FACULTY OF SCIENCE
UNIVERSITY OF COPENHAGEN

The impact of near-inertial waves on the Arctic halocline

Ida Margrethe Ringgaard

Niels Bohr Institute
University of Copenhagen

Supervisor:
Markus Jochum
Niels Bohr Institute
University of Copenhagen

October 23, 2014

Abstract

In recent years the Arctic sea ice has been observed to decrease, leading to more exposed ocean surface and enhanced turbulent mixing. Near-inertial waves have been observed to enhance through interference with the wind, and to penetrate down into the cold halocline layer. It has been suggested that near-inertial waves in the Arctic Ocean could become strong enough to penetrate through the cold halocline layer and into warmer waters, potentially causing a warming of the surface mixed layer. In this study, the impact from near-inertial waves on the Arctic halocline and mixed layer are investigated using the Hybrid Coordinate Ocean Model (HYCOM). Three different model resolutions is used: a coarse model resolution, a model with finer vertical resolution and a model with finer horizontal resolution. The model is compared to two sets of observations, one from April 2007 and one from 2008-2009, to estimate how well the model performs for specific events. The model is found to have weaker velocities and stratification compared to both observations used for comparisons, and with previous studies. Increasing the vertical resolution increases the velocity and stratification in the four events in 2005. The opposite is seen when comparing to the two specific sets of observations. Increasing the horizontal resolution does not change the current velocity significantly, but it causes a change in the atmospheric field. The cold halocline layer is not observed in any of the three model setups. The near-inertial waves is in this study observed to penetrate into the halocline, but not through it.

Resumé

I de senere år er den Arktiske havis skrumpet ind, både i tykkelsen og i udbredelsen. Dette medfører en mere åben havoverflade samt øget turbulent blanding. Det er blevet vidst i tidligere studier, at nær-inertielle bølger kan interfere med vinden og trænge gennem blandingslaget, ned til det kolde halokline lag. Derfor er det blevet foreslået, at nær-inertielle bølger i det Arktiske Ocean kan blive kraftige nok til at trænge gennem den kolde haloklin og ned til det varmere vand nedenunder, derved potentielt forårsage en opvarmning af blandingslaget. I dette studie undersøges påvirkningen fra nær-inertielle bølger på den Arktiske haloklin og blandingslag ved hjælp af Hybrid Coordinate Ocean Modellen (HYCOM). Tre eksperimenter med forskellige model opløsninger undersøges: en grov model opløsning, et eksperiment med finere vertikal opløsning og et eksperiment med finere horisontal opløsning. Modellen sammenlignes med to sæt observations, en fra april 2007 og en fra 2008-2009, for at kunne estimere hvor godt modellen simulerer specifikke episoder. Resultaterne viser, at de simulerede strømhastigheder er svagere end både observationer fra april 2007 og 2008-2009, samt værdier fundet i tidligere studier. Det samme gælder for stratifikationen. Ved at gøre den vertikale model opløsning finere, øges den simulerede hastighed samt stratifikationen for fire nær-inertielle hændelser i 2005. Det modsatte ses når de to eksperimenter med forskellig vertikal opløsning sammenlignes med observationer. Ved at øge den horisontale opløsning ændres strømhastigheden ikke, men det atmosfæriske felt gør. Det kolde halokline lag ses ikke i nogen af computer simuleringerne. De nær-inertialle bølger i dette studie trænger ned i haloklinen, men ikke igennem den.

Contents

Preface

This thesis is the culmination of my time as a geophysics student at the University of Copenhagen. The thesis was carried out over 13 months, corresponding to 60 ECTS points, in the Oceanography Group under the Climate and Geophysics Group at the Niels Bohr Institute. It was supervised by Professor Markus Jochum.

I have been interested in oceanography ever since I had my first course during my bachelor. I later wrote my bachelor project in oceanography, and was very excited when Markus Jochum started as the new oceanography professor, making it possible to study oceanography on my Master's as well.

I would therefore like to say a big thank you to Markus Jochum for suggesting this project and for all the help and guidance I have received during it. It has been very fun and interesting, and I have learned a lot. I am very grateful for this.

During this project I have analyzed model output from the Hybrid Coordinate Ocean Model (HYCOM), I have tried to setup HYCOM and run it myself, and compared my results to previous studies. It has been a very learning experience, sometimes very frustrating, but overall a very rewarding time, and it has only increased my interest in oceanography.

HYCOM is run at the Danish Meteorological Institute (DMI). I would therefore like to thank DMI for letting me use their model and in particular to Till A. S. Rasmussen, Mads H. Ribergaard and Kristine S. Madsen for using so much time to help, guide, send my useful papers and proofread my thesis. For that I am very grateful. Especially a big thanks to Till for helping me set up and run HYCOM myself. It gave me a useful insight on how large climate models work.

A special thanks to the rest of the Oceanography Group (Team Ocean) for help with technical problems and questions/ideas for my thesis during our monthly meetings.

Further, I would like to thank Turid Laksâ and Alexander C. Hansen for proofreading this thesis. It has been a great help.

A big thanks to all the people at the Master Thesis office on Rockefeller for helping me and listening to my frustrations, for all the talks and laughs, and for making this process even better: Turid Laksâ, Jeanette Aabye, Mathilde Ljungdahl, Signe Schilling, Daniel Jurlander, Søren Borg, Mads Poulsen, Kasper Hintz, Trine Jensen, Iben Koldtoft and Johanne Aagaard.

Finally, I would like to thank friends and family for all their support and thanks to my sisters Anna and Elisabeth for dragging me outside. A special thank you to Alexander for good advice, support, for putting up with me and taking care of me.

Abbreviations

ADCP	Acoustic Doppler Current Profiler
BLD	Boundary Layer Depth
CHL	Cold Halocline Layer
CICE	Los Alamos sea ice model
DMI	Danish Meteorological Institute
$E_{\text{Below ML}}$	Depth-integrated horizontal kinetic energy below the mixed layer [J m^{-2}]
E_{ML}	Depth-integrated horizontal kinetic energy in the mixed layer [J m^{-2}]
ECMWF	European Centre for Medium-Range Weather Forecasts
ERA-Interim	Atmospheric reanalysis dataset
H10	HYCOM run with a horizontal resolution of 10×10 km and 29 vertical hybrid layers
HKE	Horizontal kinetic energy [J m^{-3}]
HYCOM	Hybrid Coordinate Ocean Model
MICOM	Miami Isopycnic-Coordinate Ocean Model
MLD	Mixed Layer Depth
MMP	McLane Mooring Profiler
NICS	Near-inertial current speed
NIW	Near-inertial wave
R26	Reference run of HYCOM with a horizontal resolution of 20×20 km and 26 vertical hybrid layers
SST	Sea Surface Temperature
V42	HYCOM run with a horizontal resolution of 20×20 km and 42 vertical hybrid layers

1 Introduction

The current anthropogenic climate changes make it increasingly important to understand the dynamics of the Arctic Ocean. The sea ice cover has been observed to decrease in all seasons, but most rapid in summer and fall [IPCC (2013)], exposing more of the ocean surface to the wind, and allowing for more solar radiation to penetrate into the water. As the sea ice works as a lid on the ocean, impeding the wind from reaching the surface, and thus slowing down the mixing, a more exposed surface can lead to enhanced turbulent mixing. This enhanced mixing can potentially lead to increased sea ice melt.

Studies from other parts of the world show that near-inertial waves (NIWs) potentially play an important role in mixing in the ocean and cause a change in the water properties. Through a global numerical study Jochum et al. (2013) find that CCSM4 underestimates the near-inertial waves. By adding a parameterisation of the NIWs to the model, they find that NIWs deepen the mixed layer up to 30%, however they do not contribute significantly to the ventilation of the deep ocean or the mixing beneath the mixed layer. In addition, they alter the sea-surface temperature (SST) which in turn alters the weather patterns. Most importantly for this study, they find that in the North Pacific, the mixed layer temperature increases as a direct result of the increase in mixing due to the NIWs. The surface layer in this area is colder and fresher than the underlying water. Increasing the mixing in the model simulations causes the boundary layer to deepen into the temperature inversion, leading to a warming of the surface temperature. The temperature inversion with depth found in the North Pacific is also seen in the Arctic Ocean.

The mixing below the mixed layer is partly caused by energy propagating out of the mixed layer. Outside the Arctic, a substantial part of the wind-induced energy generated at the surface is observed to propagate out of the mixed layer. Alford et al. (2012) find that in the North Pacific, 12-33% of this energy reaches 800 m depth. They conclude that this near-inertial energy can potentially play an important role in mixing the deep ocean. Furuichi et al. (2008) uses a global primitive equation model to estimate that 75-85% of the wind-generated energy in the mixed layer is dissipated in the upper 150 m.

From studies outside the Arctic, it seems plausible that near-inertial waves contribute to mixing in the Arctic Ocean and cause a change in the water properties. A warming of the surface mixed layer can potentially lead to increased sea ice melt. However, not many observations are made in the Arctic Ocean due to the rough surroundings. Further south, satellite measurements are used abundantly, but since the ocean surface in the Arctic most of the time is covered with sea ice, satellite data cannot be used to measure properties of the water [Rainville et al. (2011)]. In the central Arctic Ocean, Fer (2014) find mixing caused by wind-generated near-inertial waves into the pycnocline. Martini et al. (2014) observes elevated levels of wind-induced near-inertial kinetic energy down to 500 m in the Beaufort Sea. Both suggest that near-inertial mixing might become increasingly important as the sea ice concentration decreases.

The same is suggested by Toole et al. (2010) and Shaw et al. (2009). However, neither of them observe near-inertial waves penetrating into warmer waters. Toole et al. (2010) suggests that the mixed layer becomes fresher and warmer and thus enhances the stratification, impeding the near-inertial waves to penetrate down below the mixed layer, even though the near-inertial waves themselves might become stronger. Shaw et al. (2009) finds that the heat flux at the base of the mixed layer is too small for it to contribute significantly to sea ice melting. They further suggest that the larger exposed ocean surface will allow more solar radiation to penetrate into the water and thus heat it up, leading to a stronger stratification.

Rainville and Woodgate (2009) find that near-inertial waves generated in summer deepens the surface mixed layer into the pycnocline. From this they suggest that the changes in the upper ocean might alter the pan-Arctic water transport and the water mass formation.

Yang et al. (2004) observed several near-inertial events in the Beaufort Sea, but they only reached the halocline or upper thermocline. However, they do observe warm thermocline water to mix into the mixed layer, concluding that the thermocline is not always separated from the mixed layer. These measurements were not taken in the centre of the storms that generated them, for which reason Yang et al. (2004) hypothesises that if the near-inertial waves are generated in the centre of the storm, the waves could potentially reach deeper into the thermocline.

Hence, there are studies of sporadic events at single locations or observations from drifter buoys, but observations covering a larger area over a long time period have not been made. In order to understand the dynamics of the Arctic Ocean and, in this case, the impact from near-inertial waves, the observations have to be combined with computer models for a complete understanding.

In this study the Hybrid Coordinate Ocean Model (HYCOM) is used to investigate the near-inertial waves in the Arctic Ocean, to test if they have a potential impact on the mixing and stratification. These results are compared to observations made by Fer (2014) and Martini et al. (2014), to see how well the model performs at two specific events.

Chapter 2 describes the dynamics of the Arctic Ocean and inertial waves. Chapter 3 describes the HYCOM model and chapter 4, the selection process of the near-inertial events investigated. The results are presented and discussed in chapters 5 and 7. The conclusions are in chapter 8.

2 Theory

To investigate the impact from near-inertial waves on the Arctic Ocean it is important to understand the dynamics of the oceans, in particular the Arctic Ocean, as well as the dynamics of near-inertial waves. Below are the general driving mechanism of the oceans described. Section 2.1 describes the structure and important features of the Arctic Ocean, and section 2.2 describes the near-inertial waves. At last, section 2.3 connects the near-inertial waves to the Arctic Ocean.

Oceans are primarily driven by two processes: the wind and the thermohaline circulation. Roughly put, the wind acts on the surface layer of the ocean, whereas the thermohaline circulation drives the circulation deeper down. In reality the two processes interact.

The wind exerts a stress on the ocean surface that can be parameterised as, $\boldsymbol{\tau} = \rho_a C_D |\mathbf{W}|\mathbf{W}$ [Bleck et al. (2002)] with ρ_a being the air density, C_D a drag coefficient and $\mathbf{W}$ the wind velocity vector. This wind stress, in turn, induces a mass transport given by the Sverdrup balance [Pedlosky (1996)]

$$\beta V_S = \frac{\mathrm{curl}_z \boldsymbol{\tau}}{\rho_0}, \tag{2.1}$$

with V_S being the meridional water mass transport, ρ_0 the water density and τ the wind stress. β is the change in the Coriolis parameter, f, with meridional distance, given as $\beta = \frac{2\Omega cos(\phi)}{R}$, with ϕ being the latitude, Ω the angular velocity of the Earth and R the radius of the Earth. The Sverdrup balance shows that the vertically integrated meridional mass transport in the ocean depends on the latitude ϕ and the curl of the wind stress.

The circulation below is driven by the thermohaline circulation, i.e. the change in distribution of temperature (thermo) and salinity (haline). The density is determined by temperature, salinity and pressure through the equation of state. The equation of state can be parameterised with many terms, the UNESCO equation of state consists of a 26-term polynomial [Brydon et al. (1999)]. A very simple, linear equation is parameterised in Knauss (2005):

$$\rho - \rho_0 = [-a(T - T_0)] + b(S - S_0) + kp \tag{2.2}$$

where ρ is density, T temperature, S salinity, p pressure and a, b and k are the coefficients for thermal expansion, saline contraction and compressibility, respectively. The subscripts indicate reference values. This equation shows that the density will increase with decreasing temperature, increasing salinity and pressure.

2.1 The Arctic Ocean

The Arctic Ocean covers the area from the Bering Strait to the coast of Russia, across the North Pole and down towards the Atlantic Ocean, see figure 2.1. However, its boundaries are not well defined [Knauss (2005)]. About a third of the Arctic Ocean is less than 200 m deep and the rest consists of two deep basins (down to around 4500 m), separated by the Lomonosov ridge [Knauss (2005)].

2.1.1 The vertical structure of the Arctic Ocean

The general vertical structure of the oceans consists of 3 distinct regions: the surface mixed layer, a highly stratified region and the deep ocean interior. The stratified region consists of

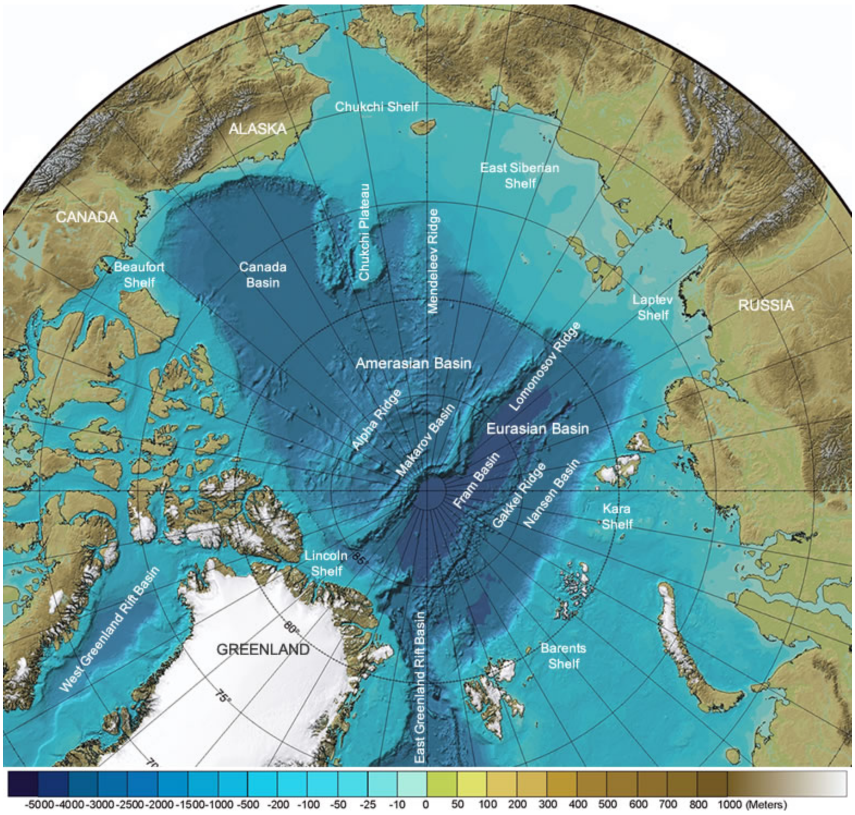

Figure 2.1: Map of the Arctic Ocean. Figure from Map of the Arctic Ocean, Web 1.

the thermocline and halocline. The thermocline is the region where the temperature changes strongly with depth. The halocline is the equivalent, but for salinity.

In the mid-latitude oceans the temperature typically decreases with depth. The salinity behaves in a similar way, until it reaches a minimum around a few hundred meters down, after which it starts to increase [Knauss (2005)].

In the Arctic Ocean the general structure is quite different. Figure 2.2(a) shows a schematic of the temperature and salinity profiles in the Arctic Ocean. It shows three distinct regions: the surface mixed layer, the cold halocline layer (CHL) and the Atlantic Water (AW).

The mixed layer is the layer closest to the surface. The temperature and salinity distributions are very uniform and, in the Arctic Ocean, the temperature is close to the freezing point. The thickness of the layer varies with season and wind forcing, but is generally 10-100 m. The base of the mixed layer is normally determined as the shallowest depth where a variable, normally either temperature or density, varies more than a certain critical value from the surface value [Knauss (2005)]. The surface mixed layer is formed due to sea ice formation, river runoff and inflowing warm water from the Pacific Ocean (Pacific Summer Water (PSW)) through the Bering Strait [Aagaard et al. (1981)]. The mixed layer is also influenced by the wind and the solar radiation. During the summer, more ocean surface is exposed to the Sun through open water areas, leads and melt ponds. Thus, more heat is transferred to the ocean, which heats it up. During winter, most of the ocean surface is covered with ice, and as the solar radiation at high latitudes is very low during winter, the ocean looses sensible heat through the few leads present. Heat is also transferred through the ice, but on a smaller scale than through the open leads. Most of the energy transferred from the wind to the ocean occurs through the open ocean. However, as the wind sweeps over the sea ice, friction is generated between the sea ice and the ocean surface. This transfers a smaller amount of energy to the ocean. Thinner and less compact sea ice can

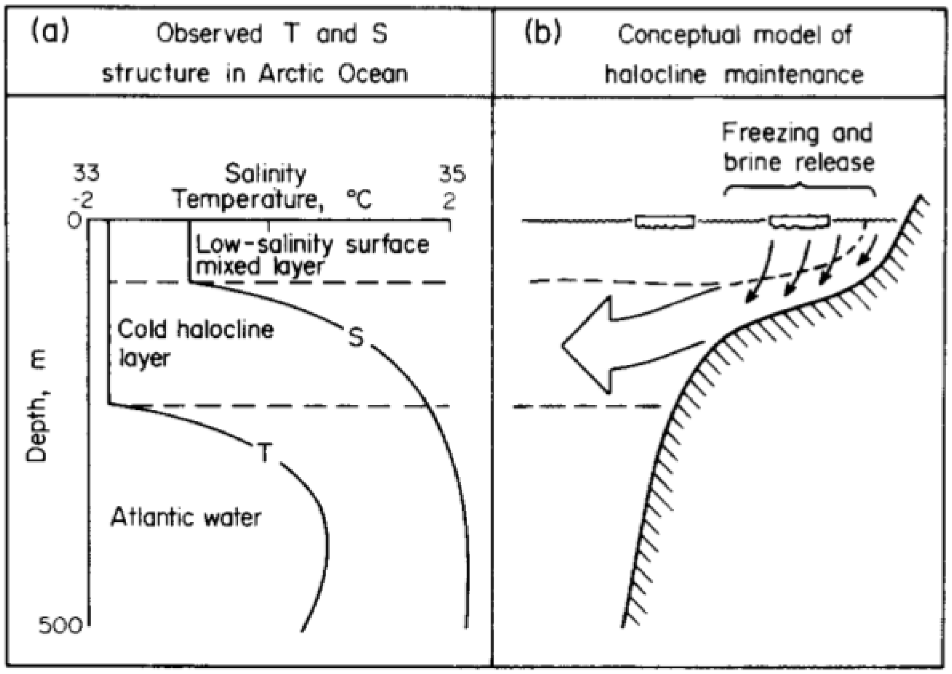

Figure 2.2: Schematic showing the cold halocline layer (a) and how it is formed (b). Figure from Aagaard et al. (1981).

move around better than compact, thick sea ice.

Below the mixed layer is the cold halocline layer. The CHL is formed due to cold and saline water flowing in from the shelf areas [Aagaard et al. (1981)]. This water is produced by a combination of brine rejection and a shallow water depth on the shelf, leading to very cold and saline water, see figure 2.2(b). The result is an isothermal layer, where the salinity increases with depth, see figure 2.2(a).

The CHL acts as a barrier between the cold, low-saline mixed layer and the warm, saline Atlantic Water underneath. The Atlantic Water is located around 300 m depth and originates, as the name implies, in the Atlantic Ocean. Close to the North Pole, the warm core is at a depth of approximately 300 m, but the depth increases with distance from the Atlantic Ocean [Sirevaag et al. (2011); Knauss (2005)].

2.1.2 Barotropic and baroclinic waves

Geostrophic flow (balanced flow between the pressure gradient and the rotation of the Earth) consists of a barotropic and a baroclinic component. For the barotropic component, the density only depends on pressure, i.e. the density is constant with depth. For baroclinic flow, the density changes with depth. This flow can be separated into its horizontal and vertical components, resulting in vertical shapes of orthogonal eigenfunctions (modes), see figure 2.3. These modes describe the magnitude of the velocity with depth. For the barotropic mode, the velocity will be uniform with depth. The first baroclinic mode has one node. This means that, in the example in figure 2.3, the flow in the upper 500 m and the flow below 500 m will be in opposite directions, while the velocity at 500 m is zero (the nodal point). The higher baroclinic modes have multiple nodes. The phase speed of the baroclinic modes decrease with increasing mode, meaning that the lower modes are the most significant [Emery and Thomson (1998)]. The current velocity is the sum of all of these modes.

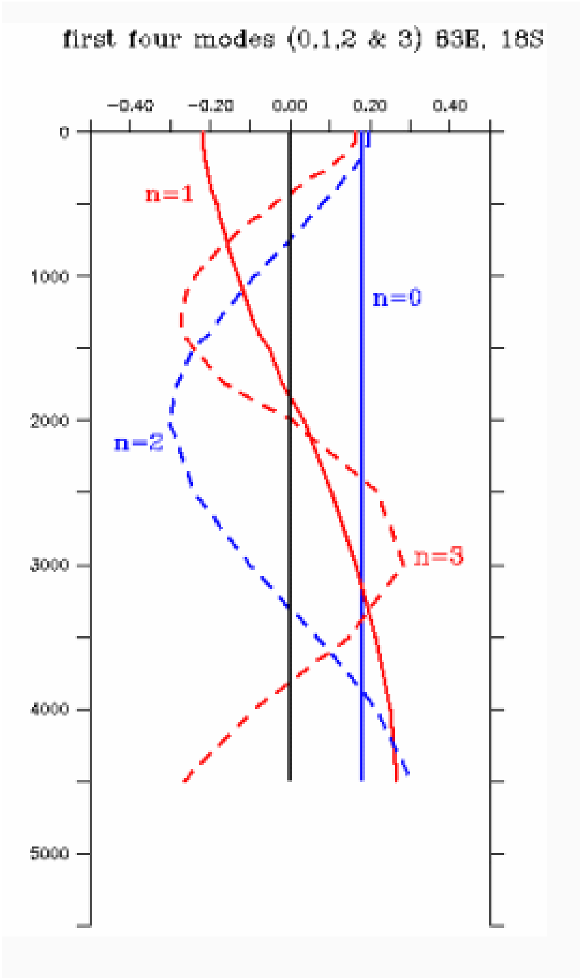

Figure 2.3: The eigenfunctions for the horizontal current velocity for a location in the Indian Ocean. The barotropic mode (n=0) and the baroclinic modes (n=1,2,3,etc.). n corresponds to the number of zero-crossings. Figure from Oceanographers.net, Web 2

2.1.3 Climate changes

The Arctic Ocean has experienced great changes in the last couple of decades due to a changing climate. The global atmospheric and oceanic temperature has increased and the sea ice extent is decreasing and thinning in most places [IPCC (2013)]. This results in larger areas of open water in the summer. This in combination with the thinner sea ice, allows the sea ice to move more freely around. There are two consequences: first, it optimises the effect of the wind on the ocean surface and hence mixing in the ocean. Secondly, the albedo (how much solar radiation is reflected and how much is absorbed) for the open ocean is much lower (0.03-0.30) than for sea ice (ranging as high as 0.80-0.90 for new snow [Suh (2011); Knauss (2005)]). When more of the ocean surface is ice-free, more of the solar radiation is absorbed by the ocean, heating the surface layers. This causes more sea ice to melt, creating a positive feedback mechanism.

2.2 Inertial waves

Inertial motion occurs when the frictional and pressure forces on a particle are neglected, leaving only the influence from the rotation of the Earth. The motion of a fluid is parameterised through

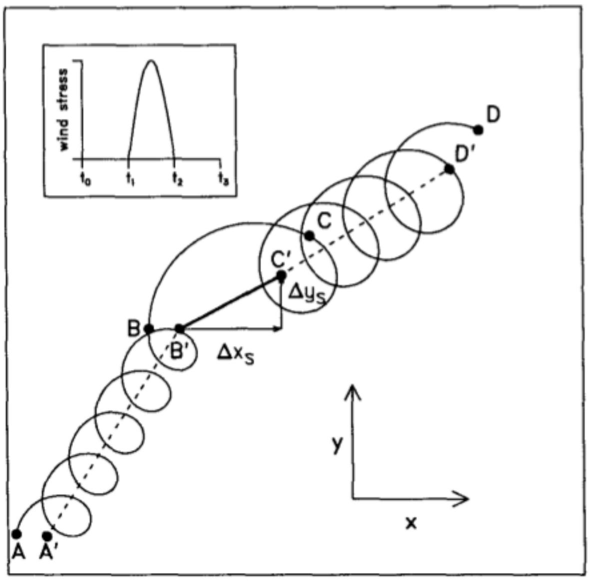

Figure 2.4: The inertial path line AD (thin solid line) and the non-inertial path line A'D' (dashed line) of a particle. The inset shows the wind stress τ where $\tau = 0$ from t_0 to t_1 and from t_2 to t_3. Between t_1 and t_2 a storm about 0.5 inertial period occurs. The storm enhances the inertial motion. Figure from Large and Crawford (1995).

the Navier-Stokes equation:

$$\frac{D\mathbf{U}}{Dt} = -2\mathbf{\Omega} \times \mathbf{U} - \frac{1}{p}\nabla p + \mathbf{g} + \mathbf{F_r}, \tag{2.3}$$

which then reduces to

$$\frac{Du}{Dt} = fv, \tag{2.4}$$

$$\frac{Dv}{Dt} = -fu, \tag{2.5}$$

where D/Dt is the total derivative, $\mathbf{U} = (u, v)$ is the velocity vector, p is the pressure, $\mathbf{g}$ is the gravitational force, $\mathbf{F_r}$ is the frictional forces and $f = 2\Omega\sin(\phi)$ is the Coriolis parameter[1], with Ω being the angular velocity of the Earth and ϕ the latitude [Knauss (2005)]. Since equations 2.4 and 2.5 are the equations for a circle, the particle will rotate. The motion of the particle is a combination of the rotation of the Earth and the advection along the ocean current. The rotation of the particle is caused by the rotation of the Earth. A particle moving north on the northern hemisphere of the Earth will be reflected to the right, due to the rotation of the Earth. This results in a clockwise rotation on the northern hemisphere and an anticlockwise rotation on the southern hemisphere. The cause of this is conservation of momentum of the particle and is known as the Coriolis force [Knauss (2005)].

Combining this circular motion with the motion of the background current, causes the particle to move in the same overall direction as the background current, while moving in circles, as is shown in figure 2.4 [Large and Crawford (1995)]. The period, T_i, of the inertial motion is given by:

$$T_i = \frac{2\pi}{f} \tag{2.6}$$

[1] f is called the Coriolis parameter, the Coriolis frequency and the inertial frequency

For the Arctic Ocean this gives inertial periods between 11.97 hours at the North pole, to around 13 hours at the Arctic Circle (located at the 66.56°N). The horizontal radius of the inertial oscillations is a few kilometres.

2.2.1 Generation of near-inertial oscillations

The wind excites a variety of waves in the ocean. Waves with frequencies close to the local inertial frequency are called near-inertial waves. These waves are present even with no winds present, but the wind can potentially enhance them. D'Asaro (1985) showed that changes in wind stress with time are the main component in generating near-inertial oscillations:

$$\frac{dZ_I}{dt} + \omega Z_I = -\frac{dT}{dt}\frac{1}{\omega H} - \frac{d(1/H)}{dt}\frac{T}{\omega} \tag{2.7}$$

where Z_I are the complex mixed layer velocities and $w = r + if$, with r being an artificial damping constant, related to energy transfer from the mixed layer to the deeper ocean. H is the mixed layer depth and $T = \frac{\tau_x + i\tau_y}{\rho}$ is the complex wind stress. The change in mixed layer depth with time, $\frac{dH}{dt}$, is slower than the change in wind stress with time, which means that $\frac{dH}{dt}$ can be ignored. Thus, the inertial currents depend on the change in wind stress with time.

Pollard (1970) states that the strength of the inertial oscillations depend on the timescale of fluctuations in the wind and the mixed layer depth. Further, he states that the horizontal scale of the wind fields and the stratification is less important. However, Rimac et al. (2013) showed that the horizontal resolution of the atmospheric fields actually influences the wind power input into the ocean mixed layer.

In addition to the intermittent wind fluctuations, the direction and frequency of the wind affects the inertial oscillations as well. An inertial oscillation rotates a full circle in an inertial period. If the wind blows in the same direction longer than the inertial period, the current momentum is increased in the first half of the inertial period, but is decreased in the other half. On the other hand, if the wind turns with the inertial frequency, it blows in the same direction, at the same pace as the inertial current, increasing its momentum. Inertial currents are thus generated by either a strong wind blowing in one direction for maximum half an inertial period or a strong wind turning with the inertial period [Pollard and Millard Jr. (1970)].

Due to the strong connection between the inertial waves, the wind and the mixed layer depth, the most energy is transferred to the ocean from October to February, when the winds are the strongest and the mixed layer the shallowest [D'Asaro (1985)].

2.2.2 Wind-induced energy

As explained above, the wind transfers energy to the ocean surface layer. Furuichi et al. (2008) estimates the global wind work to be 0.35 TW and Simmons and Alford (2012) estimates that about half of the kinetic energy in the ocean is contained in near-inertial waves. Some of this energy is used for mixing, some is destroyed by the wind, as explained above, and some propagates either downwards or towards the Equator.

Mixing caused by inertial waves

Most of the energy transferred from the wind to the ocean is used for mixing in the mixed layer. The wind generates currents in the mixed layer, causing a deepening of the mixed layer. Dohan and Davis (2010) investigate the effect of two consecutive storms occurring in the autumn of 1987 in the Northern Pacific, during The Ocean Storms Experiment. The first storm generates strong currents in the mixed layer. These currents deepen the mixed layer, digging into the transition layer (the stratified region above the seasonal pycnocline). The second storm resonates with the currents, creating strong inertial currents. The mixed layer does not deepen, in fact it shoals slightly. In this case, the mixing occurs below the base of the mixed layer, in the transition layer. In the mid-latitudes, the temperature decreases with depth, so if the wind-induced inertial currents causes mixing between the lower mixed layer and the transition layer, this will draw up cold water into the mixed layer. These events are called episodic cooling events.

Advection of energy

Near-inertial waves are not isolated waves, they are part of larger current systems. When investigating a single stationary point in space, the water will flow by continuously. Hence, the energy might not decrease as rapidly as it might appear, it simply advected away from the investigated point to an adjacent point.

Propagation of inertial waves

Simmons and Alford (2012) estimates that 3-16% of the kinetic energy in the mixed layer radiates down- and equatorward, depending on the season. Pollard (1970) find that the inertial wave amplitude decreases rapidly below the mixed layer. Alford et al. (2012) investigated a 2-year record at Ocean Station Papa (50°N, 145°W) from which they estimates that 12-33% of the energy input at the ocean surface reached 800 m. Using a three-dimensional primitive equation model, Furuichi et al. (2008) estimates that 75-85% of the wind-induced energy is dissipated in the upper 150m. Hence, the wind-induced inertial waves may be an important factor in mixing the mixed layer as well as the ocean interior.

In addition to propagating downward, the inertial waves can also propagate equatorward and slightly poleward.

This primarily equatorward motion comes from the fact that the frequency of a freely propagating internal wave must be between the inertial frequency f and the buoyancy frequency N. The fluid motion is nearly horizontal when the frequency is close to f and vertical when close to N. Inertial waves are dispersive and for inertia gravity waves the group velocity is [Garrett (2001); Knauss (2005)]

$$\mathcal{V}_i = \sqrt{gh}\sqrt{1 - \left(\frac{f}{\omega}\right)^2}, \tag{2.8}$$

where h is the water depth. Only if the frequency, ω, of the wave is larger than the inertial frequency f, is the group velocity real. Since $T \sim 1/\omega$, this means that the longest period of the wave must be the inertial period $T_i = 2\pi/f$ [Knauss (2005)]. Hence, the near-inertial waves propagate poleward until they reach a latitude where their frequency equals the local inertial frequency. Here they turn toward the equator instead [Simmons and Alford (2012)].

2.3 Inertial waves in the Arctic Ocean

The reason why all of this is interesting is that the CHL isolates the cold, low-saline mixed layer from the warm Atlantic Water below. As explained above, episodic cooling is observed in mid-latitudes. Due to the inverse temperature gradient in the Arctic, it has been suggested that the opposite can occur here, i.e. that the warm Atlantic water can potentially mix into the mixed layer, thus cause a warming of the surface waters [Yang et al. (2004); Rainville and Woodgate (2009); Rainville et al. (2011)]. Yang et al. (2004) found wind-driven events in the Arctic Ocean that reached the halocline and even the thermocline. They conclude that the warm thermocline waters can mix into the mixed layer, despite the strong stratification caused by the halocline.

With the decreasing ice cover in the Arctic Ocean, more ocean surface is exposed to the wind which can potentially lead to more frequent and stronger inertial events. Previously the sea ice has worked as a barrier between the wind and the ocean, damping the incoming energy. The energy level in an ice-covered ocean is about an order of magnitude lower than in ice-free oceans [Rainville et al. (2011)].

2.3.1 Tides in the Arctic Ocean

Tides are generated by the gravitational pull of the Sun and the Moon on the Earth. This results in ocean waves creating high and low tides twice a day (semidiurnal) or once a day (diurnal). Near the poles, the inertial frequency is similar to the frequency of the semidiurnal tides. The dominating constituents of the semidiurnal tides are M_2 (lunar constituent) and S_2 (solar constituent) which have periods of 12.42 hours and 12.00 hours, respectively [Knauss (2005)].

Fortunately, tides can be ignored for a number of reasons:

1. Tides are generally weak in the deep basins in the Arctic Ocean, except on the continental shelves where there are strong tidal currents [Polyakov (1997)]. Due to the very long wavelength of tides, they are classified as shallow water waves [Knauss (2005)]. This means that they depend on the water depth, as is seen from the shallow water equation:

$$u = a\sqrt{\frac{g}{h}} \tag{2.9}$$

   where u is the current velocity, a the wave amplitude, g the gravitational acceleration and h the water depth [Knauss (2005)]. Thus, in places with great water depth, tides can be ignored [Fer (2014); Dosser and Rainville (2014)].

2. Tides are generated by a body force, whereas inertial currents are generated by surface friction. This means that the tides are the same in the entire water column, while the inertial waves are concentrated at the ocean surface. By connecting the inertial current events to atmospheric storms, which should have no effect on tides, tidal forces can safely be ignored.

3. Finally, Pinkel (2005) showed that near-inertial internal waves are the dominant waves in the Arctic Ocean.

2.3.2 Relationship between ice concentration and wind-induced energy input

The ice cover on the Arctic Ocean plays a vital role in how much wind-induced energy are transferred into the ocean. In HYCOM, see section 3, the wind stress is linearly dependent on the ice concentration [Bleck et al. (2002)]. The stress on the ocean surface is determined partly by the wind stress on the open ocean surface and partly by the friction between the sea ice and the underlying ocean. This means that the less ice, the higher the wind stress. However, Martin et al. (2014) showed that at wind speeds greater than 3 m s^{-1} the air drag over ice is larger than over the open ocean. The ice can either be dragged along by the wind, or it can remain stationary, depending on if, the sea ice consists of compact sea ice or ice floes. Martin et al. (2014) used this to show that the ocean surface stress has increased the last three decades in winter, spring and fall and decreased in summer. They suggest that the decrease during summer is caused by the reduction in sea ice concentration, leading to the total air stress being affected more by the weaker air-ocean stress. They conclude that the optimal ice concentration for momentum flux into the Arctic Ocean is $80 - 90\%$. However, the roughness of the surface and bottom of the sea ice depends on the age and deformation, which is not taking into account.

3 Model

The near-inertial waves in the Arctic Ocean are investigated using the forced HYbrid Coordinate Ocean Model (HYCOM, code version 2.5.5) [Bleck et al. (2002)] coupled with the Los Alamos sea ice model (CICE) [Hunke et al.]. Both are run at the Danish Meteorological Institute (DMI). HYCOM is based on the primitive equations and is based on the Miami Isopycnic-Coordinate Ocean Model (MICOM).
Below is a brief review of the basic equations in HYCOM, a description of the hybrid coordinate and the vertical mixing scheme, KPP, used in this model. For a detailed description of the model see Bleck et al. (2002) and Bleck (2002).

3.1 Model description

3.1.1 Model grid

The grid used in HYCOM is the Arakawa C grid. This grid is a standard Cartesian grid. Velocity and vorticity are calculated on the interfaces of each grid cell, whereas pressure, temperature, salinity, momentum and the other model variables are calculated in the centre of the grid cell. The model output is then rotated to have east in the positive x-direction and north in the positive y-direction.

3.1.2 Governing equations

The governing equations in HYCOM are shown below, written in (x, y, s) coordinates. For more details on how they are derived and implemented in the model, see Bleck et al. (2002). The basic assumptions are those of an incompressible ocean (constant density in each layer) and an adiabatic flow (no heat transfer between the parcel and its surroundings).

The continuity equation (conservation of mass):

$$\frac{\partial}{\partial t_s}\left(\frac{\partial p}{\partial s}\right) + \nabla_s \cdot \left(\mathbf{v}\frac{\partial p}{\partial s}\right) + \frac{\partial}{\partial s}\left(\dot{s}\frac{\partial p}{\partial s}\right) = 0 \tag{3.1}$$

Conservation of momentum:

$$\begin{aligned}\frac{\partial \mathbf{v}}{\partial t_s} + \nabla_s \frac{\mathbf{v}^2}{2} + (\zeta + f)\mathbf{k}\times\mathbf{v} + \left(\dot{s}\frac{\partial p}{\partial s}\right)\frac{\partial \mathbf{v}}{\partial p} + \nabla_s M - p\nabla_s\alpha \\ = -g\frac{\partial \tau}{\partial p} + \left(\frac{\partial p}{\partial s}\right)^{-1}\nabla_s \cdot \left(\nu\frac{\partial p}{\partial s}\nabla_s \mathbf{v}\right)\end{aligned} \tag{3.2}$$

The advection/diffusion equation:

$$\frac{\partial}{\partial t_s}\left(\frac{\partial p}{\partial s}\theta\right) + \nabla_s \cdot \left(\mathbf{v}\frac{\partial p}{\partial s}\theta\right) + \frac{\partial}{\partial s}\left(\dot{s}\frac{\partial p}{\partial s}\theta\right) = \nabla_s \cdot \left(\nu\frac{\partial p}{\partial s}\nabla_s\theta\right) + \mathcal{H}_\theta \tag{3.3}$$

where s is the vertical, hybrid coordinate, $\mathbf{v} = (u, v)$ is the horizontal velocity vector, p is the pressure, g is the gravitational force, ζ is the relative vorticity, f is the Coriolis parameter, k the vertical unit vector, $M = \phi + p\alpha$ is the Montgomery potential where ϕ is the geopotential and α is the potential specific volume. The Montgomery potential represents the pressure when density ρ, and not the depth z, is used as the vertical coordinate. The shear stress induced by either the wind or the ocean bottom is represented by τ and the eddy viscosity/diffusivity coefficient by ν. In the advection equation, eq. (3.3), θ is the thermodynamic variable and $\mathcal{H}_\theta$ is the sum of the diabatic source terms acting on the chosen variable. The subscripts indicate which variable is held constant during partial differentiation and $\dot{s}$ is the time derivative of the coordinate s.

3.1.3 The hybrid coordinate and vertical layers

As the name suggests, HYCOM uses a hybrid coordinate as the vertical coordinate. A hybrid coordinate adapts to the surroundings and can change smoothly between 3 different coordinate types. The three types are: z-level coordinate, isopycnic coordinate and σ-coordinate. In this model study only the z-level coordinate and the isopycnic coordinate are used.

The z-level layers have fixed depths and are therefore independent of both time and space. This type of coordinate is suitable for the surface mixed layer and in very shallow regions, since the horizontal pressure gradients here can be calculated accurately [Kantha and Clayson (2000)]. The downside to this fixed depth coordinate is that unless the bottom is perfectly flat, the bottom layers will intersect with the topography, causing the vertical velocity to be wrong. As a means to avoiding this, the isopycnic and σ-coordinates are used as well.

The terrain-following σ-coordinate uses the pressure at a specific depth, p, normalized by the surface pressure, p_s, to determine the thickness of each layer [Holton (2004)]. A specific number of layers are defined and these layers then vary in thickness, depending on the total water depth. By doing this, the uppermost layer follows the ocean surface and the bottom layer always follows the bottom topography and thereby prevent the errors in the vertical velocity described earlier.

The σ-coordinate is used in shallow waters, but in the open, deep ocean the isopycnal coordinate is used. The reason for this, is that the z-level and σ-coordinates are Eulerian, whereas the isopycnal approach is Lagrangian. This means that the z-level and σ-coordinates are time independent and the isopycnal coordinate is not. The isopycnal layers are determined by the density distribution, which changes at each time step. Each layer is assigned a reference density, ρ_{ref}, set in the model setup. If the grid point does not lie on the reference isopycnal, it is moved vertically until it reaches it, but still conserving the height of the water column. If the density in layer 1 is lighter than the reference density of that layer, i.e. $\rho_1 < \rho_{ref}$ the lower boundary of the layer is moved downwards to allow for denser water to transfer into the layer. If the opposite is the case, $\rho_1 > \rho_{ref}$, the upper boundary is moved upward to transfer lighter water into layer 1. If the layers then become to thin, they are set to a predefined thickness.

3.1.4 Vertical mixing scheme: KPP

The vertical mixing scheme used in this study is the K-Profile Parameterization (KPP) [Large (1994)]. KPP is a semi-implicit, nonlocal, non-slab boundary layer parameterisation. Using the boundary layer depth it estimates the vertical mixing in both the surface boundary layer and in the ocean interior, allowing the boundary layer to penetrate into the stratified region below. Nonlocal means that a property depends on both the local parameters as well as the boundary layer parameters [Large (1994)]. The surface boundary layer is affected by the wind, buoyancy and convection, whereas the ocean interior is influenced by shear instability, internal waves breaking and double diffusion.

Boundary layer depth

The boundary layer depth is defined as the depth to which turbulent boundary eddies can penetrate. This depth is estimated using the bulk Richardson number, which is the ratio between the buoyancy and the vertical shear.

$$Ri_b = \frac{(B_r - B)d}{(\mathbf{v}_r - \mathbf{v})^2 + V_T^2} \tag{3.4}$$

where B is the buoyancy, d is the depth, $\mathbf{v}$ the horizontal velocity vector and V_T^2 the unresolved turbulent velocity shear. The subscript r is for reference values which are averaged over the depth range ϵd, where $\epsilon = 0.1$. The surface boundary layer depth h_b is the minimum depth at which Ri_b exceeds the critical Richardson number Ri_c, here set to 0.3.

Mixing in the surface boundary layer

The boundary layer thickness h_b is used to calculate the surface boundary layer diffusivity which then is combined with the values for the ocean interior. The surface boundary diffusivity (for potential temperature and salinity) and viscosity (for momentum) are parameterised in the following way:

$$\overline{w'\theta'} = -K_\theta \left(\frac{\partial \bar{\theta}}{\partial z} + \gamma_\theta \right), \tag{3.5}$$

$$\overline{w'S'} = -K_S \left(\frac{\partial \bar{S}}{\partial z} + \gamma_S \right), \tag{3.6}$$

$$\overline{w'\mathbf{v}'} = -K_m \left(\frac{\partial \bar{\mathbf{v}}}{\partial z} \right), \tag{3.7}$$

where w is the turbulent vertical velocity of the unresolved eddies, θ is the potential temperature, S is the salinity and γ_θ and γ_S are nonlocal transport terms. A bar denotes mean values and a prime denotes the turbulent contribution. Bold variables are vectors. The diffusivity/viscosity terms (K_θ, K_S, K_m) are:

$$K_\theta(\sigma) = h_b w_\theta(\sigma) G_\theta(\sigma), \tag{3.8}$$

$$K_S(\sigma) = h_b w_S(\sigma) G_S(\sigma), \tag{3.9}$$

$$K_m(\sigma) = h_b w_m(\sigma) G_m(\sigma), \tag{3.10}$$

Here G is a smooth shape function, $\sigma = d/h_b$, and (w_S, w_θ, w_m) being the salinity, potential temperature and momentum velocity scales, respectively [Bleck et al. (2002)].

Mixing in the ocean interior

The mixing in the ocean interior is a combination of the resolved shear instability ν^s, the unresolved shear instability caused by internal waves breaking, ν^w, and double diffusion, ν^d [Bleck et al. (2002)]. The diapycnal diffusivities for potential temperature, ν_θ, salinity, ν_S, and momentum, ν_m, are given by:

$$\overline{w'\theta'} = -\nu_\theta \frac{\partial \bar{\theta}}{\partial z}, \tag{3.11}$$

$$\overline{w'S'} = -\nu_S \frac{\partial \bar{S}}{\partial z}, \tag{3.12}$$

$$\overline{w'\mathbf{v}'} = -\nu_m \frac{\partial \bar{\mathbf{v}}}{\partial z}, \tag{3.13}$$

with

$$\nu_\theta = \nu_\theta^s + \nu_\theta^w + \nu_\theta^d, \tag{3.14}$$
$$\nu_S = \nu_S^s + \nu_S^w + \nu_S^d, \tag{3.15}$$
$$\nu_m = \nu_m^s + \nu_m^w, \tag{3.16}$$

The resolved shear instability is parameterised using the local gradient Richardson number

$$Ri_g = \frac{N^2}{\left(\frac{\partial \bar{u}}{\partial z}\right)^2 + \left(\frac{\partial \bar{v}}{\partial z}\right)^2} \tag{3.17}$$

where N is the Brunt-Väisälä frequency, and $(\bar{u}, \bar{v})$ are the mean velocities. Mixing occurs if $Ri_g < 0.7$ [Wallcraft et al. (2009); Bleck et al. (2002)].

Vertical mixing

The vertical mixing is calculated using the diffusivity and viscosity defined for both the surface boundary layer and the ocean interior. This is done by repeating two steps until the vertically mixed profiles of the model variables for one iteration is insignificantly different from the profiles in the previous iteration. The two steps are:

1. For each pressure grid point the continuity, advection/diffusion and the momentum equations are solved.

2. For these grid points the vertical diffusion equation (3.20) is solved. In this way it becomes a one-dimensional problem with zero-flux boundary conditions at the surface and bottom.

The new profiles from 2) are used in 1). When there is no significant change between the mixing profiles in two consecutive iterations, the diffusivity and viscosity coefficients are interpolated to the momentum grid point and the vertical mixing equation is then calculated. In this way, it is not necessary to repeat the KPP procedure for the momentum grid cells in this point.
The vertical diffusion equations for potential temperature, salinity and velocity are:

$$\frac{\partial \bar{\theta}}{\partial t} = -\frac{\partial}{\partial z}\overline{w'\theta'} \tag{3.18}$$
$$\frac{\partial \bar{S}}{\partial t} = -\frac{\partial}{\partial z}\overline{w'S'} \tag{3.19}$$
$$\frac{\partial \bar{\mathbf{v}}}{\partial t} = -\frac{\partial}{\partial z}\overline{w'\mathbf{v}'} \tag{3.20}$$

3.2 Model domain and resolution

The spatial resolution is 20×20 km with 26 hybrid layers and a temporal resolution of a few minutes. Model output is given in snapshots every hour for surface fields and every three hours for 3D fields. A regional domain is used, covering the Arctic Ocean and the northern part of the North Atlantic, but only a smaller part covering the Arctic Ocean is investigated, as shown in figure 3.1.

The purpose of this study is to investigate inertial waves which have wavelengths of a few kilometres. It might seem as if the inertial waves are not resolved on the 20×20 km grid. However, inertial waves only depend on the Coriolis force, see equation 2.4 and 2.5 in section 2.2. Thus, the inertial velocity in one grid point does not depend on the inertial velocity in the next point. The opposite is the case for the geostrophic balance which is determined by the pressure gradient between two adjacent grid points:

$$fu = -\frac{1}{\rho}\frac{\partial p}{\partial y} \tag{3.21}$$

$$fv = \frac{1}{\rho}\frac{\partial p}{\partial x} \tag{3.22}$$

The only influence the horizontal resolution has on the inertial waves is how well the atmospheric forcing is resolved. The atmospheric resolution affects the inertial waves in two ways:

1. The storm systems generating the inertial waves must be resolved. D'Asaro (1985) showed that inertial currents are most commonly generated by cold fronts and small low pressure systems. These mesoscale systems are of the scale of 10-1000 km [Holton (2004)] meaning that the model resolution of 20×20 km is sufficient to generate the storm systems that generate the inertial waves.

2. Rimac et al. (2013) showed that increasing the spatial and temporal resolution from the low-resolution case (6-hourly and 1.88° wind data) to the high-resolution setup (1-hourly and 0.35°) increased the wind power input to the inertial oscillations from 0.3 TW to 1.1 TW. Thus, a finer grid resolution only increases the amount of the wind-power input. Whether or not there are near-inertial waves present, is not changed.

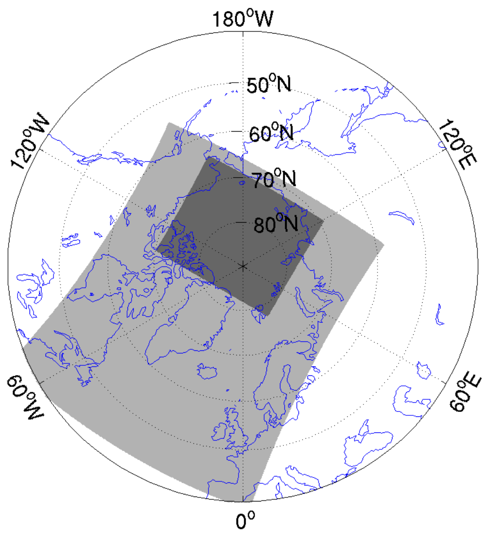

Figure 3.1: The light gray area show the model domain and the darker gray the area investigated in this study.

3.3 Atmospheric fields

The model is forced by atmospheric fields, linearly interpolated from the European Centre for Medium-Range Weather Forecasts (ECMWF) Re-Analysis ERA-Interim [ECMWF, Web 3] to the HYCOM grid [Wallcraft et al. (2003)]. Re-analysis combines observations with a model, to generate a dataset covering a uniform grid. The ERA-Interim has a horizontal resolution of ~79 km and a vertical resolution of 60 layers from the surface up to the 0.1 hPa level in the atmosphere. The temporal resolution is 3 hours [ECMWF, Web 3].

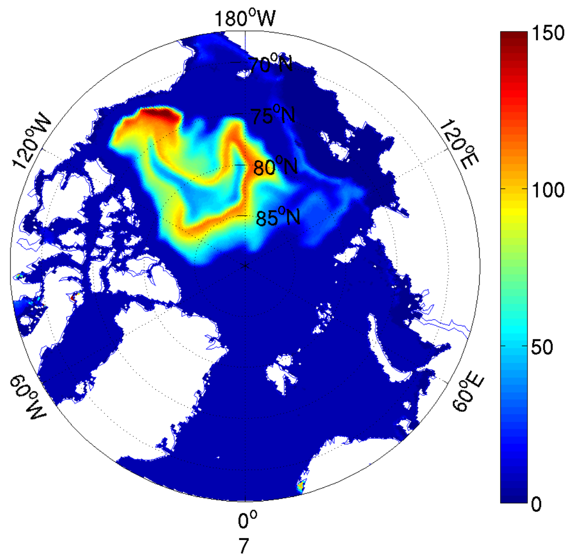

Figure 3.2: The mean thickness [m] of the 7th layer in October 2005.

The ERA-Interim is used as the standard in this study, however for one of the experiments (H10) the atmospheric forcing comes from the ECMWF operational forecast system with a horizontal resolution of 16 km and snapshots every hour, see section 3.5.

3.4 Changes to the original model setup

The thickness of the vertical layers varies greatly. In the reference experiment, one specific layer was very thick ($\sim 100 - 140$ m) in the upper 200 m, as is seen in figure 3.2. This figure shows the monthly mean of the layer thickness for this specific layer in October. Since the purpose of this study is to investigate the effect from near-inertial waves on the boundary layer and the halocline, both located in the upper 200 m, it is not ideal to have one layer being so thick.

Isopycnal layers are formed due to a homogeneous water mass. As explained in section 3.1.3 each layer is defined by a reference density. In order to increase the number of layers around this thick layer, the density jump between the layers have to be decreased. Consequently, the number of vertical, hybrid layers is increased from 26 layers in the original model setup, to 42 layers. In the original setup, DMI focused on the sea ice and therefore the surface layer, not the mixed layer as a whole. Partly due to this thick layer, 3 different experiments with varying horizontal and vertical resolution are performed.

3.5 Experiments

The near-inertial activity in the Arctic Ocean is investigated using the HYCOM model with three different model setups. The reference experiment (R26) consists of 26 vertical layers, a horizontal resolution of 20×20 km and runs from 1996 to 2013. The main analysis is done using this dataset, but to investigate the model sensitivity, an experiment with the same horizontal resolution but with 42 vertical layers (V42) is also made. The reason for this is a very thick layer in the upper 100 m in October, as explained in section 3.4 and further in section 4. This experiment is run from September 2003 to 2009. The final experiment (H10) is setup with a horizontal resolution of 10×10 km and 29 vertical layers. There are some changes to this setup, compared to R26 and V42. First of all, the atmospheric fields used in R26 and V42 are hindcasts from the ERA-Interim reanalysis, which has a horizontal resolution of $\sim 76\times76$ km and snapshots every three hours. For H10, the atmospheric forcing comes from the ECMWF operational forecast system with a horizontal resolution of 16 km and snapshots every hour. Secondly, in H10 there is assimilation on the SST from January to the end of May in 2011-2013. After this it is turned off. There is assimilation on the ice concentration the entire time. Finally, there are 29 instead of 26 vertical layers, but the three extra layers should not affect the Arctic Ocean, as they are only used when modeling the warm and saline Mediterranean.

The density layers are the same in R26 and V42 in all the years investigated, but the location of them changes.

Exp. name	Vertical resolution (no. of layers)	Horizontal resolution	Model start date	Investigated years	Atmospheric forcing
R26	26	20×20 km	1996	2005, 2007 - 2009, 2013	ERA-Interim reanalysis
V42	42	20×20 km	1/9-2003	2005, 2007 - 2009	ERA-Interim reanalysis
H10	29	10×10 km	2007	2013	ECMWF operational forecast

Table 3.1: List of experiments.

4 Method

4.1 Selecting near-inertial events

The events investigated in this study are chosen through three criteria:

1. The near-inertial speed must be 0.15 m s^{-1} or higher.

2. The ocean depth must be greater than 1000 m.

3. The ice concentration must be equal to or less than 20%.

Criteria 1

First, areas where the near-inertial speed is greater than a specific value, here chosen to be 0.15 m s^{-1}, are located. If two of these selected events are closer than 100 km and less than a day apart, the event with the largest speed is chosen. The reason is that if they are so close in time and space, it is most likely the same storm that generated them, and they will be very similar. Further, to avoid the influence from complex bathymetry near land, the events have to be more than 100 km from land.

Criteria 2

This criteria is introduced to avoid the influence from tides and topography. Tidal waves are body waves, meaning that their energy depend on the depth of the water column they are in. Therefore, tides are stronger in shallow waters than in the deep ocean (see section 2.3). Hence, by only investigating strong inertial events at locations with great water depth, the tides should be weak compared to the inertial waves and can therefore be ignored. Here only locations where the water depth is greater than 1000 m are investigated.

Criteria 3

The velocity field is up to an order of magnitude weaker under ice than in parts of the other oceans [Rainville et al. (2011)] and too weak to overcome the strong pycnocline. Hence, only events where the ice cover is less than 20% are interesting. The ice concentration used here is the weekly average, not the instantaneous ice concentration. This is done to avoid a large ice floe drifting over a specific location at the same time as a strong inertial current is generated, and thereby eliminate it as a potential interesting events.

4.1.1 Events in 2005

Using the first criteria to select strong inertial events resulted in 76 events in 2005. Figure 4.1(a) shows the distribution of events with respect to the inertial current speed and the month they occurred in. As is seen, the majority of the events, 43%, occurred in September, secondmost in October, 26%, and thirdmost in August, 17%. This is consistent with the strongest storms occurring in the fall, which contributes to make the stratification weak [Martin et al. (2014)].

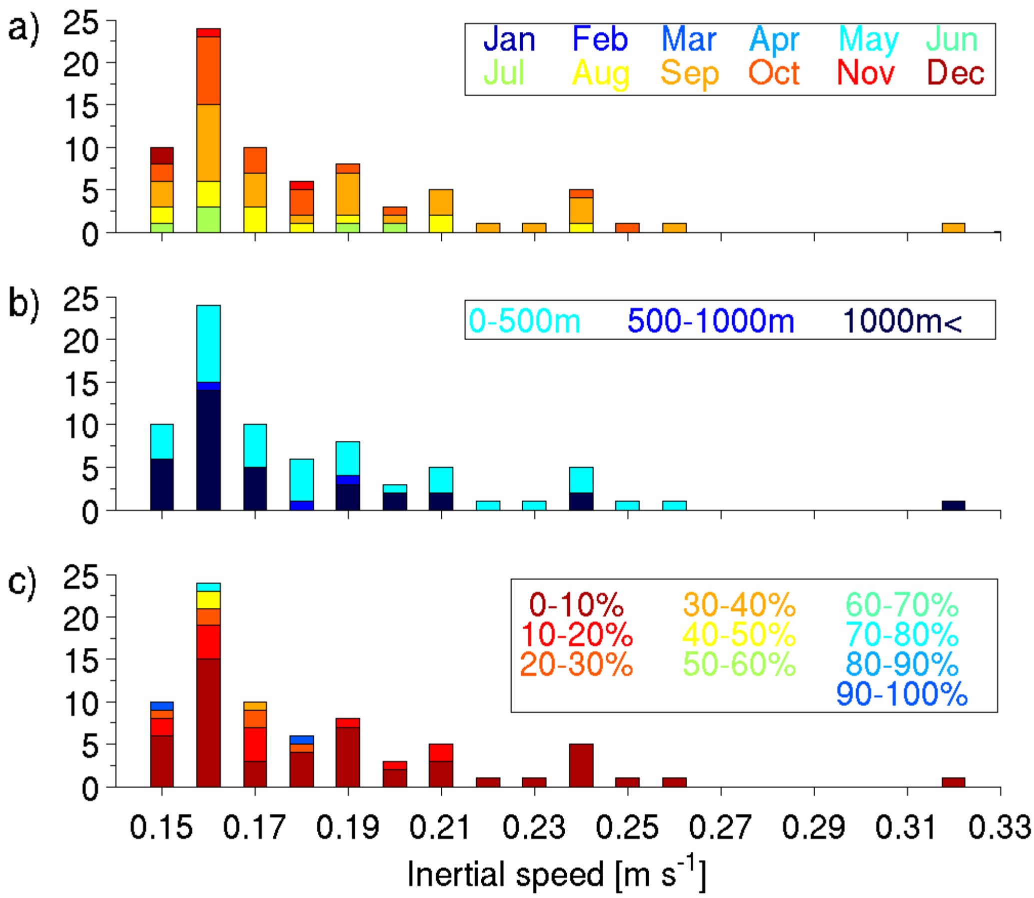

Figure 4.1: Bar plots showing the number of events in 2005 as a function of the inertial speed. The events are grouped into 0.01 m s^{-1} intervals, ranging from 0.15 to 0.32 m s^{-1}. The colours indicate a) how many events occur in each month, b) the depth of the ocean at the specific location (0-500 m, 500-1000 m or deeper than 1000 m) and c) the ice cover percentage, in intervals of 10%.

Figure 4.1(b) shows the same distribution of events as in 4.1(a), but this time depending on whether they occur at shallow depth (0-500 m), intermediate depth (500-1000 m) or in the deep ocean (greater than 1000 m). Invoking the second criteria then leaves the dark blue events. As is seen, 50% of the events occur at locations with depths less than 500 m, on continental shelves and plateaus. 46% occur in the deep basins. Thus, only about half of the strong inertial events are left after applying this criterion.

Figure 4.1(c) shows the distribution of events with respect to the inertial current speed and the weekly averaged ice cover, when they occurred. The number of inertial events decrease with increasing ice cover, with the majority (66%) of the events occurring with an ice cover of 10% or less and 84% occurring with an ice cover of 20% or less.

Martin et al. (2014) showed that the maximum momentum flux occurs at an 80-90% ice cover. This is not clear from the results shown here, but it could possibly be because of the wind stress reaching the ocean surface in the model is linearly proportional to the ice cover percent (see section 2.3.2).

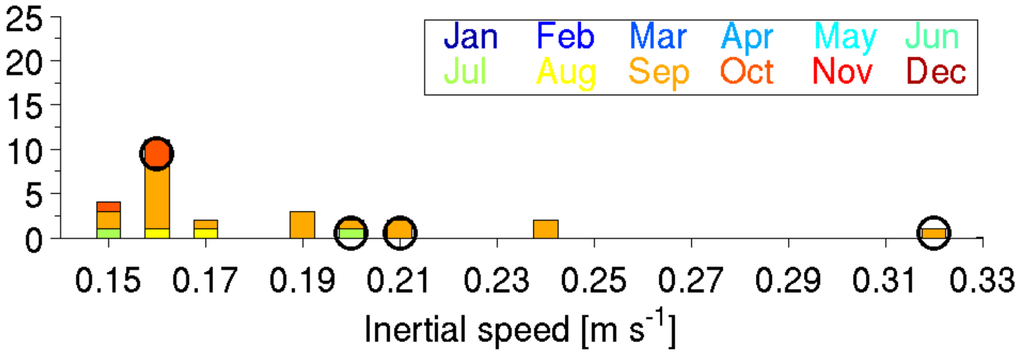

Figure 4.2: Bar plots showing the number of events in 2005 as a function of the inertial speed. The events are grouped into 0.01 m s^{-1} intervals, ranging from 0.15 to 0.32 m s^{-1}. The colours indicate how many events occur in each month. The black circles indicate the four events investigated here.

The selected inertial events

Using the three criteria to select inertial events in the Arctic Ocean reduces the original 76 events to 27. The 27 events are shown in figure 4.2 with respect to the inertial current speed and the month in which they occurred. Removing the events that occurred on shallow water or was covered by ice has shifted the distribution so that now 70% of the events occur in September and 15% in October. The spatial distribution of the 27 events is seen in figure 4.3. Many of the events occur on the boundary between the continental shelf and the deep ocean floor.

From this, four events are chosen for investigation: The overall strongest event, occurring in September, another one occurring in September but in the deep Nansen Basin, and the strongest events in July and October.

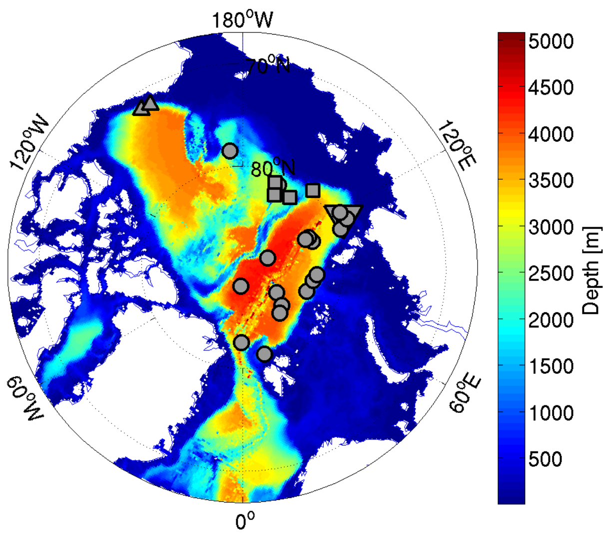

Figure 4.3: The spatial distribution of the 27 events selected. Downward-pointing triangles: July, upward-pointing triangles: August, circles: September and squares: October.

4.1.2 Events in 2013

For 2013 the same selection method is used and the results is shown below in figures 4.4 to 4.6. The events are found in R26, which is then compared to H10.

There were 35 events in 2013 with inertial speeds greater than 0.15 m s^{-1}. Out of these,

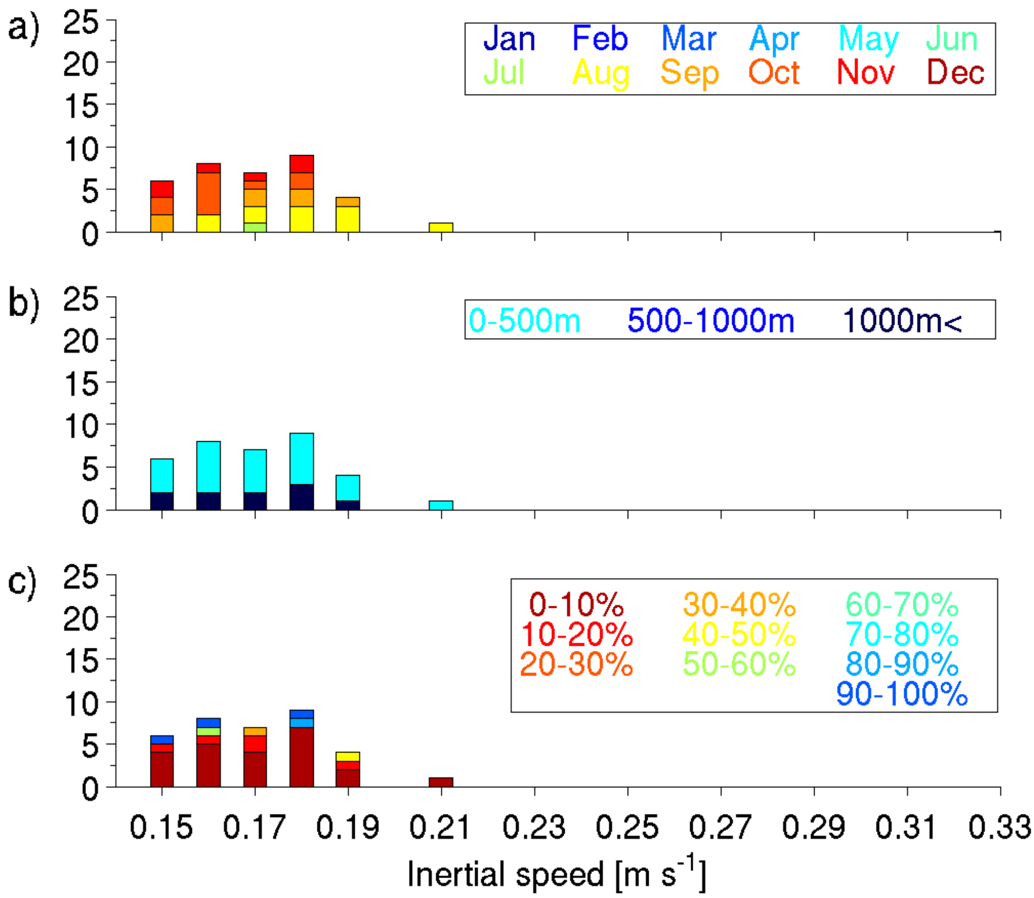

Figure 4.4: Bar plots showing the number of events in 2013 as a function of the inertial speed. The events are grouped into 0.01 m s^{-1} intervals, ranging from 0.15 to 0.32 m s^{-1}. The colours indicate a) how many events occur in each month, b) the depth of the ocean at the specific location (0-500 m, 500-1000 m or deeper than 1000 m) and c) the ice cover percentage, in intervals of 10%.

three events fulfilled the three criteria described above. In figure 4.5 the inertial speeds of these three selected events are seen. The strongest event, occurring in November, is investigated. The reason for choosing this is, the event in September occurred on the Yermak Plateau, were the topography interacts with the tides, creating strong tides [Fer et al. (2010)]. The event in October is the weakest of the three.

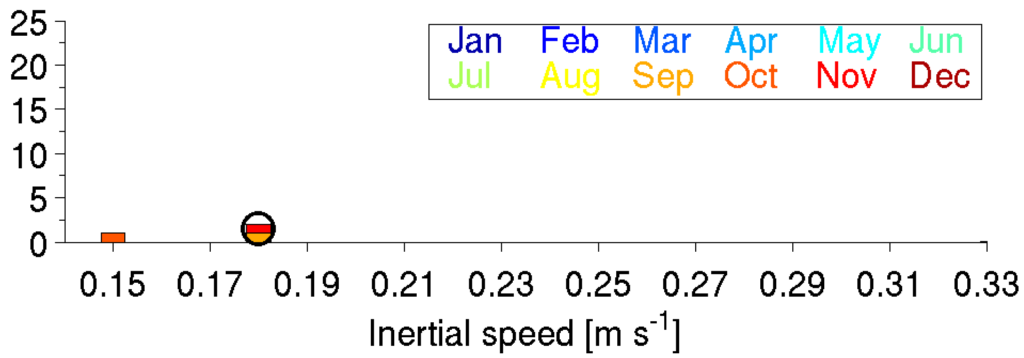

Figure 4.5: Bar plots showing the number of events in 2013 as a function of the inertial speed. The events are grouped into 0.01 m s^{-1} intervals, ranging from 0.15 to 0.32 m s^{-1}. The colours indicate how many events occur in each month. The black circles indicate the four events investigated here.

The largest fraction of the inertial events occurred in August (31%), second most in October (29%) and third most in September (20%). Only 29% occurred at location were the water depth was greater than 1000 m, figure 4.4(b).

66% occurred when the weekly averaged ice cover was less than 10% and 80% when the ice cover was less than 20%, figure 4.4(c).

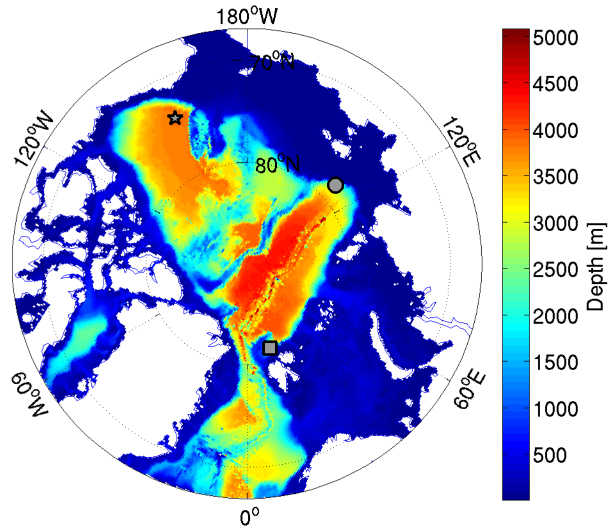

Figure 4.6: Location of the events which fulfill the three criteria. Circle: September, square: October and star: November.

In H10 both the horizontal resolution and vertical resolution are changed, compared to R26. Furthermore, the atmospheric fields are not the same and assimilation are added some of the year (see section 3.5). Therefore, only the velocity, near-inertial velocity and wind are compared between R26 and H10, as well as the monthly averaged temperature and salinity profiles.

4.2 Strength of the near-inertial waves

To investigate how strong the near-inertial waves are, they must first be separated from the rest of the wave spectrum. This can then be used to estimate the horizontal kinetic energy.

4.2.1 Separating the inertial current velocity from the rest of the velocity spectrum

As described above, inertial waves are waves with the inertial frequency. This means that they can be separated from the rest of the wave spectrum by filtering out the waves with this specific frequency. This is done using a moving average over 12 hours on the model output, which is snapshots of every hour for the surface fields, and every three hours for the three dimensional fields. This filters out all waves with a period of 12 hours, i.e. inertial waves and tides. This is then subtracted from the total wave field, leaving the inertial signal. As described in section 2.3.1, the tides are neglected in deep waters, away from land and rough bathymetry.

4.2.2 Mixed layer depth

In the Arctic Ocean the water density depends more on the salinity than the temperature [Rainville et al. (2011); Dosser and Rainville (2014); Knauss (2005); Bleck et al. (2002)]. Therefore, the mixed layer depth used here is defined in the same way as in Martini et al. (2014), as the depth were the density varies more than 0.05 kg m^{-3} from the surface value. In practice, it is the depth where the density in layer n varies more than 0.05 kg m^{-3} from the surface layer value. The mixed layer then consists of layers 1 to $k = n - 1$.

4.2.3 Calculating the near-inertial kinetic energy

The strength of the near-inertial events is estimated using the horizontal kinetic energy (HKE) of the near-inertial waves. This depends on the depth-mean density ρ_0, and the current velocity (u, v) [Martini et al. (2014)]:

$$\mathrm{HKE} = 0.5\rho_0(u^2 + v^2)_I \tag{4.1}$$

where $()_I$ is the time average over the inertial period. The kinetic energy in the mixed layer, $\mathrm{E_{ML}}$, and below it $\mathrm{E_{Below\ ML}}$ are calculated using the mixed layer depth defined above. Since the inertial frequency coincides with the frequency of the semidiurnal tide, the tides have to be removed to get the actual near-inertial kinetic energy. This is done by calculating the average velocity in the entire water column

$$\overline{\mathrm{NICS}} = \frac{\sum_{n=1}^{N} \mathrm{NICS}_n \cdot \Delta_n}{H}, \tag{4.2}$$

where $NICS_n$ is the near-inertial current speed in layer n and Δ_n the layer thickness. The total depth of the water column is $H = \sum_{n=1}^{N} \Delta_n$, where N is the total number of layers.
This average velocity is then subtracted from the total near-inertial speed for every layer:

$$\mathrm{NICS}_n^{\mathrm{NoTides}} = \mathrm{NICS}_n - \overline{\mathrm{NICS}} \tag{4.3}$$

Next, the energy in the mixed layer is calculated. This is done by calculating the energy in each of the model layers making up the mixed layer i.e.:

$$\mathrm{HKE}_n = 0.5 \cdot \rho \cdot (\mathrm{NICS}_n^{\mathrm{NoTides}})^2 \cdot \Delta_n \tag{4.4}$$

where ρ is a reference density, here set to 1027 kg m^{-3}.
The energy in the mixed layer is then

$$\mathrm{E_{ML}}[\mathrm{J\ m^{-2}}] = \sum_{n=1}^{k} \mathrm{HKE}_n, \tag{4.5}$$

with k being the deepest layer within the mixed layer. The energy below the mixed layer then becomes:

$$\mathrm{E}_{\mathrm{Below\ ML}}[\mathrm{J\ m^{-2}}] = \sum_{n=k+1}^{N} \mathrm{HKE}_n \tag{4.6}$$

The vertical distribution of near-inertial energy during the storm is calculated as:

$$\mathrm{HKE}[\mathrm{J\ m^{-3}}] = 0.5 \cdot \rho \cdot \sum_{n=1}^{N} (\mathrm{NICS}_n^{\mathrm{NoTides}})^2 \tag{4.7}$$

The kinetic energy in the mixed layer, and below it, is depth-integrated energy, whereas the energy for the entire water column is not. Therefore, to distinguish between the two, the depth-integrated energy in the mixed layer, and below it, are termed E_{ML} and $\mathrm{E}_{\mathrm{Below\ ML}}$. The energy in the entire water column is termed HKE.

The depth to which the near-inertial waves penetrate, is estimated as the deepest depth where the amount of kinetic energy is larger than a specific value, here set to the same value as in Martini et al. (2014), HKE > 0.15 J m^{-3}.

The kinetic energy is calculated for the specific locations found in section 4.1.1 as well as for two points further south. These two additional points are the two grid points closest to the original location ((ϕ_0,λ_0)=(latitude,longitude)). In addition to this, they have to be south of it and be in the longitudinal range $\lambda_0 \pm 0.5$. The reason for this last criterion is that the grid does not point north-south and east-west. This means that the closest grid-point do not have to be directly south of the original grid-point, as the grid is rotated.

5 Results for modelled events

Four events in 2005 are selected for investigation. The four cases are: 1) The strongest near-inertial event in 2005, occurring in September, 2) strong event occurring in the deep Nansen Basin in September, and the strongest events in 3) October and 4) July, see table 5.1. The location of the four events is seen in figure 5.1.
A single event in 2013 is investigated as well, the location is also shown in figure 5.1.
Below are the results for R26 in 2005 for the 4 cases. These are compared to the experiment with finer vertical resolution, V42, in section 5.2. Following this, in section 5.2.5 is R26 compared to H10. Finally, R26 and V42 are compared to observations made in 2007 and 2008/2009, to investigate how well HYCOM performs for specific events. This is described in section 6.

5.1 Case studies

5.1.1 Case 1: Strongest event in 2005

The strongest event in 2005 is found to be on the boundary between the Laptev Shelf and the Eurasian Basin, see figure 5.1. The period before, during and after the event, from the 16th to the 29th of September, are shown in figure 5.2.

The wind increases from the 16th and reaches 12.80 m s^{-1} at the 18th after which it rapidly decreases. It is followed by a stronger wind (the 'storm'), occurring late on the 19th. This wind reaches a maximum of 16.72 m s^{-1}.

The base of the mixed layer, as defined in section 4.2.2, is shown in figure 5.2(c)-(e). The mixed layer depth is 31 m at the start of the period. As the storm peaks, the mixed layer deepens to 38 m. It remains at 38 m until the 24th where it shoals to 31 m again.

Figure 5.2(b) shows the surface near-inertial current vector during the storm. As is seen, the current rotates clockwise, as would be expected for inertial currents. The first strong wind on the 18th does not generate an inertial respond, but the storm on the 19th does. The current continues to rotate throughout the period, only decreasing slowly.

At the time of the storm, the surface near-inertial current speed increases from less than 0.10 m s^{-1} to as high as 0.32 m s^{-1}, (figure 5.2(c)). Half a day after the wind peaks, the wind-generated NIWs have reached a depth of 45 m, i.e. they penetrate through the base of the mixed layer. The NIWs reach as far down as 60 m on the 21th and are present there until the 27th of September. The inertial current speed in the upper 45 m remains above the pre-storm value during the next 5 days, only slowly decreasing in strength.

The temperature change over the same period is shown in figure 5.2(d). In the beginning of

Event	Date	Location	Experiment
Case 1	September 2005	78.8°N 115.1°E	R26 V42
Case 2	September 2005	84.7°N 45.3°E	R26 V42
Case 3	October 2005	79.7°N 137.4°E	R26 V42
Case 4	July 2005	78.8°N 116.3°E	R26 V42
Case 5	November 2013	74.1°N 153.7°W	R26 H10

Table 5.1: Table showing the 5 cases investigated in this study, which month and year they occurred in, their location and which experiments are used to investigate them.

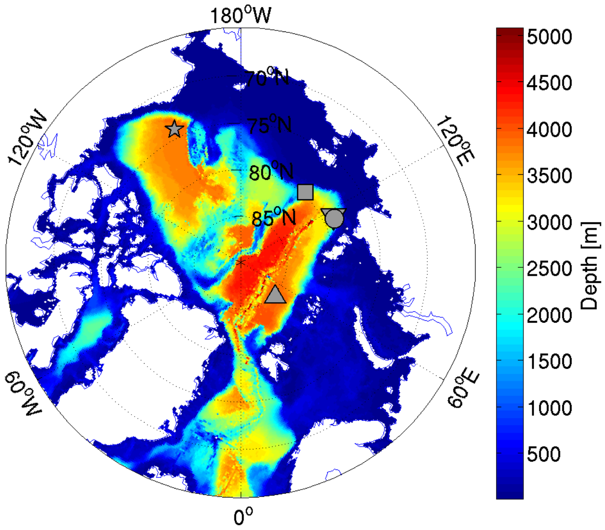

Figure 5.1: Location of cases 1-4 investigated in 2005 and case 5 in 2013. Case 1: Circle, located at 78.8°N 115.1°E, Case 2: Upward-pointing triangle, located at 84.7°N 45.3°E, Case 3: Square, located at 79.7°N 137.4°E, Case 4: Downward-pointing triangle, located at 78.8°N 116.3°E and Case 5 in 2013: Star, located at 74.1°N 153.7°W. The colour scale indicates the water depth.

the period, before the storm, the mixed layer temperature decreases from 0.17°C at the start to 0.06°C just before the storm. Below the mixed layer and down to 50 m, there is a strong stratification and below this, a temperature minimum of -1.42°C at 75 m. As the storm hits, the temperature drops 0.06°C in the first 12 hours to 0.00°C. After the storm, the mixed layer temperature cools further by 0.30°C in the following 9 days. Just below the mixed layer, the temperature increases by ~0.10 °C in the first 12 hours after the wind peaks. As the mixed layer shoals to 31 m on the 24th, the temperature of the layer just below the mixed layer increases to -0.25°C. During the rest of the period the temperature just below the mixed layer decreases. The temperature of the cold minimum at 75 m increases, causing it to 'vanish', becoming increasingly similar to the temperature of the water above and below it.

The salinity, shown in figure 5.2(e), is generally very stratified. In the three days leading up to the storm, the salinity in the mixed layer increases from 33.14 to 33.24. During and after the storm the mixed layer deepens into the stratification, causing the mixed layer salinity to increase rapidly as the storm peaks and more slowly afterwards, increasing from 33.24 psu to 33.36 psu, a total of 0.12 psu, from the time of the storm to the end of the period. This means that the mixed layer erodes into the halocline, deepening the upper limit of the halocline from 31 m to 38 m. The stratification of the halocline weakens slightly as the salinity of the upper parts increases and the lower part decreases. This results in the difference between the surface and lower layers to be less pronounced, hence the stratification weakens. From ~45 to 60 m depth the salinity decreases by 0.10 psu in the first two days after the wind peaks. After this it increases to the pre-storm salinity again. From 60 m and down the salinity remains unchanged throughout the inertial event.

Depth of the near-inertial waves

Just how deep the near-inertial waves penetrate is seen in figure 5.3, showing the horizontal kinetic energy (HKE) of the event. The majority of the near-inertial energy generated in the event is present in the mixed layer and just below it, down to 75 m. Below 75 m there are two areas of enhanced HKE (HKE > 0.15 J m^{-3}, value from [Martini et al. (2014)]), one at 125 m

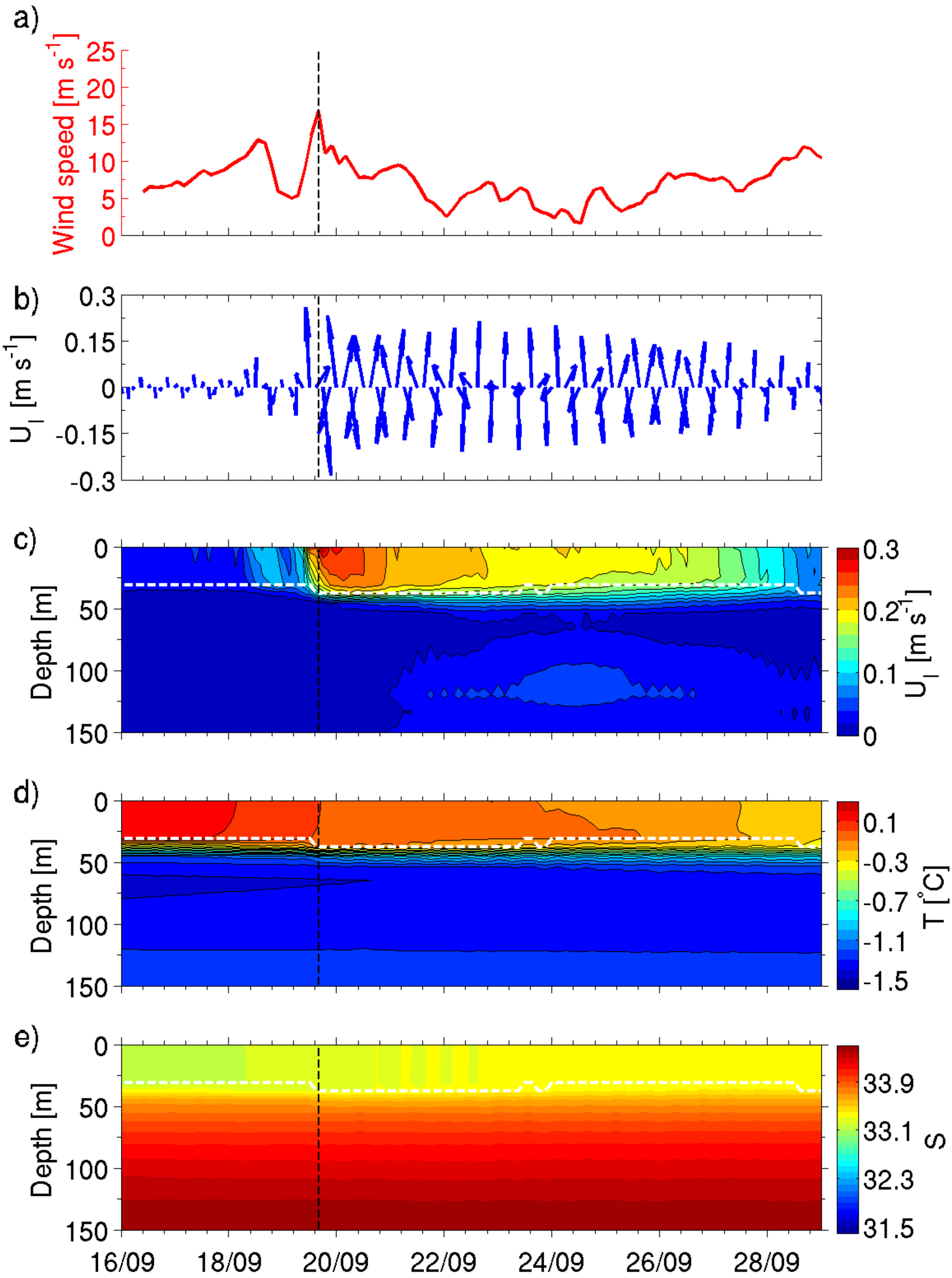

Figure 5.2: Case 1: Strongest event in September. Time series of a) wind speed, b) near-inertial surface velocity vector, c) near-inertial current speed (contour interval 0.02 m s^{-1}), d) temperature (contour interval 0.1 °C) and e) salinity (contour interval 0.1 psu). The white dashed line in c)-e) is the mixed layer depth. The vertical dashed line indicates the time of the maximum wind speed.

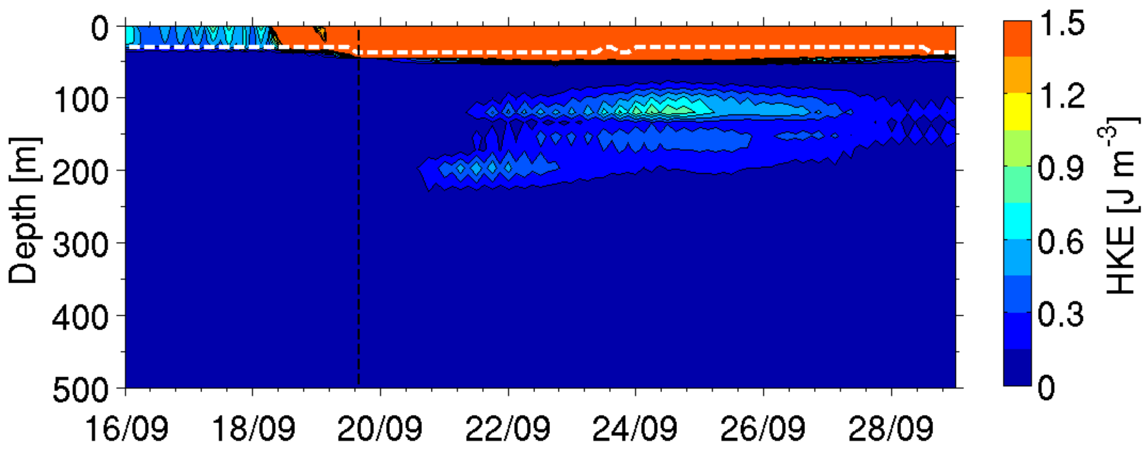

Figure 5.3: Case 1: HKE with depth for R26 (contour interval 0.15 J m^{-3}). Black dashed line indicates the time of the maximum wind speed. White dashed line indicates the mixed layer depth.HKE is enhanced for HKE > 0.15 J m^{-3}.

and one at 250 m. This shows that the near-inertial waves generated at the surface propagates down to at least 250 m.

The regions of enhanced HKE appear to be isolated from the mixed layer, i.e. the near-inertial waves appear to 'jump' from the mixed layer down to 70-100 m. In between is the energy level less than 0.15 J m^{-3}. A possible reason for this is that the near-inertial waves consists of vertical modes (a barotropic and several baroclinic modes), as described in section 2.1.2. The area with low energy between the mixed layer and the area with high energy at 100 m, is potentially the nodal point (u = 0) of one of the baroclinic modes.

Depth-integrated kinetic energy

The kinetic energy in the mixed layer and below the mixed layer, E_{ML} and $E_{Below\ ML}$ respectively, are shown in figure 5.4 for both the original location, as indicated in figure 5.1, as well as two points further south. The location of the two points further south is shown in figure 5.5. E_{ML} for the original location increases rapidly as the storm peaks on the 19th of September. The energy peaks at midnight between the 19th and 20th at 1081 J m^{-2}. In the following two days the energy decreases to 700 J m^{-2}. Over the next few days the energy decreases more slowly to ~500 J m^{-2} on the 27th. Afterwards HKE drops off rapidly to 100 J m^{-2} on the 29th.

$E_{Below\ ML}$ increases as the storm peaks, reaching around 20 J m^{-2} on the 20th and staying there until the 23rd. Here it increases to the maximum of 305 J m^{-2} on the 24th, after which it decreases to 50 J m^{-2} on the 29th. The rapid jump in energy on the 23rd and 24th could possibly be caused by the change in mixed layer depth, that oscillates between 31 and 38 m, see figure 5.2.

Propagation of energy

Figure 5.4 show E_{ML} and $E_{Below\ ML}$ for the location of the event and for two points to the south of it. The location of the two points relative to the original location is shown in figure 5.5. Figure 5.4 show the depth-integrated kinetic energy, E_{ML}, at the time of the storm on the 20th of September, is higher 19 km south of the original location, than at the original location. The energy 28 km from the original location is the lowest of the three. From the 21th the en-

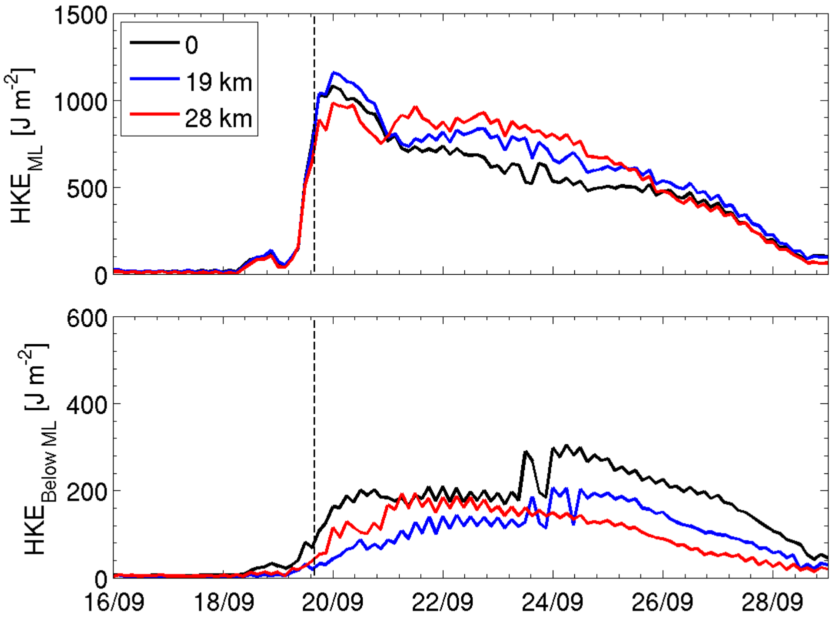

Figure 5.4: Case 1: Kinetic energy in the mixed layer (E_{ML}) and below it, ($E_{Below\ ML}$) for the original location in case 1 (black) and at two points 19 km (blue) and 28 km (red) to the south of it.

ergy increases with distance to the south, indicating that the energy appears to be propagating southward.

By comparing with figure 5.5, showing the kinetic energy in the mixed layer at the time of the storm and snapshots every day in the following 5 days, it is seen that the energy decreases with time. The core of the enhanced energy area moves slightly south, towards the point 28 km from the original location. This compares well with what is seen in figure 5.4.

The mixed layer currents flow east at the time of the storm, but shift to a more northern direction in the following days. Hence, the current advects some of the energy northward, but most propagates equatorward.

From the 20th to the 23rd the energy below the mixed layer, $E_{Below\ ML}$, is strongest at the original location. It is stronger 28 km south of the original location, than it is 19 km south of it. After the 23rd, the energy decreases with distance south of the original location. This indicates a northern transport of energy.

Comparing with figure 5.6, showing the energy at the sub mixed layer maximum (in this case at 125 m), indicate that the energy here moves northeast, increasing on the 20th, and then decreasing again until the 23rd were it starts to increase once more. This is also seen in figure 5.4. This is consistent with the energy at the original location being highest, figure 5.4. To sum up, near-inertial waves were generated by the wind on the 19th of September. This caused the mixed layer to deepen from 31 to 38 m. The near-inertial waves penetrated down to ~60 m, below the mixed layer and enhanced near-inertial kinetic energy was visible down to 350 m. The event caused a rapid cooling of 0.05°C in the first 12 hours after the storm peaked. After this rapid cooling, the temperature decreased further by 0.30°C to -0.30°C.

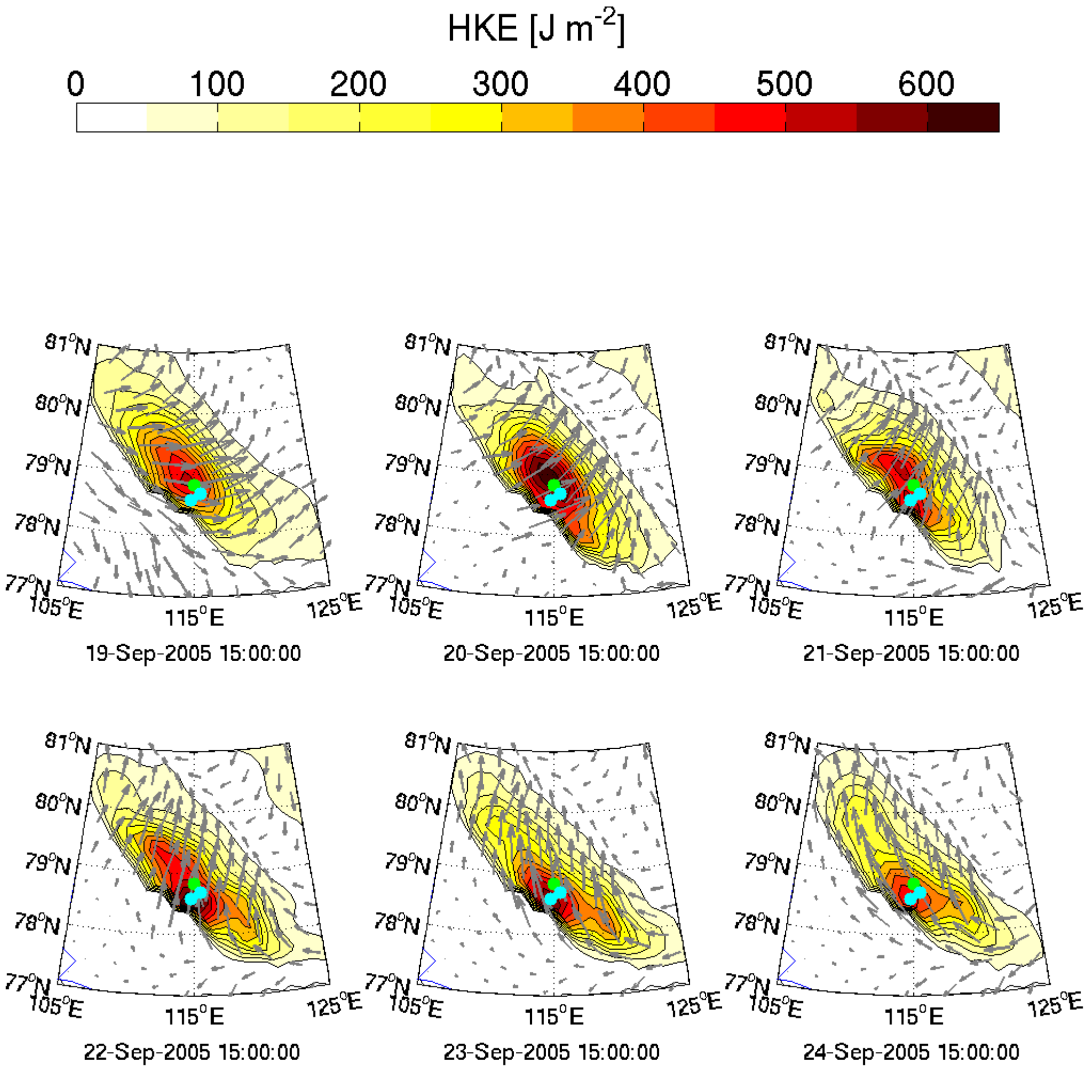

Figure 5.5: Case 1: E_{ML}. Location of case 1 is indicated by the green dot. The two blue dots indicate the two points further south used in figure 5.4.

The mixed layer deepened into the halocline, causing the halocline to deepen during and after the storm by 7 m. This resulted in an increase in the mixed layer salinity, from 33.24 to 33.36, and a weakening of the halocline.

5.1.2 Case 2: Strong near-inertial event in the Nansen Basin in September

Figure 5.7 show the same figures as in figure 5.2, but for a second strong inertial event in September. This event occurred in the Nansen Basin on the 11th of September (figure 5.1). Figure 5.7 shows the period from the 8th to the 17th of September. The wind speed has a similar evolution as in the strongest event described above in figure 5.2(a). The first strong wind reaches 14.41 m s^{-1} on the afternoon of the 9th, see figure 5.7(a). The wind peaks at 16.09 m s^{-1} on the 11th of September (the 'storm'). After this, it decreases until the 13th, where it increases once more. It continues to increase until it peaks at 16.23 m s^{-1} on the 16th.

The mixed layer depth is shown in figures 5.7(c)-(e). Before and during the storm is the base of the mixed layer at 38 m. Approximately half a day after the storm has peaked, the mixed layer deepens to 46 m, where it remains for the rest of the period. The only exception is around the 15th, where is oscillates between 46 and 52 m, before returning to 46 m.

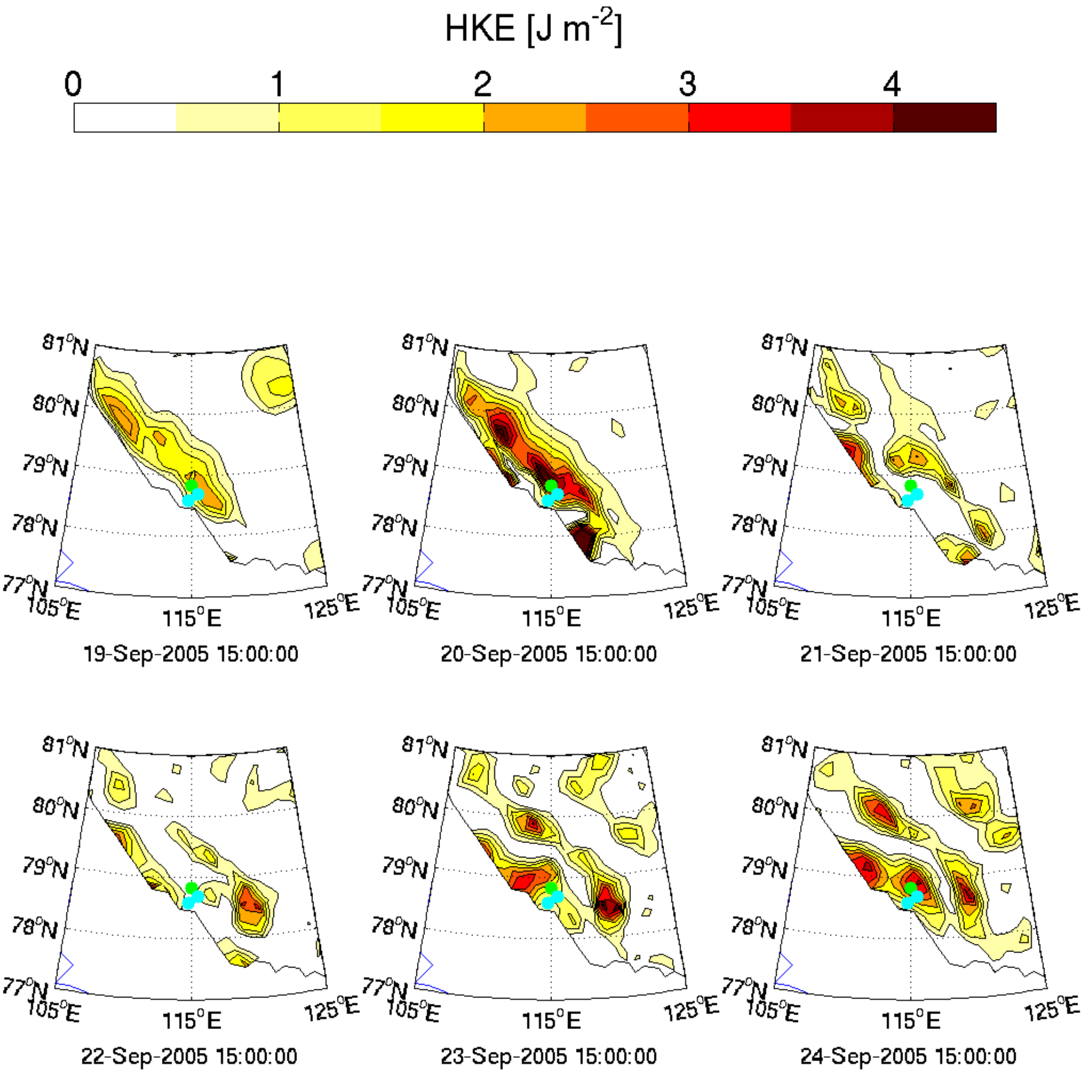

Figure 5.6: Case 1: HKE at the depth of the sub mixed layer energy maximum. Location of case 1 is indicated by the green dot. The two blue dots indicate the two points further south, used in figure 5.4.

Figure 5.7(b) shows the near-inertial surface current vectors rotating clockwise and increasing in strength as the storm peaks on the 11th. The slightly stronger wind blowing on the 16th does not induce as large an inertial signal as on the 11th of September. This can also be seen in figure 5.7(b) showing the near-inertial current speed. The maximum near-inertial speed is 0.20 m s^{-1}, which is generated by the storm on the 11th. Before the storm event, the near-inertial current speed is less than 0.05 m s^{-1}. When the storm is over, the near-inertial current speed has doubled. The NIWs penetrate down to ~60 m within the first day, but after this they deepen further, down to 75 m in the following three to four days. For the rest of the period the inertial waves propagate even further down to below 150 m. The NIWs on the 16th 'only' reaches a near-inertial speed of 0.16 m s^{-1}.

The temperature for the same period is seen in figure 5.7(d). The mixed layer temperature cools from -0.08°C at the beginning of the period to -0.47°C as the storm peaks and decreases further by 0.37°C to -0.84°C at the end. The thermocline lies between the mixed layer and the cold temperature minimum of -1.56°C at 75 m. The upper thermocline is very strong in the

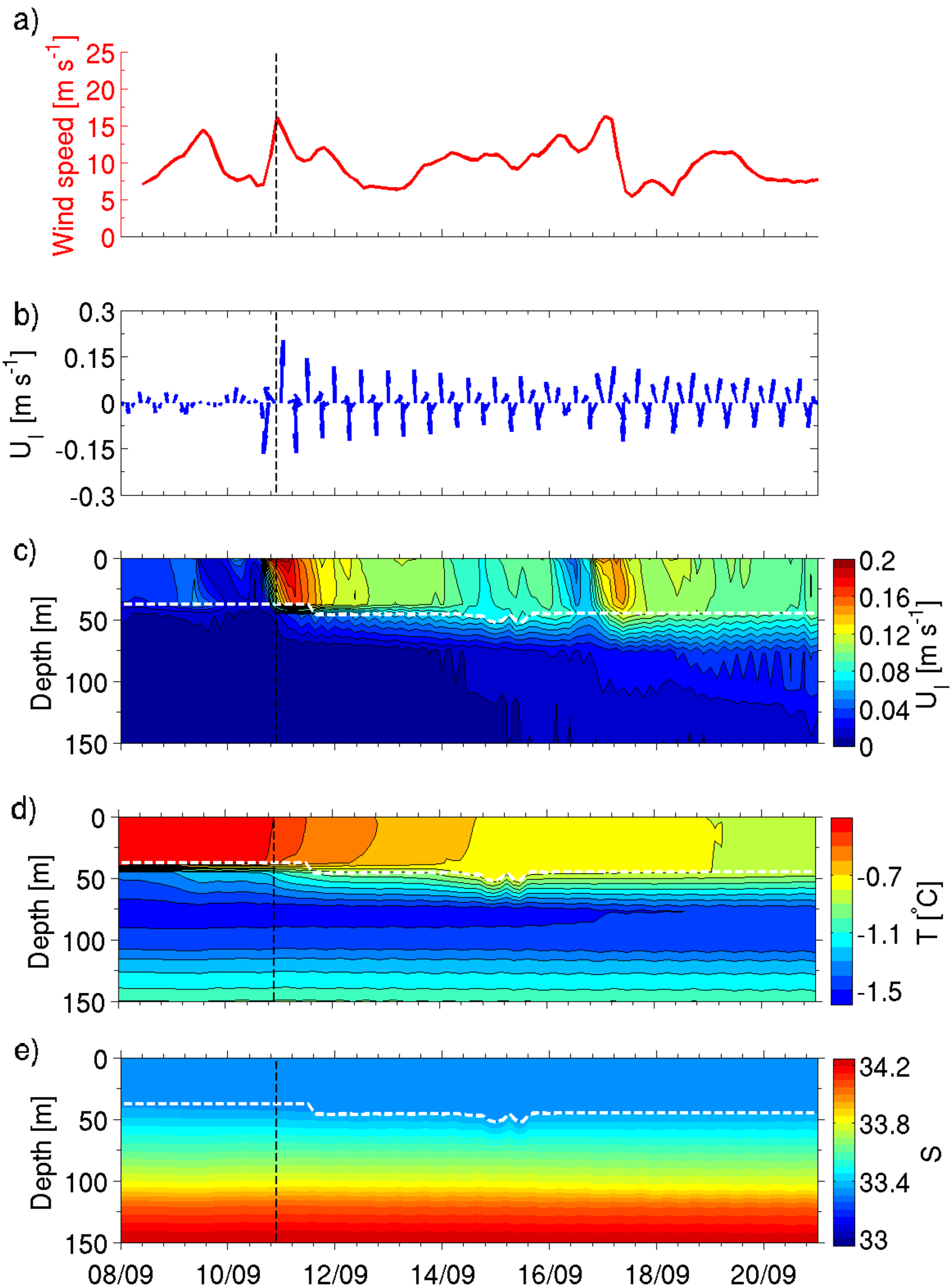

Figure 5.7: Case 2: Strongest event in September. Time series of a) wind speed, b) near-inertial surface velocity vector, c) near-inertial current speed (contour interval 0.01 m s^{-1}), d) temperature (contour interval 0.1 °C) and e) salinity (contour interval 0.05 psu). The white dashed line in c)-e) is the mixed layer depth. The vertical dashed line indicates the time of the maximum wind speed.

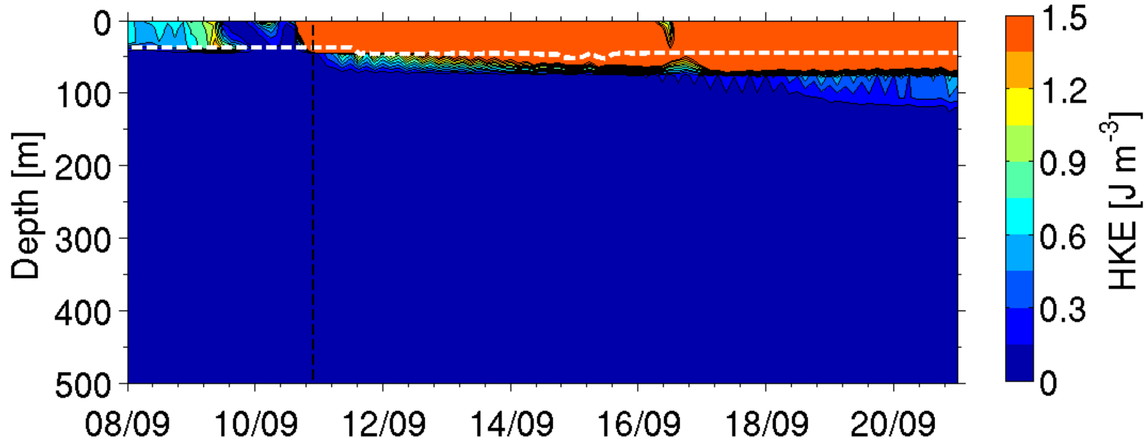

Figure 5.8: Case 2: HKE with depth for R26 (contour interval 0.15 J m^{-3}). Black dashed line indicates the time of the maximum wind speed. White dashed line indicates the mixed layer depth. HKE is enhanced for HKE > 0.15 J m^{-3}.

beginning of the period, decreasing 1.48°C in 7 m. As the first strong wind sweeps over the ocean surface on the 9th, the mixed layer starts to erode into the thermocline, cooling down the mixed layer. The uppermost of the thermocline weakens, but the rest strengthens. Over the course of time, the thermocline becomes thinner, as the mixed layer deepens and cools the upper part, while the temperature in the bottom part remains the same. The cold minimum layer becomes thinner and 'vanishes' completely on the 18th, i.e. the temperature increases and is closer to the temperature above and below the cold layer. Below 90 m the temperature does not change.

The salinity for the period is shown in figure 5.7(e). It decreases by 0.02 psu in the three days from the start of the period till the storm occurs. Afterwards, it increases from 33.31 to 33.35 psu, a difference of 0.04 psu in ten days. Below the mixed layer, the salinity does not change.

Depth of the near-inertial waves

The penetration depth of the near-inertial waves is estimated from the horizontal kinetic energy, shown in figure 5.8. There are regions of enhanced kinetic energy down to a depth of 150-160 m. The energy below the mixed layer is lower than 0.15 J m^{-3} until the 15th. Before this, the energy is confined to the mixed layer and just below.

Depth-integrated kinetic energy

The kinetic energy in the mixed layer, E_{ML} and below the mixed layer, $E_{Below\ ML}$, is seen in figure 5.4. The maximum E_{ML} of 579 J m^{-2} is reached as the storm peaks. It then decreases, first rapidly, than slower until the second strong wind peaks on the 16th. Here, the E_{ML} increases to 439 J m^{-2}, followed by the same pattern: first a rapid decrease, then a slower decrease.

The energy below the mixed layer, $E_{Below\ ML}$, peaks at 143 J m^{-2} a few hours after the storm has peaked. $E_{Below\ ML}$ rapidly decreases to ∼40 J m^{-2} in about 6 hours. It then starts to increase again until the 17th of September, where it quickly drops, immediately followed by a fast increase to its maximum of 250 J m^{-2} on the 17th. After this, it slowly decreases again. This second wave of energy is probably generated from the second strong wind on the 16th.

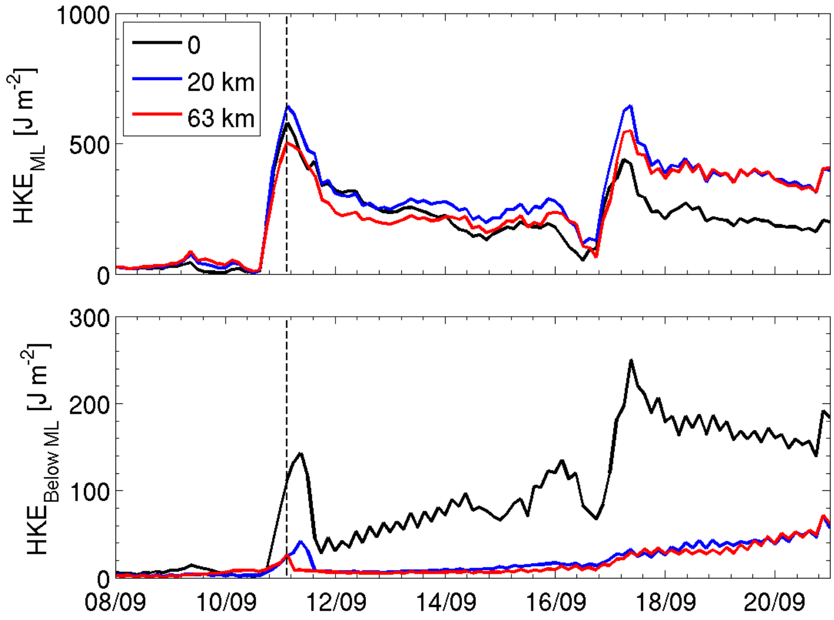

Figure 5.9: Case 2: Kinetic energy in the mixed layer (E_{ML}) and below it, ($E_{Below\ ML}$) for the original location in case 2 (black) and at two points 19 km (blue) and 28 km (red) to the south of it.

Propagation of energy

Figure 5.9 shows E_{ML} and $E_{Below\ ML}$ at the original location as well as two points 20 km and 63 km south of the original point. At the time of the storm, the energy in the mixed layer is higher 20 km south of the original location than at the original location. 63 km south of it, it is lower. From the 13th of September, the energy is the lowest at the original site and strongest 20 km south of it. The energy on the 11th and the 17th are comparable in strength, for the two points to the south of the original location. This indicates that the maximum energy is found 20 km south of the original point.

The energy below the mixed layer, $E_{Below\ ML}$, decreases rapidly within the first 20 km south of the original location. The energy 63 km south of the original site is of comparable magnitude to the energy 20 km away. At the original location, the mixed layer energy does not decrease much with distance, but below the mixed layer the energy decreases rapidly with distance.

Figures 5.10 and 5.11 shows the energy over a larger horizontal area in the mixed layer and at the depth of the maximum energy below the mixed layer, in this case just below the mixed layer. The figures show that the energy in the mixed layer decreases with time and moves eastward, following the direction of the current. This is not what is seen in figure 5.9(a), where the energy is largest 20 km to the south of the original point. The point is slightly to the east as well, but it does not appear to be enough to explain the higher energy here. Below the mixed layer, the energy is at its maximum as the storm peaks, but rapidly falls off in the following day. After this it starts to increase again, northeast of the original location. This coincides well with what is seen in figure 5.9, that the energy is much higher at the original location than south of it.

For this second event in September, near-inertial waves are generated, the mixed layer cools after the storm peaks and the salinity increases. The mixed layer deepens into the halocline.

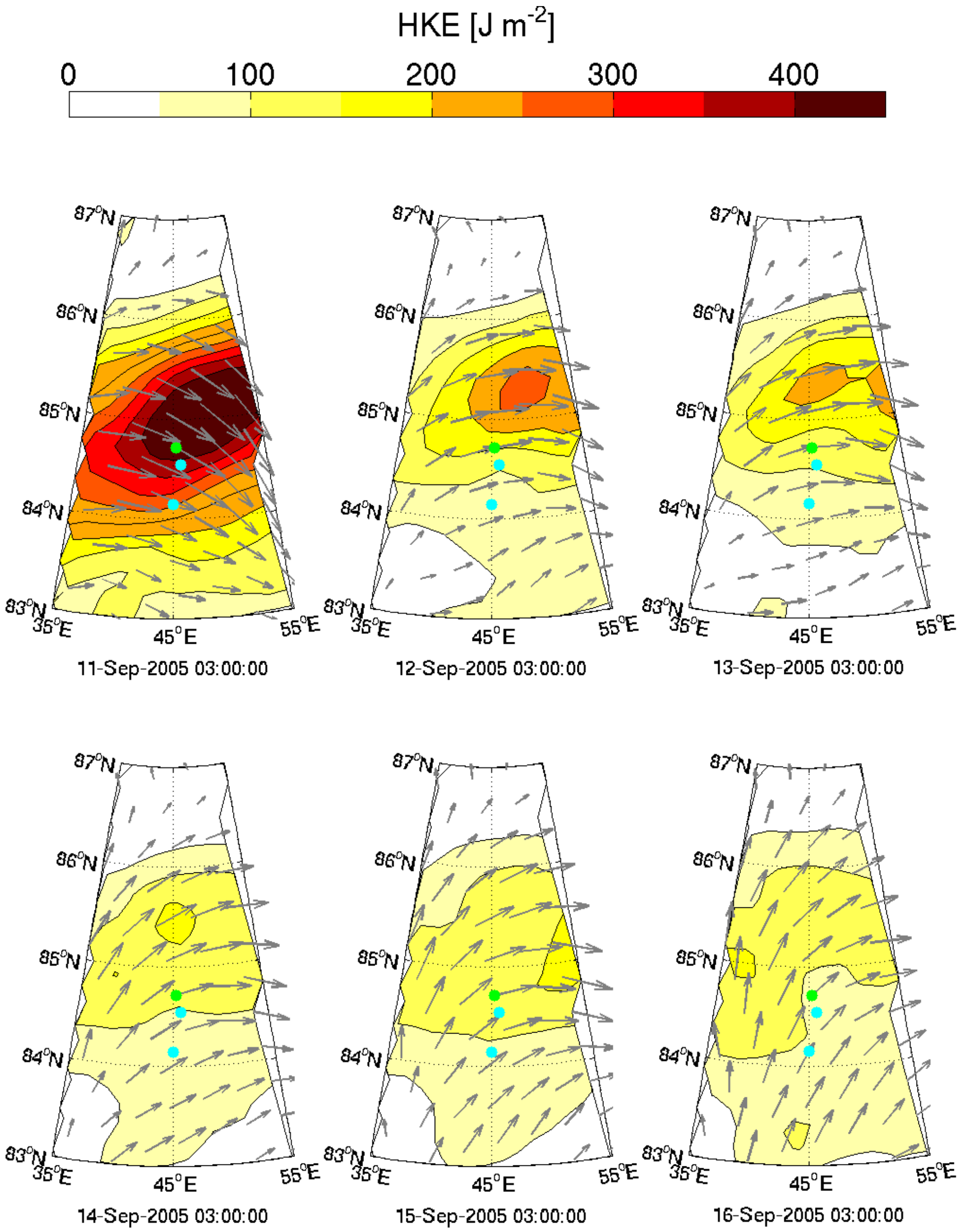

Figure 5.10: Case 2: E_{ML}. Location of case 2 is indicated by the green dot. The two blue dots indicate the two points further south used in figure 5.9.

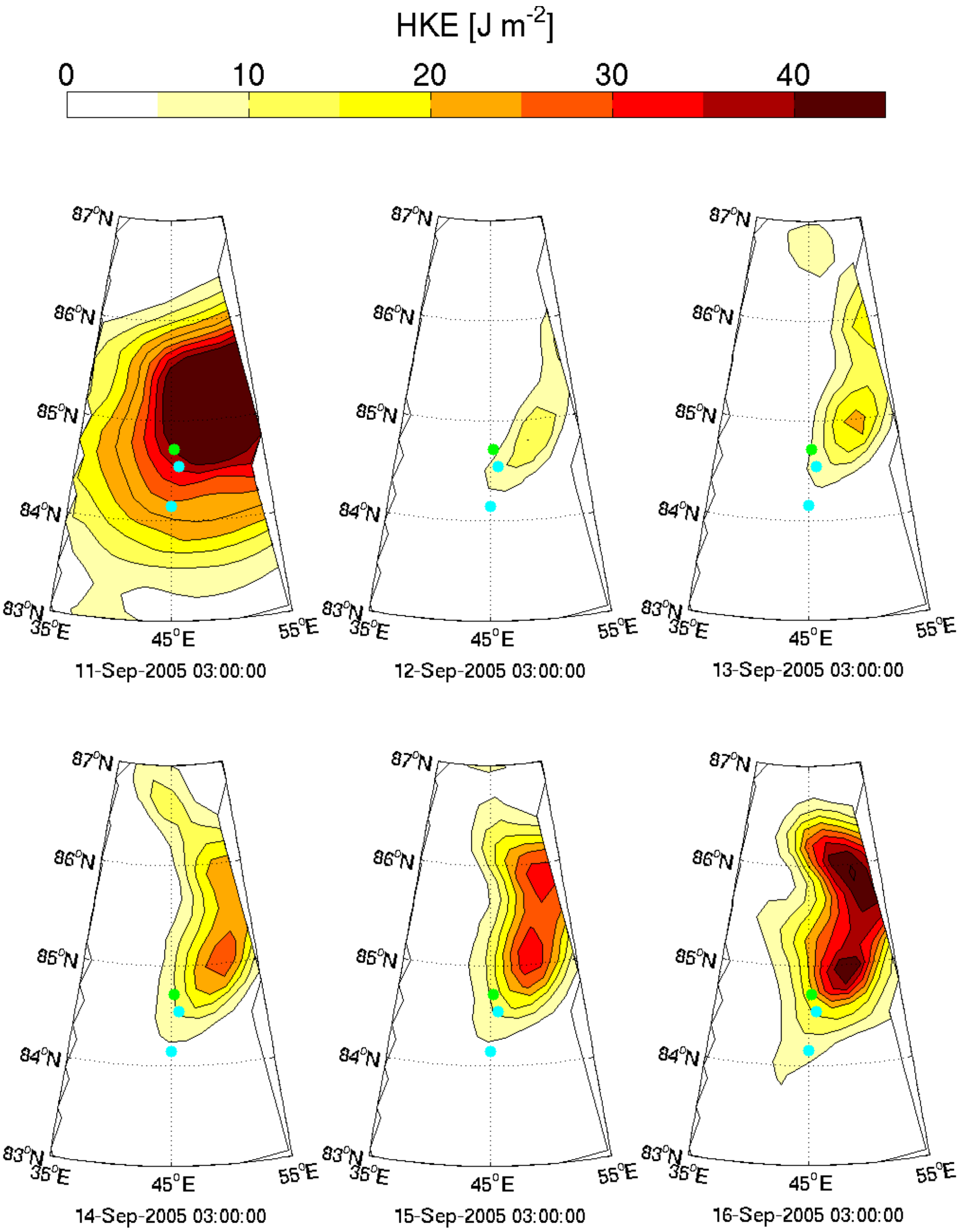

Figure 5.11: Case 2: HKE at the depth of the sub mixed layer energy maximum. Location of case 2 is indicated by the green dot. The two blue dots indicate the two points further south, used in figure 5.9.

The near-inertial waves penetrate down into the halocline, to at least 150 m. Enhanced near-inertial energy is visible down to 150-160 m. The temperature decreases with depth, so warm water can not be drawn up to the surface.

5.1.3 Case 3: Strongest near-inertial event in October

The strongest inertial event in October occurred around the 25th in the Eurasian Basin, very close to where the Lomonosov Ridge connects to the Laptev Shelf (figure 5.1).

The wind is relatively weak in the days leading up to the event, see figure 5.12(a). From

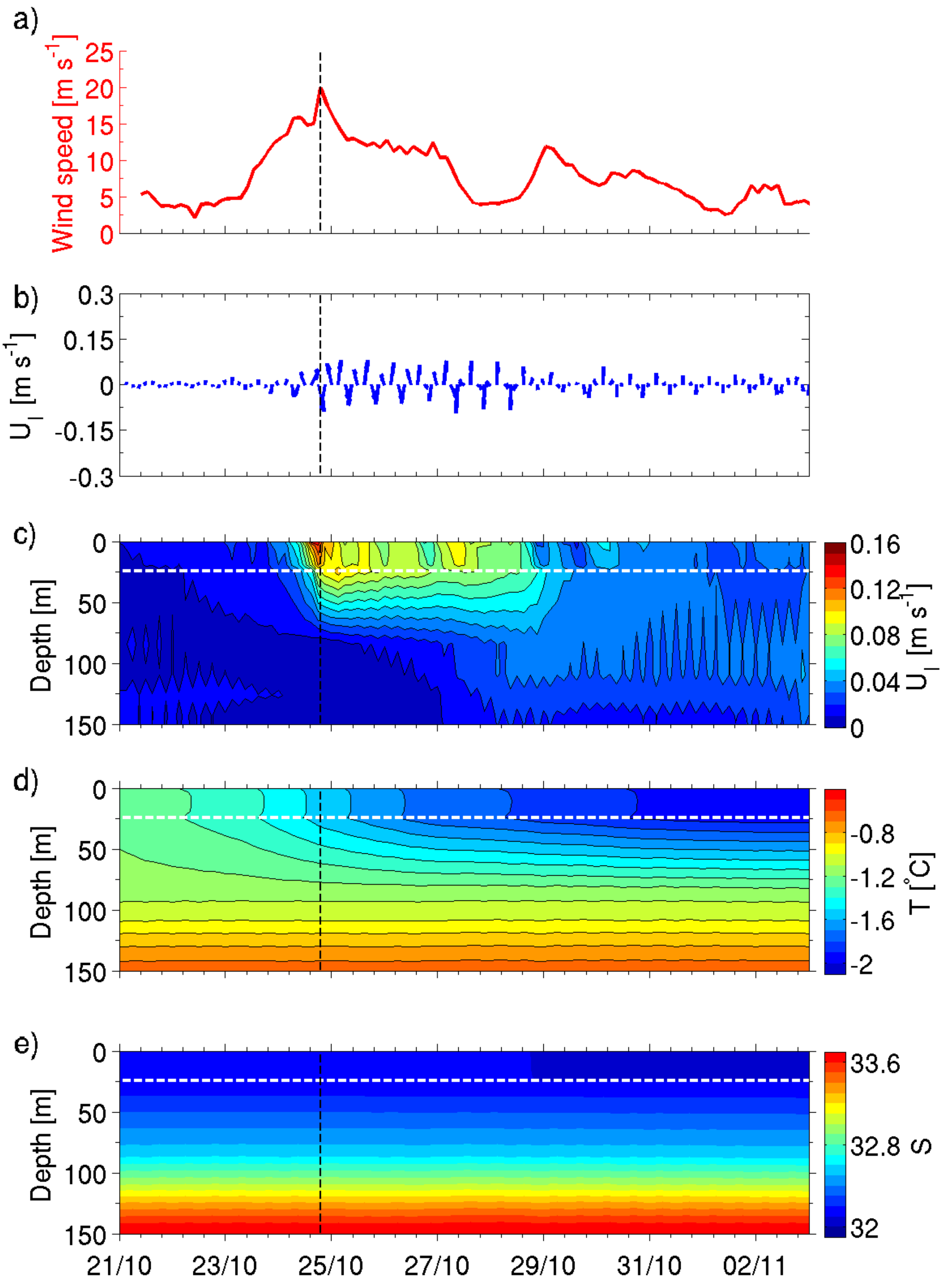

Figure 5.12: Case 3: Time series of a) wind speed, b) near-inertial surface velocity vector, c) near-inertial current speed (contour interval 0.01 m s^{-1}), d) temperature (contour interval 0.1 °C) and e) salinity (contour interval 0.1 psu). The white dashed line in c)-e) indicates the mixed layer depth. The vertical dashed line indicates the time of the maximum wind speed.

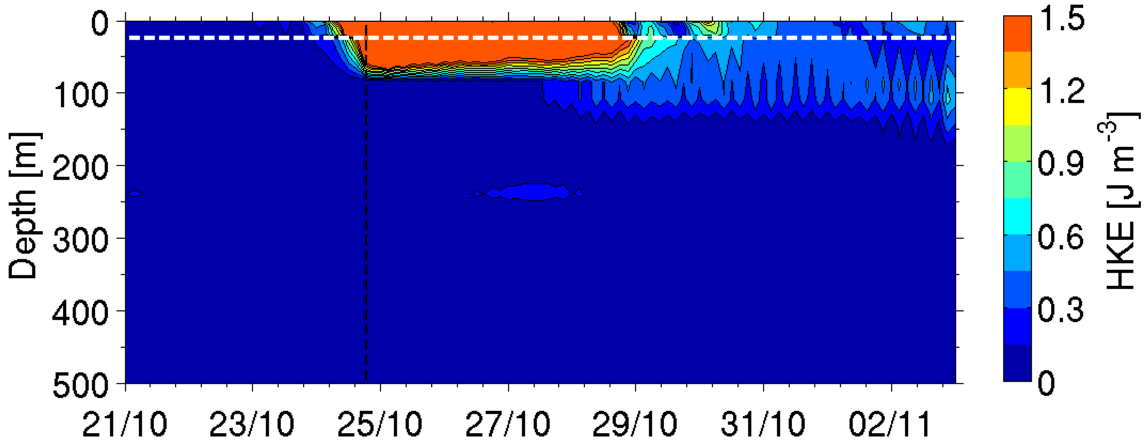

Figure 5.13: Case 3: HKE with depth for R26 (contour interval 0.15 J m^{-3}). Black dashed line indicates the time of the maximum wind speed. White dashed line indicates the mixed layer depth. HKE is enhanced for HKE > 0.15 J m^{-3}.

around the 23rd of October the wind begins to increase, reaching a maximum of 19.94 m s^{-1} on the 25th. After this, the wind speed decreases to around 12.00 m s^{-1} where it remains until the 27th. In the rest of the period it increases to 12.41 m s^{-1} on the 29th.

The mixed layer depth remains at 25 m throughout the storm, but by looking at the temperature in figure 5.12(d), it appears that the mixed layer depth in the beginning of the period should be down at 85 m. Instead, it is at 25 m. A possible reason for this is in the method used for determining the mixed layer depth. In this study the mixed layer depth is determined, as the shallowest depth where the density differs more than 0.05 kg m^{-3} from the surface value. The depth used is the boundaries between the layers. The layers in R26 are very thick, in particular in October at the location of case 3. Between 25 and 85 m there is only one layer, see figure 5.22 in section 5.2. Due to this, the density difference between 25 m and 85 m during the entire period in case 3, is more than than 0.05 kg m^{-3}. In this case, the density on the 8th of October at 25 m is 1025.82 kg m^{-3} and at 85 m it is 1026.18 kg m^{-3}.

Figure 5.12(b) shows the near-inertial surface velocity as a function of time. The near-inertial current rotates clockwise, is enhanced as the wind peaks on the 24th and slowly decreases over the next few days. The near-inertial speed with depth is seen in figure 5.12(c). First of all, it is weaker than the two events in September (figures 5.2 and 5.7). Before the storm, the near-inertial speed is 0.01-0.02 m s^{-1}. As the wind increases, the near-inertial speed builds up and peaks at 0.12 m s^{-1}. After the storm the near-inertial speed decreases. The near-inertial waves generated by the wind, appear to penetrate far below the mixed layer, all the way down to 75 m in the first few days, and later down below 150 m.

As opposed to the two events in September described above, the temperature increases with depth in October, see figure 5.7(d). The temperature of the mixed layer, going down to 25 m, decreases from -1.23 to -1.95 °C from the 21st of October to the 3rd of November. The greatest temperature change in the mixed layer coincides with the storm. Below the mixed layer is the thermocline which strengthens as the mixed layer cools down and the temperature below 90 m is unchanged.

The salinity in figure 5.7(e) does not change below the mixed layer. In the mixed layer, the

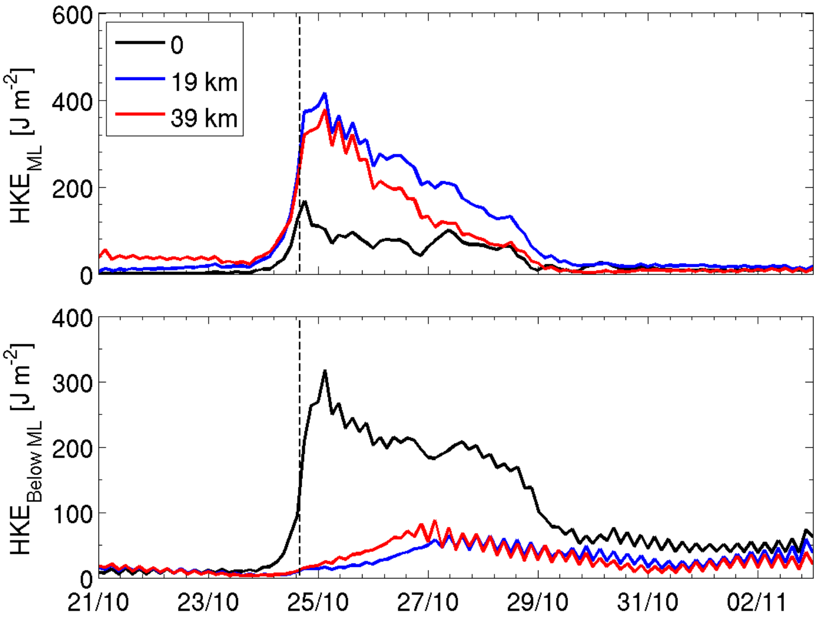

Figure 5.14: Case 3: Kinetic energy in the mixed layer (E_{ML}) and below it, ($E_{Below\ ML}$) for the original location in case 3 (black) and at two points 19 km (blue) and 28 km (red) to the south of it.

salinity decreases by 0.01 psu through the shown period.

Depth of the near-inertial waves

The kinetic energy of case 3 in October is seen in figure 5.13. As seen in figure 5.12, the near-inertial waves penetrate down below the mixed layer, down to 75 m. From the 27th of October, the HKE is enhanced (HKE >0.15 J m^{-3}) down to 170-200 m. The energy generally decreases with depth, except for at the end of the period, where the energy at 100 m is higher than in the mixed layer. This indicates an inertial wave propagating downwards. At about 200 to 250 m there is enhanced near-inertial energy from the 26th to th 28th.

Depth-integrated kinetic energy

The energy in the mixed layer and below the mixed layer are shown in figure 5.14. E_{ML} increases as the wind increases and peaks at 167 J m^{-2}, a few hours after the wind has peaked. The energy decreases slowly, reaching 60 J m^{-2} late on the 28th. Over the next day it decreases rapidly to around 10 J m^{-2}, where it stays for the rest of the period.

$E_{Below\ ML}$ is actually greater than E_{ML}. Before the storm, the energy decreases from 10 to 5 J m^{-2}. As the wind builds up on the 24th-25th, the energy increases rapidly, reaching its maximum value of 318 J m^{-2}. It then relatively slowly decreases to 150-160 J m^{-2} on the 29th, where it drops rapidly to around 50 J m^{-2}.

Propagation of energy

E_{ML} and $E_{Below\ ML}$ for the original location and two locations further south are shown in figure 5.14. E_{ML} at the original location is only half of the energy 19 km south of it. The energy 38

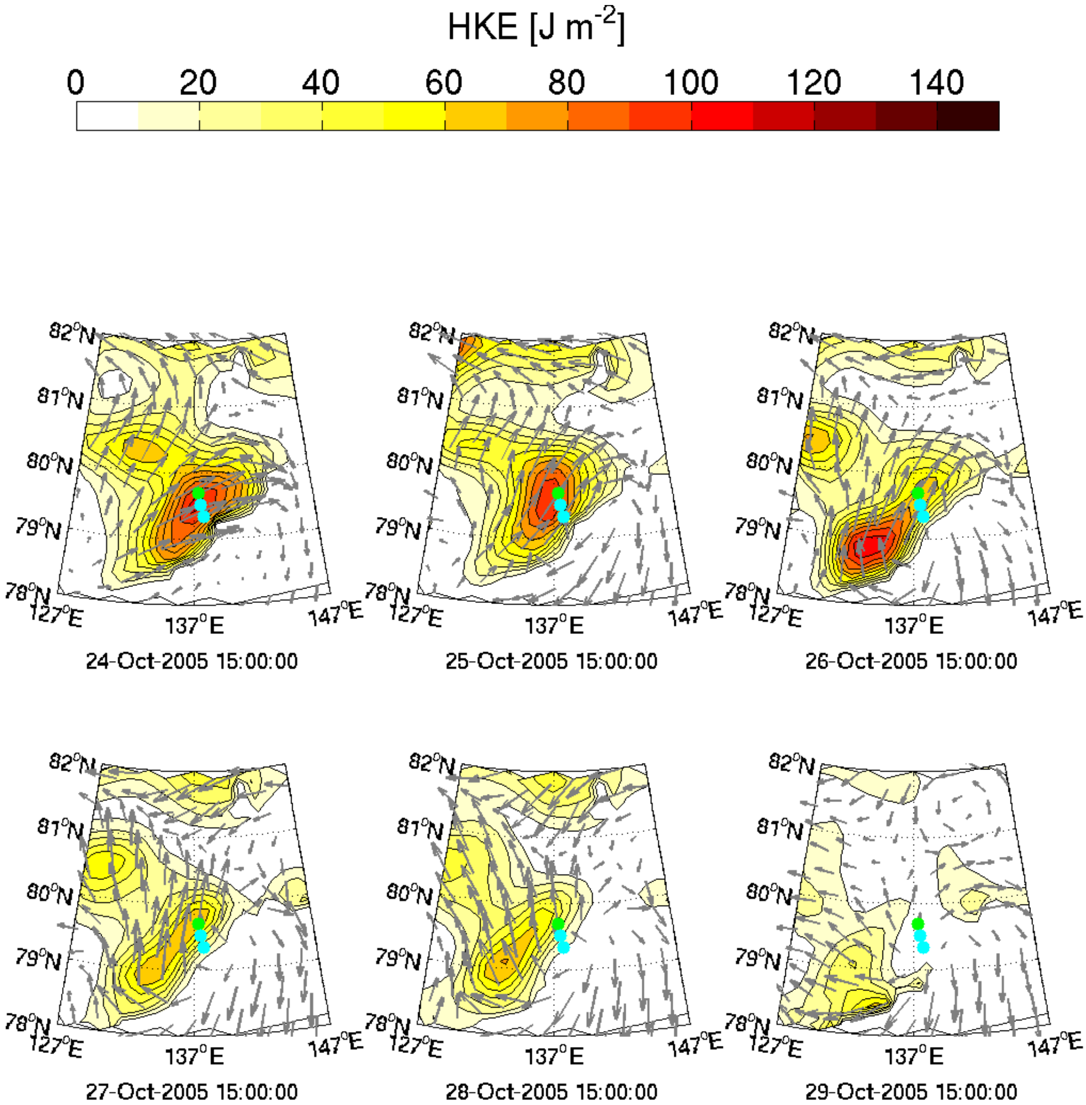

Figure 5.15: Case 3: E_{ML}. Location of case 3 is indicated by the green dot. The two blue dots indicate the two points further south used in figure 5.14.

km from the original location is comparable to the energy 19 km from the original location, but slightly lower. This causes the energy below the mixed layer to be much lower 19 and 39 km south of the original location. It is lowest 19 km south of it. Comparing this to the energy shown in figure 5.15 and 5.16 it is seen that most of the mixed layer energy propagates south-southwest and only a minor part of the energy advect along with the currents flowing north-northwest. This compares well with what is seen in figure, 5.14, i.e. the energy is much larger south of the original location.

Below the mixed layer, it is a bit more difficult to see which way the energy moves. In the first few days, it appears as if the energy does not move significantly, it increases from the 24th to the 25th of October and then decreases again on the 26th. From the 27th it appears to be moving toward the northeast. The energy is much higher at the original location than to the south of it, as was also seen in figure 5.14.

This event is weaker than the two in September. The very coarse vertical resolution indicate that the density gradient with depth (thus the stratification) is very weak. This allows for

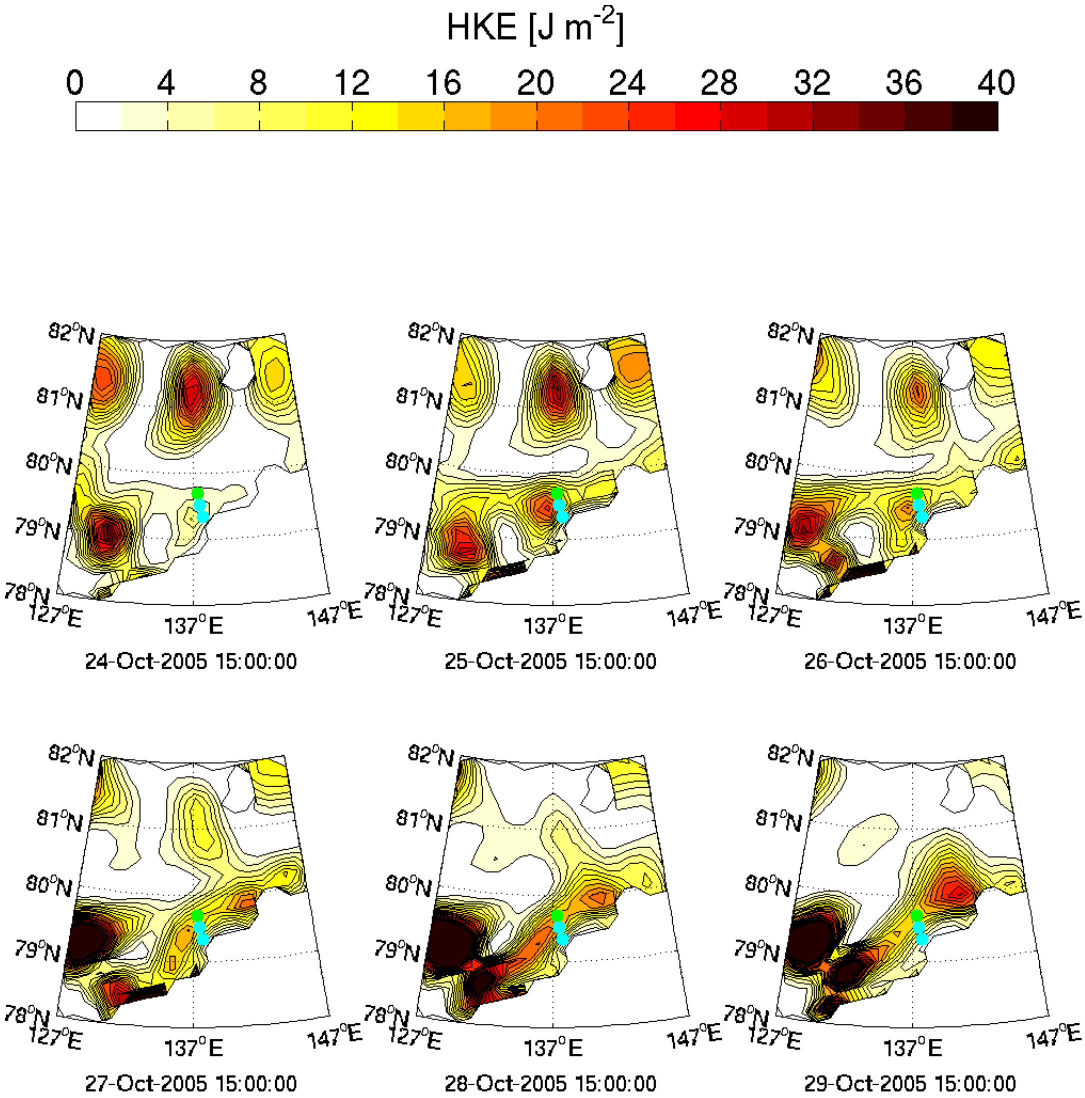

Figure 5.16: Case 3: HKE at the depth of the sub mixed layer energy maximum. Location of case 3 is indicated by the green dot. The two blue dots indicate the two points further south, used in figure 5.14.

more mixing to occur, hence the NIWs can penetrate deep down in this case. The NIWs in case 3 decreases slower with depth, compared to what is seen in cases 1 and 2 in sections 5.1.1 and 5.1.2. As the storms are generally stronger in the fall, peaking in October [Martin et al. (2014)], the stratification weakens. Therefore, the weaker stratification seen in case 3, compared to cases 1 and 2, is realistic. The mixed layer cools throughout the period, slightly faster during the storm. The salinity decreases by 0.01 psu throughout the period.

The mixed layer energy moves southwest and thus the energy increases the further south it moves. Below the mixed layer the energy at the original location is much higher than further south. It appears as if the energy moves southwest. However, The region of enhanced energy is very narrow, causing the two points to the south to be less energetic then at the original location.

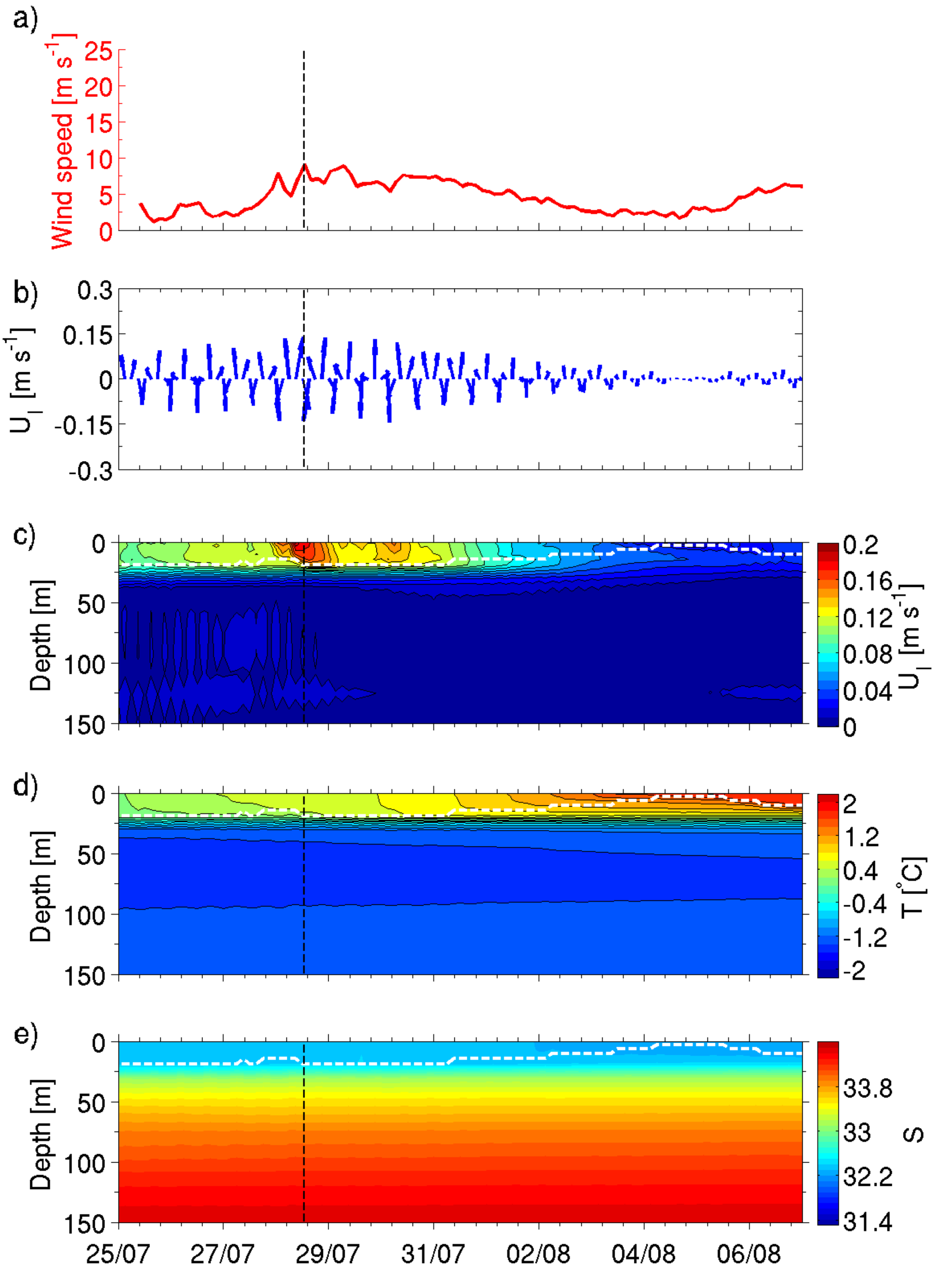

Figure 5.17: Case 4: Time series of a) wind speed, b) near-inertial surface velocity vector, c) near-inertial current speed (contour interval 0.01 m s^{-1}), d) temperature (contour interval 0.2 °C) and e) salinity (contour interval 0.1 psu). The white dashed line in c)-(e) indicates the mixed layer depth. The vertical dashed line indicates the time of the maximum wind speed.

5.1.4 Case 4: Strongest event in July

The strongest event in July occurred on the 28th. Figure 5.17 shows the results for this case. It is located near the location of the strongest event of year, on the boundary between the Laptev Shelf and the Eurasian Basin, at 78.8°N 116.3°E.

The wind is the weakest of the 4 cases investigated here, increasing from around 2-3 m s^{-1} on the 27th of July to the maximum of 'only' 9.07 m s^{-1} on the 28th (the 'storm'). It fluctuates between 5 and 9 m s^{-1} until the 31st, after which it decreases (figure 5.17(a)).

The mixed layer depth is shown in figure 5.17(c)-(e). Before the storm the mixed layer depth is 19 m. Just before the storm it shoals to 14 m, but as the storm peaks it deepens again to 19 m. Here it remains until the 31st, where it first shoals to 14 m again. In the following days it shoals even further, until it is at its thinnest of 3 m on the 4th and 5th of August. From the 5th it starts to deepen again.

The near-inertial velocity vector shown in figure 5.17, indicate that there is near-inertial activity already before the storm occurred. The storm only slightly enhanced the near-inertial velocity. The near-inertial speed shows the same trend. Before the storm the near-inertial speed is ~0.08-0.1 m s^{-1} and the near-inertial waves penetrate down to approximately 35 m. The storm causes the near-inertial speed to increase to a maximum of 0.15 m s^{-1} at the surface. On the 30th, the near-inertial waves penetrate below 35 m, down to 45-50 m.

The mixed layer temperature increases during the storm, from 0.20°C on the 25th of July to 1.60°C on the 7th, peaking at 1.87°C on the 5th, when the mixed layer is the shallowest, figure 5.17(d). This is most likely caused by solar insolation, since the water below is colder than the surface water and a thin mixed layer warms up faster than a thick one.

The salinity is unchanged below 25 m. Above, it decreases from 32.38 psu on the 25th to 32.25 on the 7th.

Depth of the near-inertial waves

The near-inertial waves penetrate just below the mixed layer depth, down to 40 m, see figure 5.18.

Depth-integrated kinetic energy

The amount of energy in the mixed layer and below it is seen in figure 5.19. E_{ML} increases from around 100 J m^{-2} before the storm to a maximum of 315 J m^{-2} as the storm peaks. The energy then decreases, with a small increase on the 30th, reaching 230 J m^{-2}. This increase coincides with an increase in the wind speed.

The energy below the mixed layer is around 50 J m^{-2} before the 27th of July. The increase in energy between the 27th and the peak of the storm is probably a result of the change in the mixed layer depth. During the period before the storm, the energy below the mixed layer peaks at 103 J m^{-2}. After the storm has peaked the energy decreases with time, except for around the 31th, were it rapidly increases again. This again coincides with a change in the mixed layer depth.

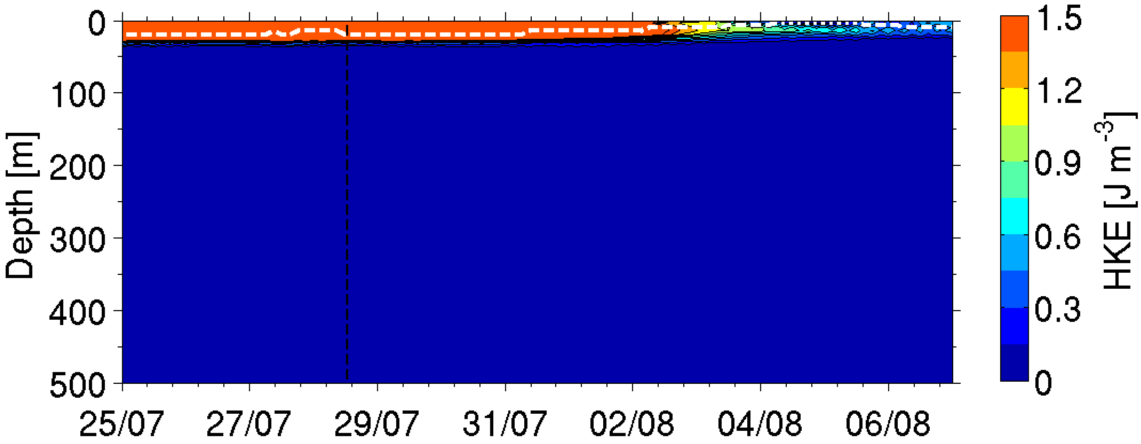

Figure 5.18: Case 4: HKE with depth for R26 (contour interval 0.15 J m^{-3}). Black dashed line indicates the time of the maximum wind speed. White dashed line indicate the mixed layer depth. HKE is enhanced for HKE > 0.15 J m^{-3}.

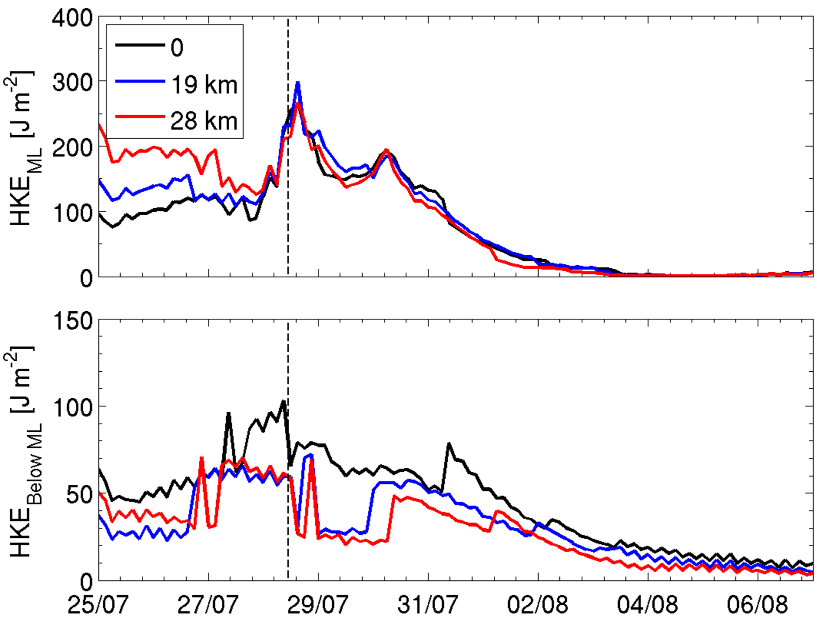

Figure 5.19: Case 4: Kinetic energy in the mixed layer (E_{ML}) and below it, ($E_{Below\ ML}$) for the original location in case 4 (black) and at two points 19 km (blue) and 28 km (red) to the south of it.

Propagation of energy

E_{ML} increases with southern distance from the original location from the 25th to a few hours before the storm peaks, figure 5.19. For the rest of the period, the energy is very similar at the original point and at the two points south of it. Below the mixed layer the energy is generally higher at the original location than further south.

Comparing this with figure 5.20 and 5.21 it is seen that the core of the enhanced mixed

Case	Max NICS [m s^{-1}]	MLD	Pen. Depth [m]	Depth of sub-ML HKE [m]	Max E_{ML} [J m^{-2}]	Max $E_{Below\ ML}$ [J m^{-2}]
1	0.32	Deepens from 31 to 38 m	350	125	1081	305
2	0.20	Deepens from 38 to 46 m	150-160	Just below ML	579	250
3	0.14	25 m	200	Just below ML	167	318
4	0.20	19 m during storm, shoals with time	40	Just below ML	264	103

Table 5.2: Table showing the maximum near-inertial current speed (NICS), the mixed layer depth (MLD), the penetration depth of the near-inertial waves, the depth of the maximum kinetic energy below the mixed layer, and the maximum depth-integrated kinetic energy in the mixed layer and below the mixed layer. Results are for the reference experiment R26.

layer energy, E_{ML}, does not appear to move significantly in the first 3 days after the storm. Some of the energy moves northwest, but the core of the energy is more or less at the same location. From the 31th of July and to the 2nd of August the energy moves northward, in the same direction as the mixed layer currents. From figure 5.19 the energy appears to be the same for all three points, but in figure 5.20 the energy appears to be greater at the original location. $E_{Below\ ML}$ in figure 5.20 appears to be moving towards the northeast. This is compatible with what is seen in figure 5.19.

The event in July is the weakest of the 4 cases investigated here. The mixed layer is very thin and the near-inertial waves do no penetrate very far below it. The temperature rises and the salinity decreases.

The inertial current velocities in July are stronger than in October, but the wind speed in July is weaker than in October. The stronger inertial currents, in spite of the weaker winds, could be the result of the mixed layer being thinner in July. In this case, the near-inertial energy input from the wind has to be distributed over a thinner layer than in October [Rainville et al. (2011)]. HKE in case 4 does not appear to move much in the mixed layer from the 28th to the 31st. The energy is at maximum at the original location below the mixed layer, moving north-east. In the mixed layer, the energy does not decrease very strongly with southern distance, but from figure 5.20 the energy appears to be greater to the north than to the south.

5.1.5 Summary

In all four cases are the near-inertial waves seen to penetrate into the mixed layer and the underlying halocline, see table 5.2. In none of them does this cause warm water to be drawn closer to the surface. Only in case 3 is the water relatively close to the surface warmer than the surface water. Here, the mixed layer cools, and the storm accelerates the cooling.
Therefore, in these four cases do the near-inertial waves not appear to cause a warming in the surface waters. The thermo- and halocline shoaled and strengthened in July and October (cases 3 and 4). In September, the thermo-and halocline deepened and weakened.

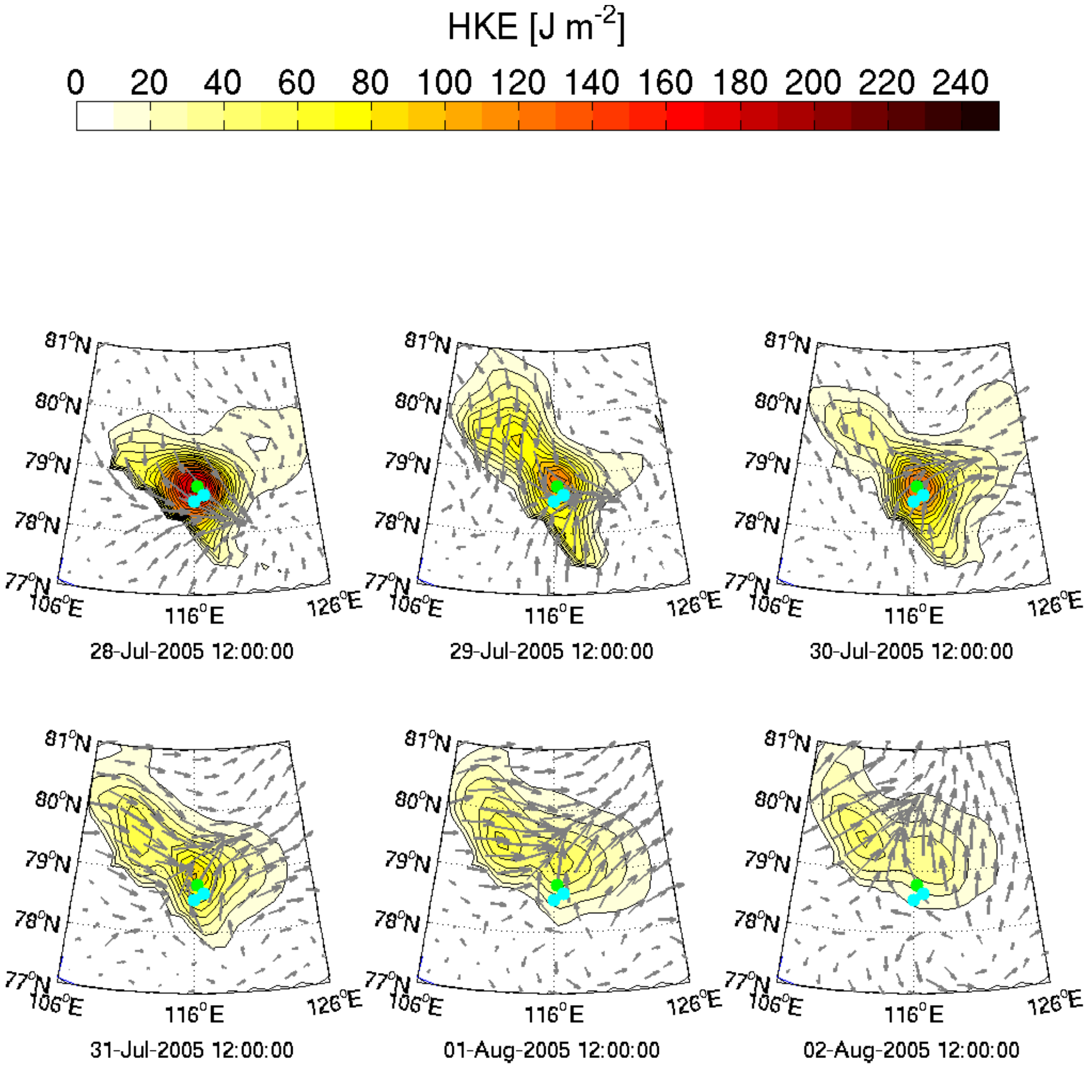

Figure 5.20: Case 4: E_{ML}. Location of case 4 is indicated by the green dot. The two blue dots indicate the two points further south used in figure 5.19.

5.2 Model sensitivity - Comparing R26 to V42 and H10

The results shown in section 5 are from the reference experiment R26. In addition to this, an experiment with an increased number of vertical layers is run, see section 3.5. The consequence of increasing the number of vertical layers is seen in figure 5.22. For all four cases shown here, there are more (hence thinner) layers in V42. This is especially clear for case 3, occurring in October. In R26, there is one layer between 25 and 85 m whereas there are seven layers in the same range in V42. Even though the layers are isopycnal below 20 m in both R26 and V42, the layers in V42 are constant with time, whereas the layers in R26 vary in time. This is due to the layers being isopycnal. As explained in section 3.1.3, each layer is determined from a specific density. If the densities in two adjacent layers are too close, causing the two layers to be very thin, the layers are set to a minimum thickness. This results in layers that do not vary in thickness in time, as is seen for V42.

To compare R26 and V42 both datasets are linearly interpolated to the same vertical grid, with a layer thickness of 5 m. The difference between R26 and V42 is defined as $s_{R26} - s_{V42}$, so that a negative difference comes from a higher variable value in V42 than in R26. The result

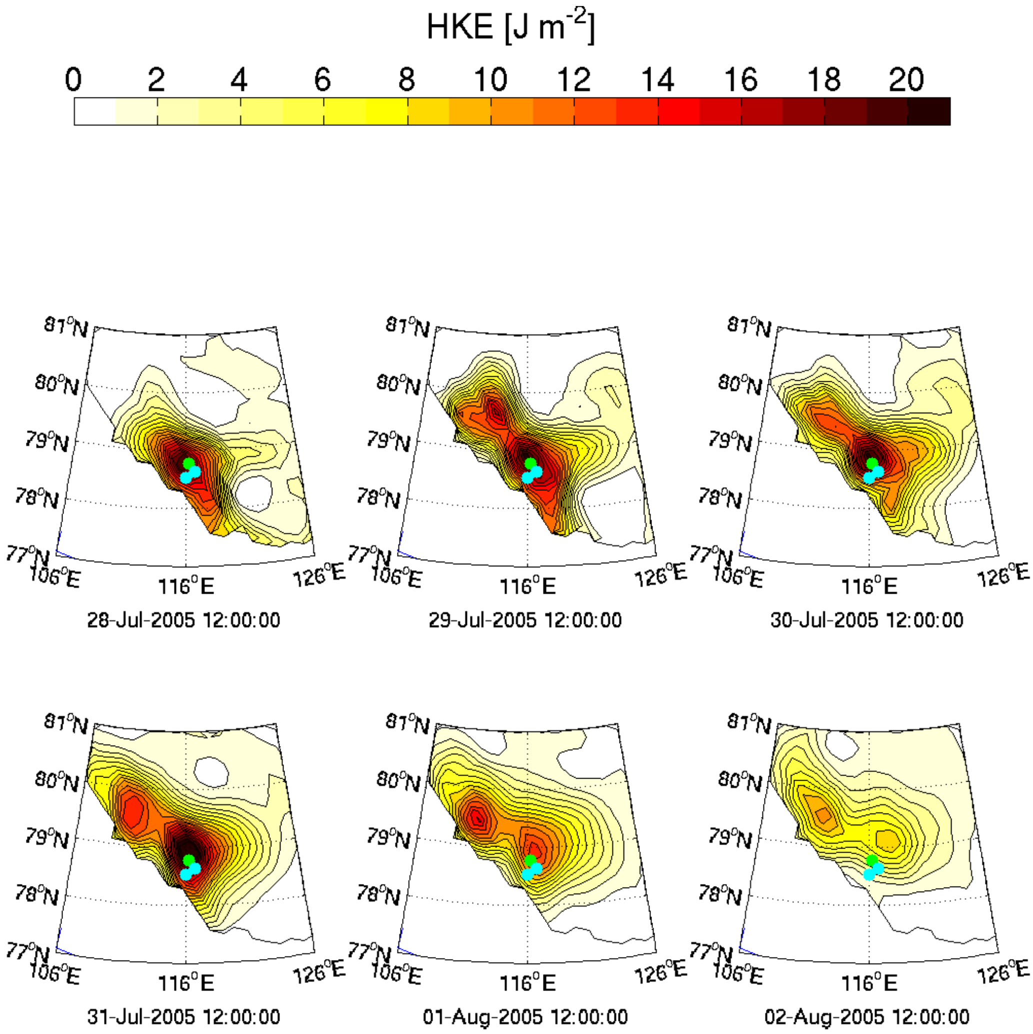

Figure 5.21: Case 4: HKE at the depth of the sub mixed layer energy maximum. Location of case 4 is indicated by the green dot. The two blue dots indicate the two points further south, used in figure 5.19.

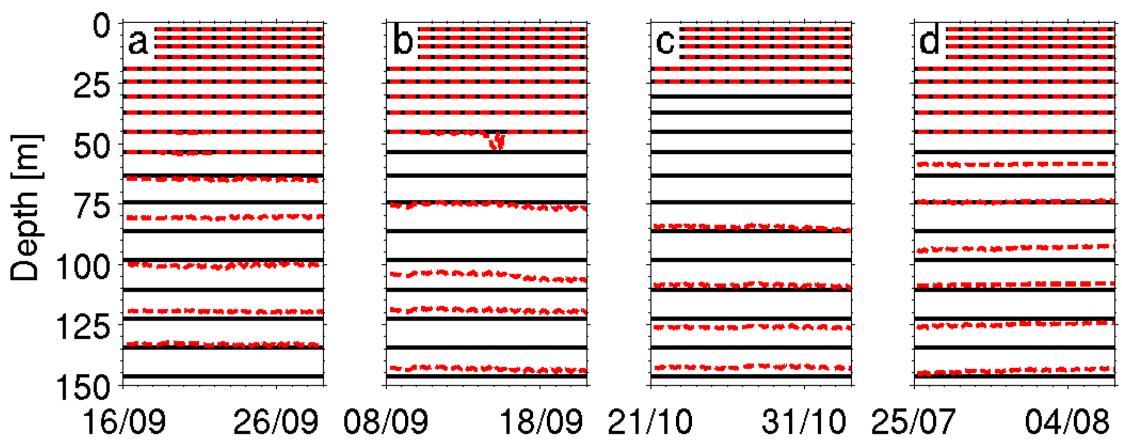

Figure 5.22: Layers for R26 (red dashed line) and for V42 (black solid line) for a) case 1, b) case 2, c) case 3 and d) case 4.

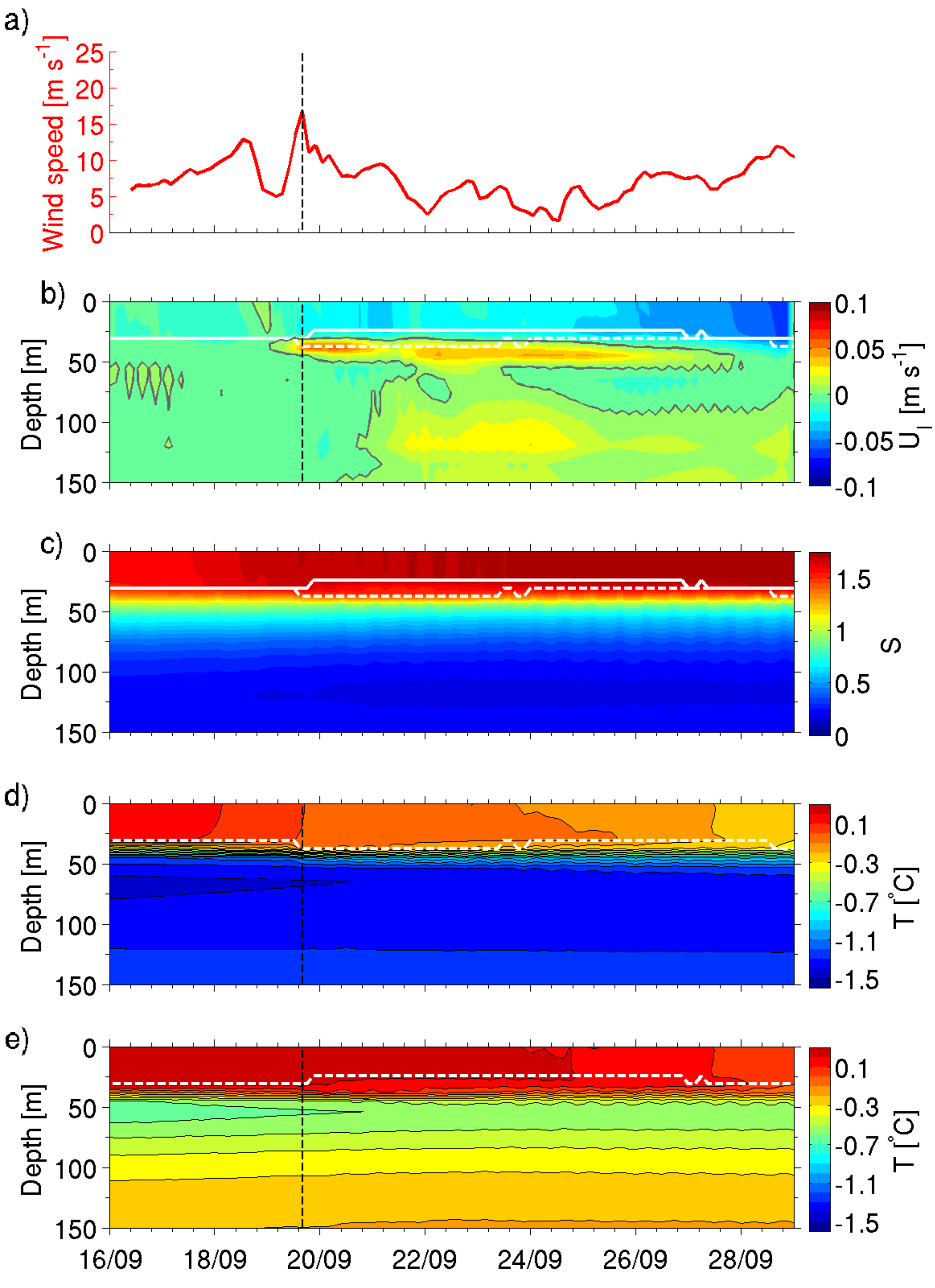

Figure 5.23: Case 1: a) The wind speed. The differences between R26 and V42 are shown in b) and c), showing the near-inertial current speed and salinity, respectively. The difference is calculated as diff=$s_{R26} - s_{V42}$, thus a negative difference means that the fine resolution experiment (V42) has higher values than the coarse resolution experiment (R26). The zero-level in b) is indicated by a thin, grey contour. d) and e) show the temperature for R26 and V42, respectively. The white dashed line indicates the mixed layer depth for R26, the white solid line indicates the mixed layer depth for V42. The vertical dashed line indicates the time of the maximum wind speed.

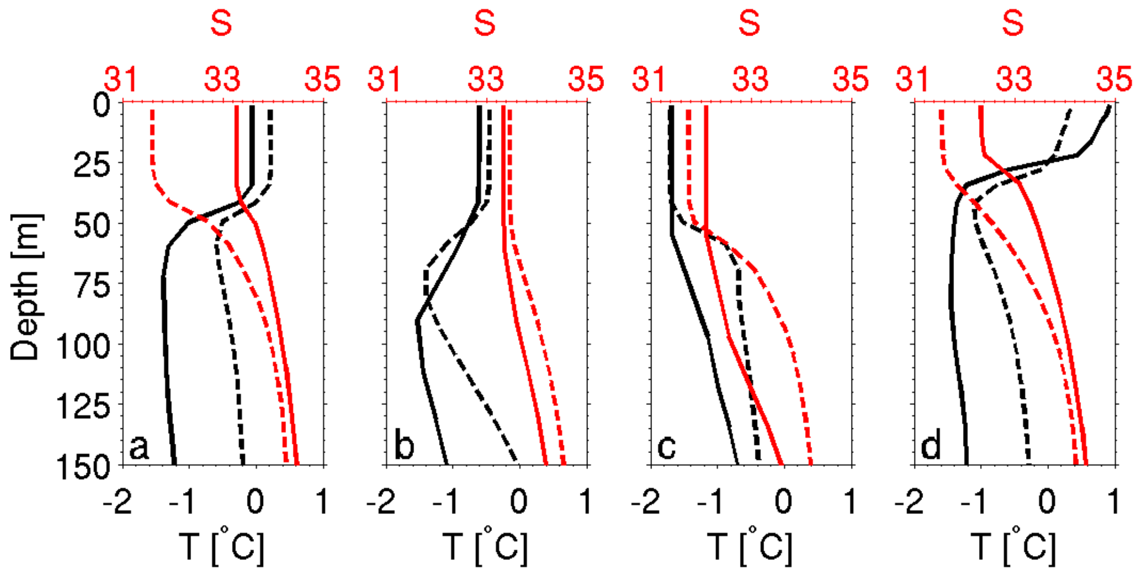

Figure 5.24: Temperature (black) and salinity (red) for R26 (solid) and for V42 (dashed) for the four cases: a) case 1, b) case 2, c) case 3 and d) case 4. Profiles are averaged over the respective period each case is shown for.

are seen in figures 5.23-5.30. The wind field for R26 and V42 is the same, since the horizontal resolution has not changed. Thus, the incoming energy is the same for the two experiments.

5.2.1 Case 1

Case 1 run in V42 is seen in figure 5.23. Figure 5.23(a) shows the wind and 5.23(b) the difference in near-inertial current speed between R26 and V42. It shows that the mixed layer near-inertial speed is greater in V42 than in R26 and that the mixed layer depth differs between the two experiments, see figure 5.23(b)-(e). In R26 the mixed layer deepens from 31 m before the storm to 38 m during. In V42 the mixed layer shoals from 31 m before the storm to 25 m during. This means that the same amount of incoming energy has to be distributed over a larger depth in R26 than in V42. Hence, the energy in the mixed layer is smaller in R26 than in V42, but greater below.

The salinity, figure 5.23(c), is higher down to 150 m in R26 than in V42. In the surface mixed layer, the difference increases with time, becoming as high as 1.70 psu.

Figures 5.23(d)-(e) show the temperature for R26 and V42, respectively. The temperature in V42 is higher than in R26. The mixed layer temperature in V42 decreases from 0.30°C at the beginning to 0.00°C at the end, i.e. it does not decrease below 0.00°C. In R26 the mixed layer temperature decreases from 0.16°C at the beginning to -0.30°C at the end of the simulation. The cold minimum layer is -0.65°C in V42 and -1.42°C in R26, thus 0.77°C colder in R26 compared to V42.

The temperature and salinity are higher in V42 than in R26. The mixed layer is shallower and thus the energy is distributed differently. Less energy propagates out of the mixed layer and downwards in V42 than in R26. This indicates a stronger stratification in V42. Figures 5.23 and 5.26 suggest that the stratification is stronger in V42 than in R26. By examining the thermo- and halocline in figure 5.24(a) it is clear that the halocline is much stronger in V42 than in R26. The thermo- and halocline shown in this figure is the average over the time period spanning from the 16th to the 29th of September. The halocline is stronger since the mixed layer salinity is 1-2 psu lower in V42 than in R26 and below 100 the salinity is comparable in the

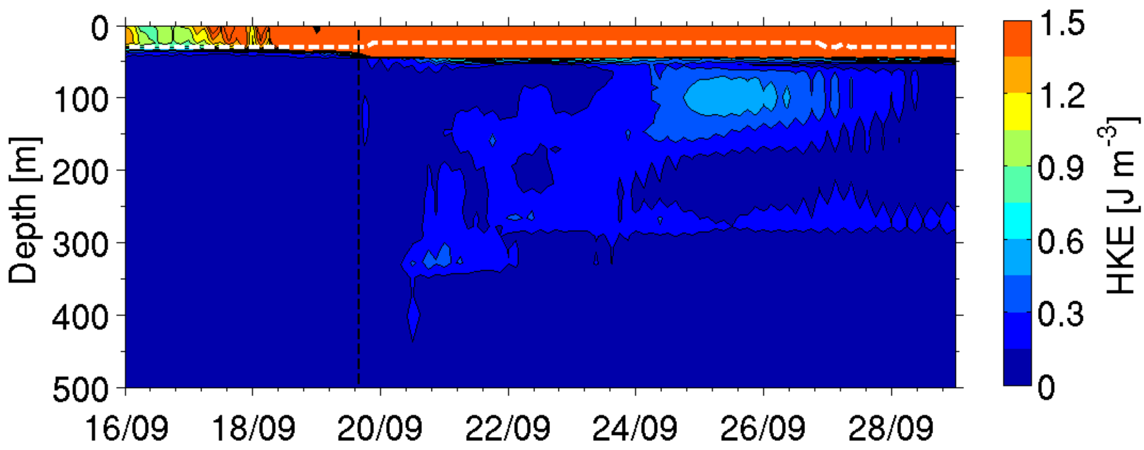

Figure 5.25: Case 1: HKE with depth for V42 (contour interval 0.15 J m^{-3}). The vertical black line indicates the time of the maximum wind speed. The white dashed line indicate the mixed layer depth. HKE is enhanced for HKE > 0.15 J m^{-3}.

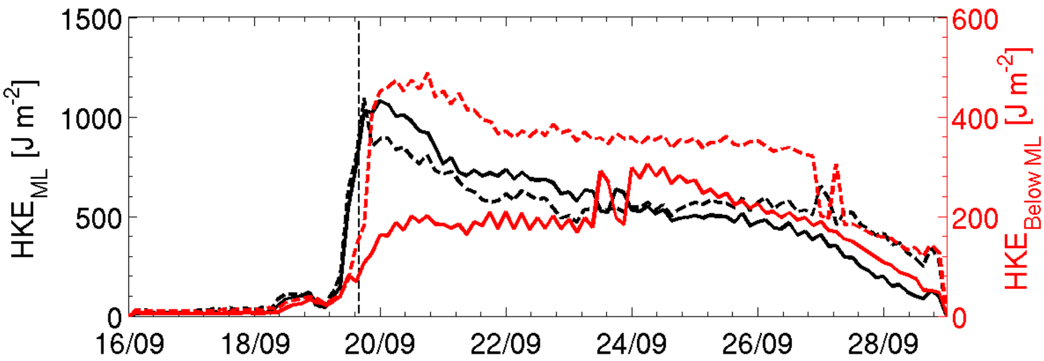

Figure 5.26: Case 1: E_{ML} (black) and $E_{Below\ ML}$ (red) for R26 (solid) and V42 (dashed).

two experiments. As for the thermocline it is the opposite, here it is strongest in R26, but since the halocline is the major contributor to the density distribution in the Arctic, the stratification is strongest in V42.

The depth to which the near-inertial waves in V42 penetrate is estimated by the kinetic energy (HKE), as shown in figure 5.25. At 100 m depth the energy is greater than 0.15 J m^{-3}. Comparing this to R26 (figure 5.3) shows that less energy propagates out of the mixed layer in V42 than in R26. There is an enhanced near-inertial signal in V42 down to 350 m, compared to 250 m in R26.

The depth-integrated kinetic energy in the mixed layer and below it is seen in figure 5.26. The maximum E_{ML} are similar in R26 and in V42: 1081 J m^{-2} and 1095 J m^{-2}, respectively. The energy decreases faster in V42 than in R26, causing E_{ML} to be largest in R26 from the time of the storm until the 25th. After this, the mixed layer energy is highest in V42. The energy below the mixed layer, $E_{Below\ ML}$, is much higher in V42 than in R26: 488 J m^{-2} and 305 J m^{-2}, respectively. However, figure 5.23(b) shows the opposite, here the energy below 31 m is higher in R26. The high value of $E_{Below\ ML}$ in V42 could be due to the fact that the mixed layer shoals in V42, whereas it deepens in R26. From figure 5.23(b) it is seen that in the 7 m below the mixed layer depth in V42, the near-inertial velocity is greater in V42 than in R26. Since the energy is proportional to the velocity squared, the difference in velocity between R26 and V42 is larger for high velocities than for low velocities.

5.2.2 Case 2

Figure 5.27 compares R26 to V42 for case 2. The mixed layer depth for R26 and V42 is seen in figures 5.27(b)-(e). The mixed layer base in R26 is at a depth of 38 m before the storm. After the storm it deepens to 46 m where it more or less remains for the rest of the shown period. In V42 the mixed layer depth is 31 m for most of the first day. On the 9th it deepens to 38 m where it remains until the storm has peaked, after which it deepens further to 46 m. The mixed layer deepens to 46 m a few hours before in R26 than in V42. In R26 the mixed layer depth does not change significantly for the rest of the period, but in V42 it deepens even further to 54 m on the 16th, as the second strong wind peaks.

Figure 5.27(b) shows the difference in near-inertial speed between R26 and V42, with positive values for greater values in R26. It is seen that the near-inertial speed in V42 is strongest above ∼54 m, especially after the second strong wind on the 16th. Actually, the storm on the 11th and the second strong wind on the 16th in V42 generate similar near-inertial speeds of 0.20 m s^{-1}. In R26 the near-inertial speeds were 0.20 and 0.15 m s^{-1}. Below ∼54 m, the near-inertial speed is greatest in R26.

The difference in salinity between R26 and V42 is shown in figure 5.27(c). The entire water column down to 150 m is more saline in V42 than in R26. The salinity from 75 to 125 m is 0.50 psu higher in V42 than in R26 and the difference in the mixed layer becomes stronger with time.

Figures 5.27(d) and (e) show the temperature for R26 and V42, respectively. The mixed layer is warmer in V42 than in R26 by approximately 0.10-0.20°C. The cold minimum layer with temperature of -1.51°C is close to the minimum temperature in R26, but the layer is thinner and closer to the surface in V42, lying at 50-60 m in V42 and at 60-80 m in R26. The stratification is stronger in V42, as the change in temperature is greater and occurs over a shallower depth. The most significant feature in V42 is that the strong wind on the 16th deepens the mixed layer and thus the thermocline. The minimum temperature at the end of the simulation, after the storm and the second strong wind on the 16th have occurred, is -1.49°C in R26 and -1.40°C in V42, 0.09°C warmer in V42 than in R26.

The thermocline and halocline are stronger in V42 than in R26, which is clear from figure 5.24(b) showing the average temperature and salinity taken from the 8th to the 21st of September. Here the difference in temperature is clear as well, with V42 being warmer at depth and the cold minimum being shallower in V42.

Figure 5.28 show the HKE with depth for case 2 in V42. In V42 the near-inertial waves penetrate down to 150-160 m, the same as in R26. As opposed to R26, the energy only propagates down below 75 m until the 18th, after the second strong wind has peaked. In R26 the energy propagates down below 75 m on the 15th. This supports what is seen in figure 5.27 that the second strong wind on the 16th generates a relatively strong near-inertial event in V42, compared to R26.

The depth-integrated energy in the mixed layer and below the mixed layer for R26 and V42 is seen in figure 5.29. E_{ML} is higher in V42 for both the storm and for the second strong wind. During the storm it reaches 759 J m^{-2} and during the second strong wind it becomes even higher, reaching 886 J m^{-2}. This is different from R26 where the second event is smaller than the storm. The two energy peaks in V42 higher than in R26. On the 11th the difference is 180 J m^{-2} and on the 16th it is 447 J m^{-2}.

For the energy below the mixed layer ($E_{\mathrm{Below\ ML}}$) there are differences as well. $E_{\mathrm{Below\ ML}}$ is

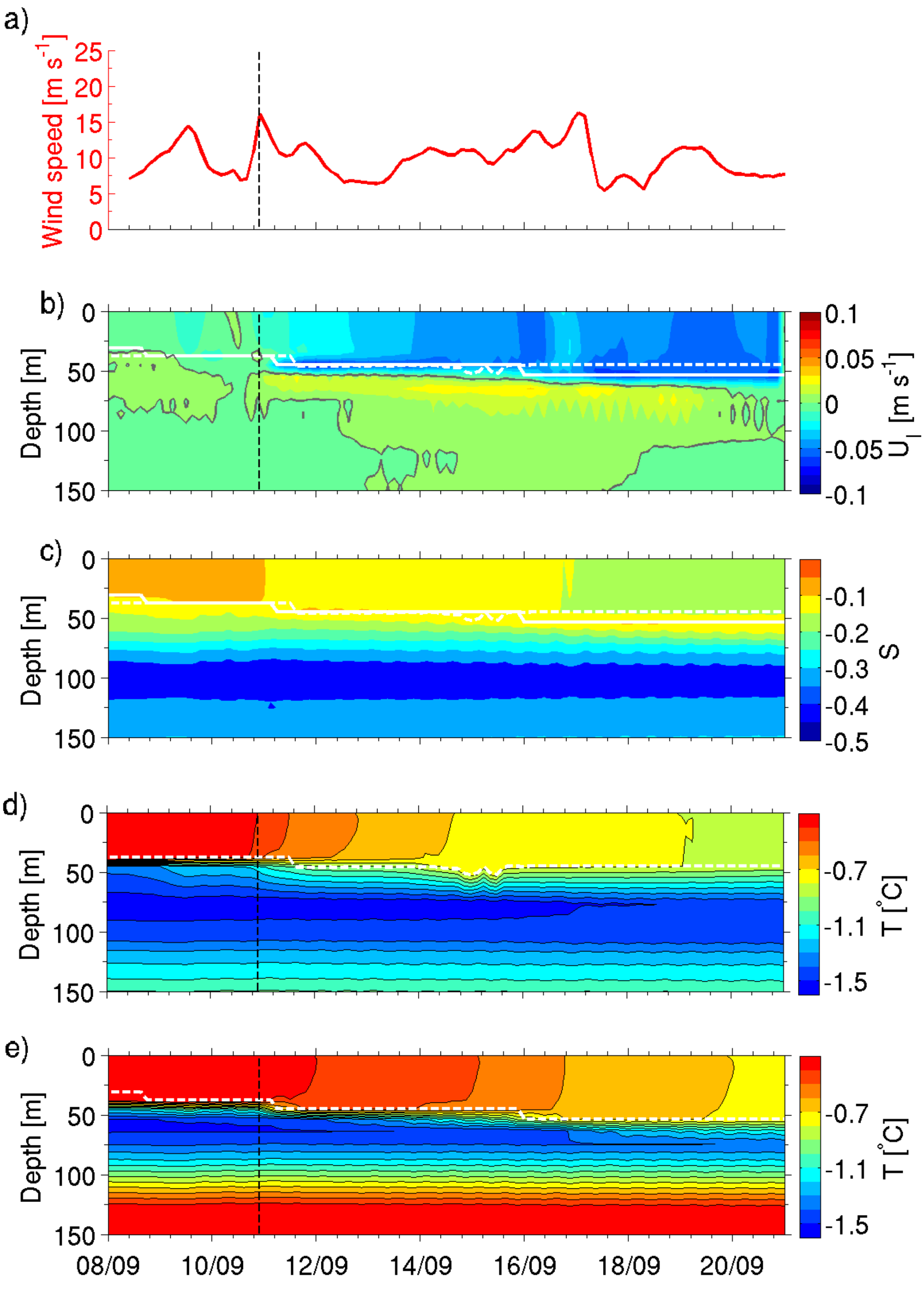

Figure 5.27: Case 2: a) The wind speed. The differences between R26 and V42 are shown in b) and c), showing the near-inertial current speed and salinity, respectively. The difference is calculated as diff=$s_{R26} - s_{V42}$, thus a negative difference means that the fine resolution experiment (V42) has higher values than the coarse resolution experiment (R26). The zero-level in b) is indicated by a thin, gray contour. d) and e) show the temperature for R26 and V42, respectively. The white dashed line indicates the mixed layer depth for the R26, the white solid line indicates the mixed layer depth for V42. The vertical dashed line indicates the time of the maximum wind speed.

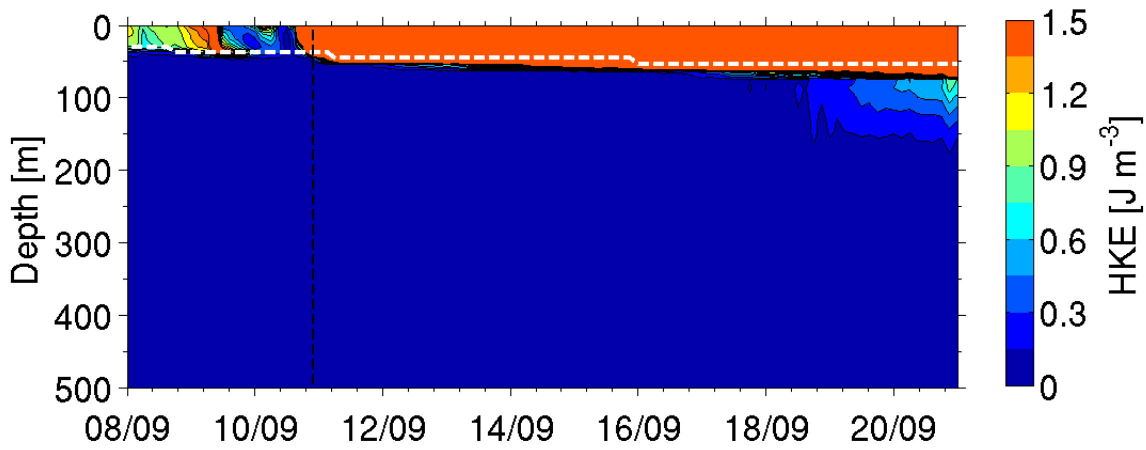

Figure 5.28: Case 2: HKE with depth for V42 (contour interval 0.15 J m^{-3}). The vertical black line indicates the time of the maximum wind speed. The white dashed line indicate the mixed layer depth. HKE is enhanced for HKE > 0.15 J m^{-3}.

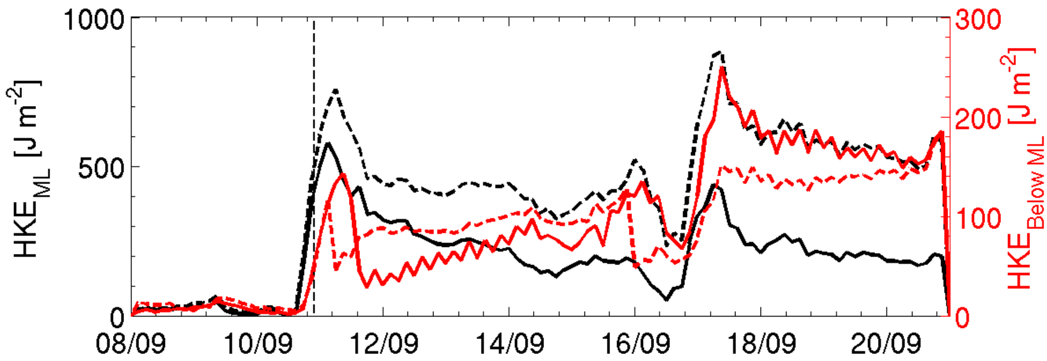

Figure 5.29: Case 2: E_{ML} (black) and $E_{Below\ ML}$ (red) for R26 (solid) and V42 (dashed).

higher for the storm in R26, but it rapidly decreases and become less than in V42. $E_{Below\ ML}$ increases faster in R26 than in V42 and from the 16th the energy is higher in R26 again. This persists throughout the rest of the period. Both R26 and V42 reaches their maxima after the second strong storm, but the energy is 65 J m^{-2} higher in R26 than in V42. This shows that more energy propagates out of the mixed layer in R26 than in V42, hence the stratification is stronger in V42, as was also found from investigating the thermo- and halocline in figure 5.24(b).

5.2.3 Case 3

Comparing R26 and V42 for case 3 reveals some differences, seen in figure 5.30. The mixed layer depth for both R26 and V42 are shown in figures 5.30(b) to (e). In R26 the mixed layer depth is constant with time at 25 m, but in V42 the mixed layer is almost twice as thick, reaching down to 38 m before the storm peaks and deepening to 46 m after.

Figure 5.30(b) shows the difference in near-inertial speed between the two, where positive values indicate that the near-inertial speed is greater in R26 than in V42. Before the storm the near-inertial speed is greatest in V42, except for just before the wind peaks, indicating that the near-inertial speed increases before in R26 than in V42. As the storm peaks, the near-inertial speed in the upper 50 m is stronger in V42 than in R26. Below 50 m it is the opposite, except

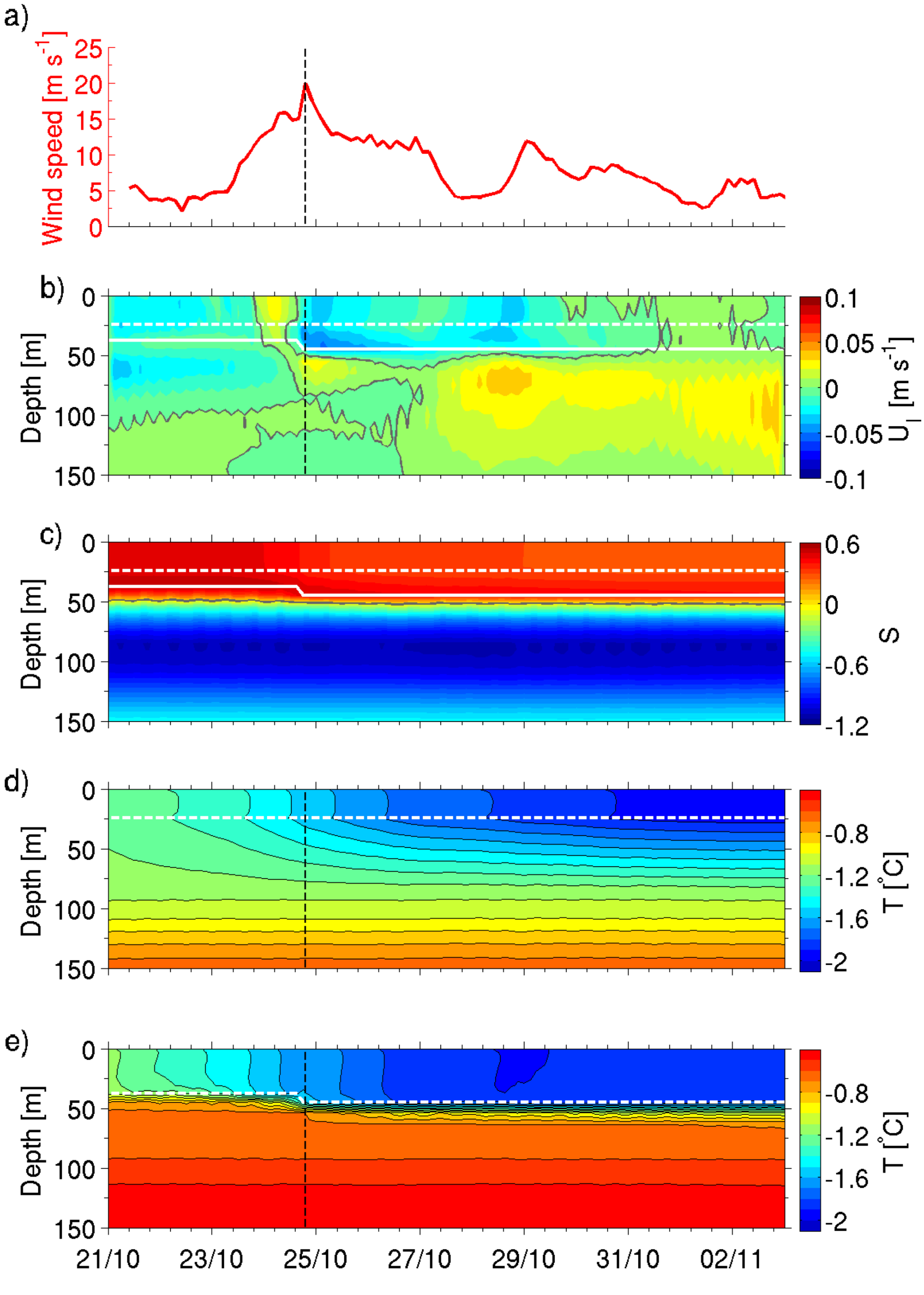

Figure 5.30: Case 3: a) The wind speed. The differences between R26 and V42 are shown in b) and c), showing the near-inertial current speed and salinity, respectively. The difference is calculated as diff=$s_{R26} - s_{V42}$, thus a negative difference means that the fine resolution experiment (V42) has higher values than the coarse resolution experiment (R26). The zero-level in b) and c) are indicated by a thin, gray contour. d) and e) show the temperature for R26 and V42, respectively. The white dashed line indicates the mixed layer depth for the R26, the white solid line indicates the mixed layer depth for V42. The vertical dashed line indicates the time of the maximum wind speed.

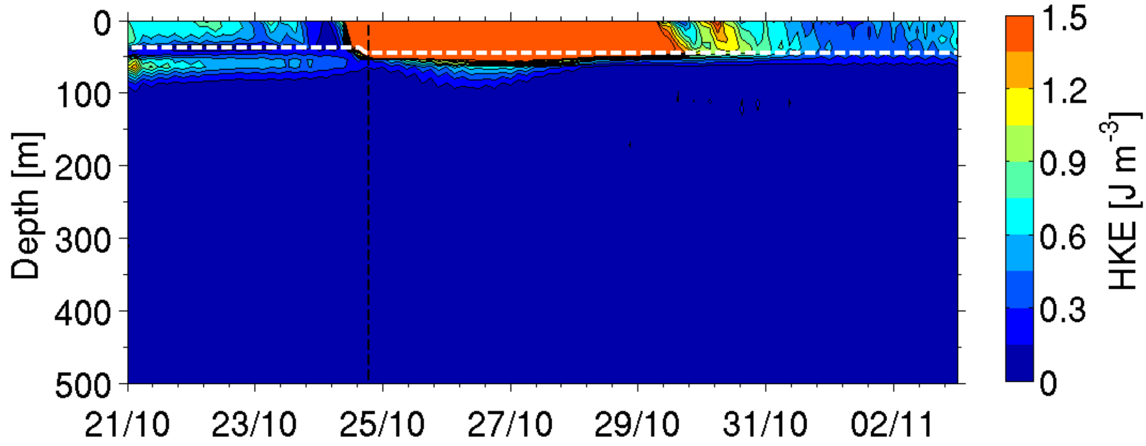

Figure 5.31: Case 3: HKE with depth for V42 (contour interval 0.15 J m^{-3}). The vertical black line indicates the time of the maximum wind speed. The white dashed line indicate the mixed layer depth. HKE is enhanced for HKE > 0.15 J m^{-3}.

for just under the mixed layer in V42. This means that the near-inertial waves generated are stronger in the mixed layer in V42 than in R26 and that they penetrate down to 60 m in V42. The near-inertial waves generated in R26 are distributed over a larger area, down to first 75 m and later down below 150 m. This means that the energy in the mixed layer in R26 must be less than that in V42, as the incoming energy is the same. The near-inertial speed peaks at 0.14 m s^{-1} in R26 and at 0.15 m s^{-1} in V42.

The difference in salinity between R26 and V42 is shown in figure 5.30(c). The water above 50 m is more saline in R26, but as time goes by, the difference decreases. Below 50 m, V42 has the highest salinity. Between 75 and 115 m the salinity is more than 1.50 psu higher in V42 than in R26, indicating a stronger halocline in V42 than in R26.

The temperatures for R26 and V42 are seen in figures 5.30(d) and (e), revealing large differences between the two experiments. First of all, the temperature below ~50 m is higher in V42 than in R26: -0.37°C and -0.63°C, respectively, at 150 m depth. Secondly, the thermocline is stronger in V42 than in R26. Finally, the stratification is stronger in V42 and the mixed layer deepens in V42, whereas it shoals in R26. A possible reason for the difference in mixed layer depth is explained in section 5.1.3.

The average temperature and salinity profiles with depth are taken over the period from the 21st of October to the 3rd of November. The results are seen in figure 5.24. Here, the stronger thermo- and halocline is evident and confirms what are seen in figure 5.30.

The depth to which the near-inertial waves penetrate in V42 is seen in figure 5.31, showing the HKE with depth. Before the storm strikes there are enhanced HKE above the mixed layer and below it, down to 100 m. As the storm peaks, the energy increases above 1.50 J m^{-3} in the mixed layer. Below the mixed layer, the enhanced energy is seen as far down as 100 m, lasting from the 25th to the 28th. In the 5-10 m just below the mixed layer, the energy is enhanced throughout the period. Comparing this to HKE with depth for R26 (figure 5.13) shows that more energy propagates downwards out of the mixed layer in R26. This is possibly due to the much weaker thermo- and halocline and hence the stratification is in R26 than in V42, see figure 5.24.

The difference between R26 and V42 for the energy in the mixed layer and below it is shown in figure 5.32. E_{ML} is much higher in V42 than in R26, peaking at 385 J m^{-2} and 167 J m^{-2}, respectively. This causes the energy below the mixed layer, $E_{Below\ ML}$, to be the opposite; much

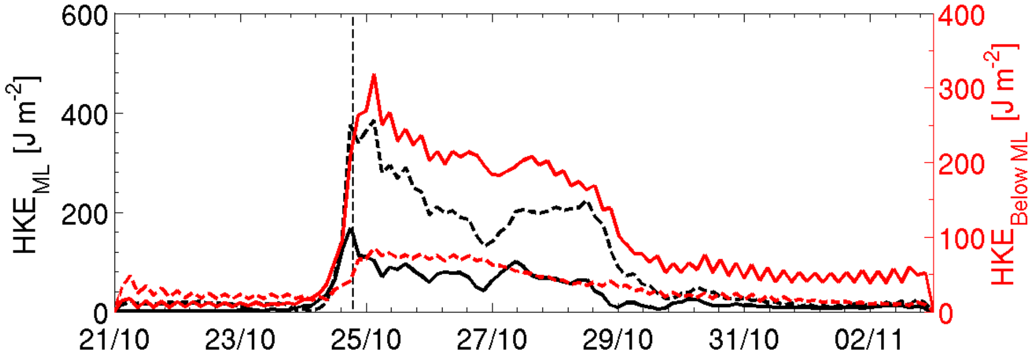

Figure 5.32: Case 3: E_{ML} (black) and $E_{Below\ ML}$ (red) for R26 (solid) and V42 (dashed).

higher in R26 than in V42, peaking at 318 J m^{-2} and 86 J m^{-2}. This indicates that the stratification is much stronger in V42 than in R26, thereby keeping the energy in the mixed layer. This is supported by figures 5.30 and 5.24(c).

5.2.4 Case 4

Figure 5.33 shows the difference between R26 and V42 for case 4. The mixed layer depth in V42 is a few meters deeper than the mixed layer depth in R26. The temporal evolution is more or less the same, except that just before the storm, the mixed layer shoals in R26 but not in V42.

The near-inertial speed shown in figure 5.33(b) is greater in R26 in the mixed layer than in V42, until the 2nd of November. After this, and below the mixed layer, the near-inertial speed is similar in the two experiments.

The salinity is up to 1.20 psu higher between 25 and 50 m in R26 than in V42, figure 5.33(c). Generally, the salinity in R26 is higher than in V42. In the mixed layer the difference increases with time. Below 25 m the difference does not change significantly with time and the difference decreases with depth.

The temperature in R26 and in V42 are shown in figures 5.33(d) and (e). The thermocline is weaker in V42 than in R26, hence the stratification is weaker. Another difference is in the mixed layer depth, which is deeper in V42. In addition to this, the cold minimum layer is thinner in V42 than in R26.

The stratification is more clear from figure 5.24. Here it is seen that the mixed layer is warmer and the temperature below 30-40 m is lower in R26 than in V42, making the thermocline steeper. In addition to this, the halocline is steeper as well, causing the stratification to be strongest in R26.

The penetration depth of the near-inertial waves in V42 is the same as in R26: they penetrate just below the mixed layer, but does not propagate below 40 m which is seen by comparing figure 5.34 with 5.18.

Figure 5.24(d) shows that the stratification is strongest in R26. This, and figure 5.33(d), compares well to E_{ML} being greater in R26 than in V42, meaning that more energy is trapped in the mixed layer in R26 than in V42. The energy below the mixed layer is greater in R26 than in V42, but it should be the opposite, since the same amount of energy is transferred from the wind to the ocean. If more energy is in the mixed layer, less energy should be below it. A possible cause for the greater amount of $E_{Below\ ML}$ in R26 is the change in mixed layer depth. The mixed layer is shallower in R26, but just below the mixed layer the near-inertial velocity is greater in R26 than in V42, see figure 5.33(b).

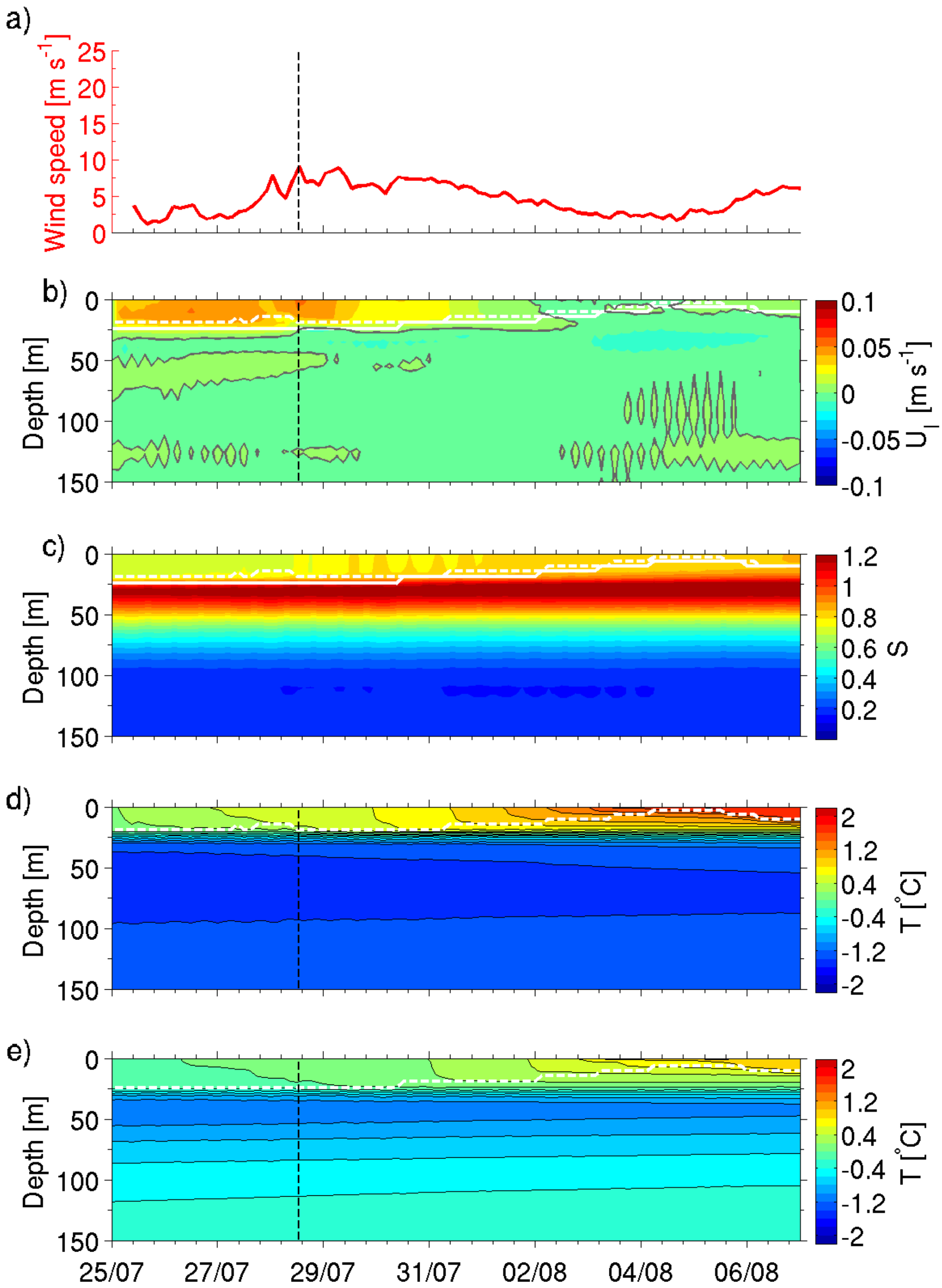

Figure 5.33: Case 4: a) The wind speed. The differences between R26 and V42 are shown in b) and c), showing the near-inertial current speed and salinity, respectively. The difference is calculated as diff=$s_{R26} - s_{V42}$, thus a negative difference means that the fine resolution experiment (V42) has higher values than the coarse resolution experiment (R26). The zero-level in b) is indicated by thin, gray contour. d) and e) show the temperature for R26 and V42, respectively. The white dashed line indicates the mixed layer depth for the R26, the white solid line indicates the mixed layer depth for V42. The vertical dashed line indicates the time of the maximum wind speed.

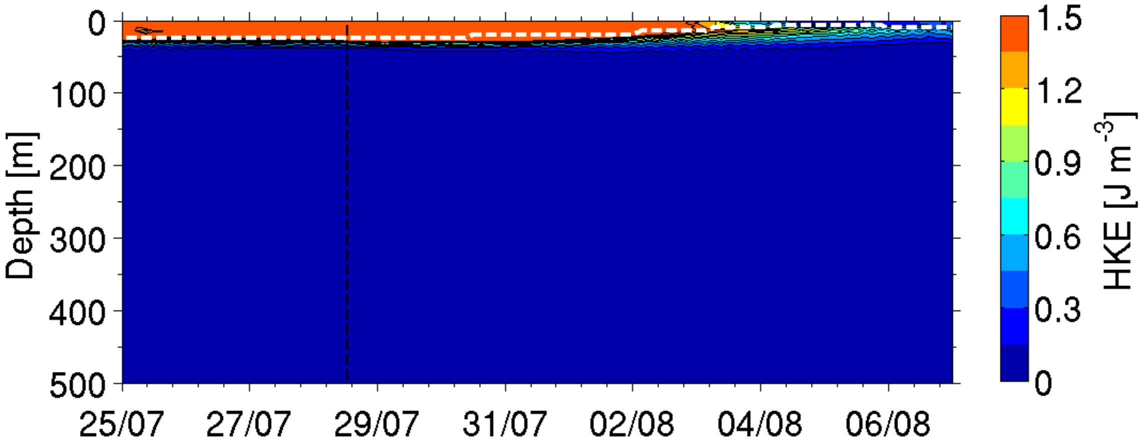

Figure 5.34: Case 4: HKE with depth for V42 (contour interval 0.15 J m^{-3}). The vertical black line indicates the time of the maximum wind speed. The white dashed line indicate the mixed layer depth. HKE is enhanced for HKE > 0.15 J m^{-3}.

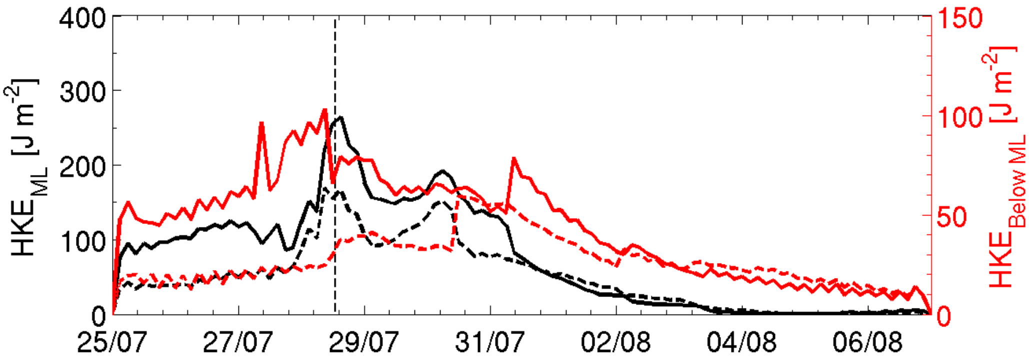

Figure 5.35: Case 4: E_{ML} (black) and $E_{Below\ ML}$ (red) for R26 (solid) and V42 (dashed).

E_{ML} and $E_{Below\ ML}$ for R26 and V42 are shown in figure 5.35. E_{ML} in V42 is less strong than in R26, 169 J m^{-2} and 264 J m^{-2}, respectively. Otherwise, the evolution with time is similar for the two experiments. $E_{Below\ ML}$ for R26 and V42 varies greatly, with R26 being the highest of the two. The oscillations in $E_{Below\ ML}$ in R26 on the 27th and 28th, due to the changes in the mixed layer, are not present in $E_{Below\ ML}$ in V42, since the mixed layer does not vary as much there. Otherwise, $E_{Below\ ML}$ in V42 slowly increases until the 30th, where it jumps to its maximum of 59 J m^{-2}. This is probably a result from the change in mixed layer depth, occurring at the same time. After this, it generally decreases, but then rapidly increases when the mixed layer depth changes.

The results from V42 are seen in table 5.3.

5.2.5 Case 5

In H10, the model is changed much compared to R26, as explained in detail in section 3.5. Due to this, case 5 is not investigated in the same way as cases 1-4. Rather, the general structure of the wind, velocity, temperature and salinity are investigated over one month (November) in 2013, at a location in the Canada Basin.

Case	Max NICS [m s^{-1}]	MLD	Pen. Depth [m]	Depth of Max HKE below ML [m]	Max E_{ML} [J m^{-2}]	Max $E_{Below\ ML}$ [J m^{-2}]
1	0.34	Shoals from 31 to 25 m	350	100	1095	488
2	0.23	Deepens from 38 to 46 m and later to 54 m	160	Just below ML	886	185
3	0.15	Deepens from 38 to 46 m	100	75	385	86
4	0.15	Shoals stepwise from 25 m before and during storm to 6 m and deepens slightly to 10 m again	40	Just below ML	169	59

Table 5.3: Table showing the maximum near-inertial current speed (NICS), the mixed layer depth (MLD), the penetration depth of the near-inertial waves, the depth of the maximum kinetic energy below the mixed layer and the maximum kinetic energy in the mixed layer and below the mixed layer. Results are for the reference experiment V42.

Figure 5.36 shows the layers for case 5 in R26 and H10. The layers are thickest in the upper 150 m in R26, but still quite thick in H10. This difference in the location and thickness of the layer, might contribute to the difference in the observables between R26 and H10, but the change in horizontal resolution and atmospheric forcing are the major contributors.

Using the same method as described in chapter 4, three events in 2013 are found in R26. The largest of these, occurring in November 13th in the Canada Basin, with a maximum near-inertial speed of 0.18 m s^{-1}, does not occur in H10. This can be due to the change in atmospheric forcing, as a small difference can evolve and become larger over time. This is seen in figure 5.37, showing the surface speed and the near-inertial surface speed in November 2013 at 74.1°N 153.7°N. The surface speeds in R26 and in H10 are comparable in magnitude and timing from the 1st to just before the 13th. From the 20th and for the rest of the month, the speed is of comparable magnitude again, but the timing is off. And most importantly, H10 does not capture the strong currents on the 13th to the 17th. The same is seen for the near-inertial speed in figure 5.37(b). From the 1st to the 10th-11th and from the 20th and the rest of the month, the magnitude of the near-inertial speeds in R26 and H10 are similar, but the strong near-inertial currents on the 13th to the 17th are not visible in H10. The maximum near-inertial speed in H10 of 0.08 m s^{-1} occurs on the 11th, a few days before the storm.

The difference in current speed is a consequence of the difference in wind fields between the two experiments. Figure 5.38 shows the wind speed in November 2013 for R26 and H10. The wind speed in the two experiments coincide most of the time, but around the 13th to the 17th the wind in H10 is weaker than in R26, i.e. it does not capture the strong wind generating the near-inertial waves. The currents range between 0.10-0.20 m s^{-1} in both R26 and H10. However, they reach as high as 0.35 m s^{-1} in R26.

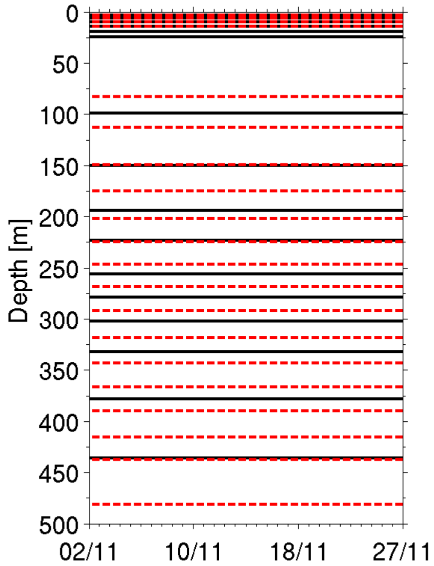

Figure 5.36: Model layers from the 2nd to the 27th of November 2013 at 74.1°N 153.7°W. The black, solid line indicate R26 and the dashed, red line indicate H10.

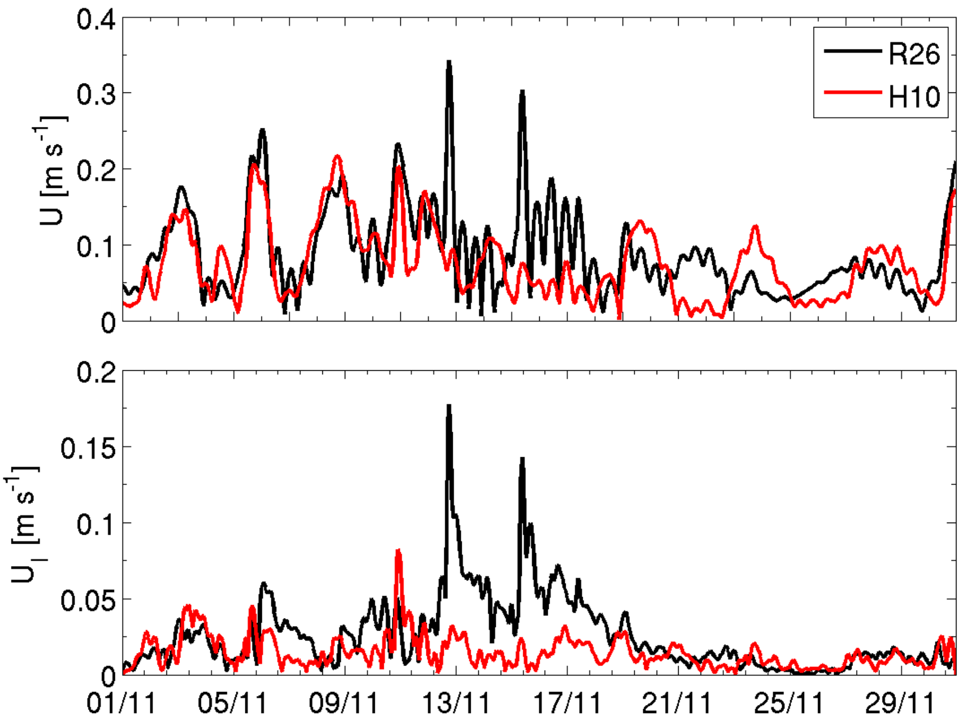

Figure 5.37: Surface current speed (top) and near-inertial surface current speed (bottom) for R26 (black) and H10 (red) i November 2013.

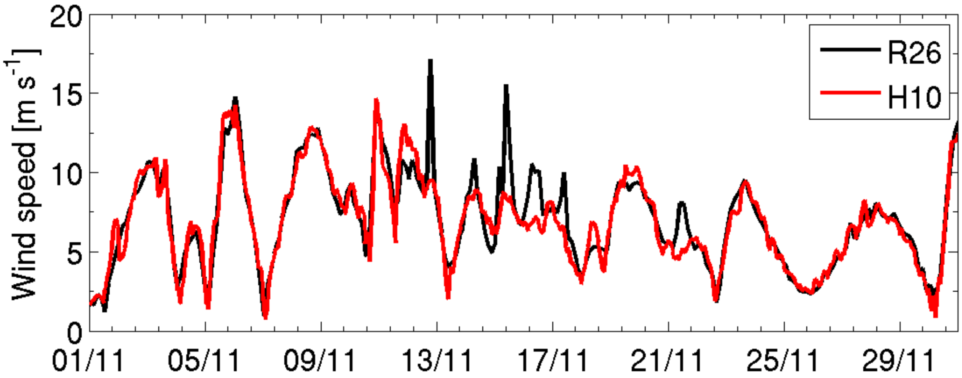

Figure 5.38: Wind speed for R26 (black) and H10 (red) in November 2013.

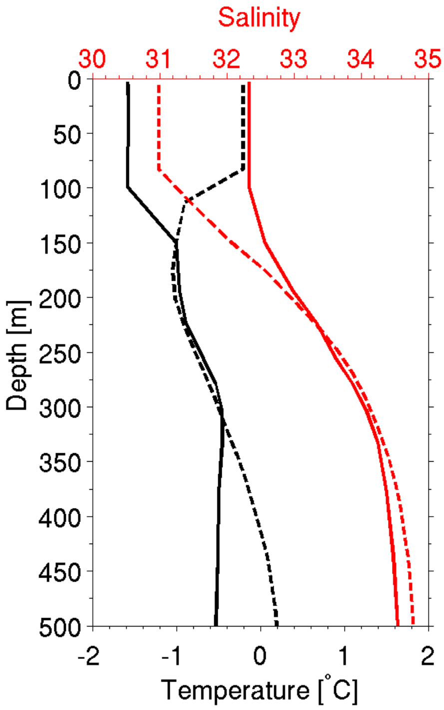

Figure 5.39: Average temperature (black) and salinity (red) for R26 (solid) and H10 (dashed) in November 2013.

The temperature and salinity profiles for R26 and H10 are shown in figure 5.39. The mixed layer depth is at 100 m in R26 and at 83 m in H10. The mixed layer temperature is -1.58°C and -0.21°C in R26 and H10, respectively, 1.37°C lower in R26 than in H10. The temperature in H10 decreases with depth down to the cold minimum at 200 m depth, below which it increases with depth. In R26 the temperature increases with depth continuously. The mixed layer salinity varies greatly between the two as well, with a value of 32.33 psu in R26 and 30.98 psu in H10. Below the mixed layer, both the temperature and salinity become more similar between R26 and H10 and are almost the same in the range 200 and 300 m. Below 300 m, H10 is warmer and the salinity slightly higher, than in R26.

5.2.6 Summary

Case 1

The halocline steepens in V42 compared to R26, hence the stratification is stronger in V42. It is the opposite for the thermocline, but since the density structure is mostly determined by the salinity in the Arctic, the stratification is stronger in V42. This causes more of the energy to be trapped in the mixed layer in V42. Less energy propagates out of the mixed layer in V42, but the enhanced energy is present down to 350 m in both experiments. The mixed layer shoals in V42, as compared to deepens in R26, which causes the energy below the mixed layer to be larger in V42 than in R26, even though more energy is present below 50 m in R26.

Case 2

The stratification is strongest in V42 as both the thermocline and halocline are steeper than in R26. Note that the water below 125 m is actually warmer than the mixed layer waters in V42, making it possible for warm water to be drawn up to the surface. As in case 1, less energy propagates out of the mixed layer in V42, hence there is more energy in the mixed layer. Just below the mixed layer, the near-inertial waves are stronger in V42, but further down they are strongest in R26. Moreover, in this case, there are two strong winds. In R26, only the 'storm' on the 11th of September generates strong near-inertial currents. In V42, both the wind on the 11th and the second strong wind on the 16th generate strong near-inertial events, with the second one being the strongest. Enhanced near-inertial energy is present down to 150-160 m in both experiments.

Case 3

The thermo- and halocline (hence the stratification), are stronger in V42 than in R26. The mixed layer is deeper in V42. As in the previous two cases, the near-inertial waves in V42 are stronger in the mixed layer and weaker below it. Thus, more energy is propagated out of the mixed layer in R26. The energy is above the background level down to 200 m in R26 and to 100 m depth in V42. The deepening of the mixed layer during the storm and the stronger stratification is probably a result of the increased vertical resolution.

Case 4

This case is opposite to the other three cases. The thermocline and halocline are weaker in V42 compared to R26, hence the stratification is weaker. The near-inertial waves are stronger in the mixed layer in R26, both before and after the storm. Below the mixed layer, the near-inertial speed in V42 is slightly stronger. The mixed layer is slightly shallower in V42 than in R26. The near-inertial waves penetrate down to 40 m in both R26 and 42.

Case 5

Increasing the horizontal resolution (and the vertical resolution by 3 layers) results in changes between R26 and H10. First of all, the mixed layer salinity is lower in H10, the temperature is higher and the mixed layer is slightly shallower. The wind speed coincides well in R26 and H10, except from the 13th to the 18th, during the time of the 'storm'. H10 does not capture the strong winds, which in R26 generate near-inertial waves. This difference in the wind field propagates to the current speed and near-inertial current speed, resulting in a relatively strong near-inertial event occurring on the 13th of November in R26 but not in H10.

Overall, the stratification is stronger in V42 than in R26, causing more energy to be trapped in the mixed layer. Therefore, the near-inertial energy in V42 is the strongest in the mixed layer and just below it. The penetration depth is either the same for R26 and V42 (cases 1, 2 and 4) or shallower in V42 (case 3). V42 is generally warmer, especially with depth.

6 Comparing HYCOM to observations

To investigate how well the HYCOM model performs in the Arctic Ocean with respect to near-inertial waves, it is compared to two different sets of observations. This shows how the model performs at two specific events, but it is not a validation of the model as a whole. The first set is from the Barneo ice camp, measurements are taken in April 2007, and the results are described in Fer (2014). The second set is from the Beaufort continental slope. The measurements are taken in 2008/2009 and are described in Martini et al. (2014).
These two sets of observations are compared both to the reference model, R26, and to V42, where the number of vertical layers is increased from 26 to 42.

6.1 Observations from April 2007

Observations is made 24th-30th of April 2007 on the Barneo ice camp and are described in detail in Fer (2009) and Fer (2014). Some of the measurements are taken using a microstructure profiler MSS90L. An Acoustic Doppler Current Profiler (ADCP) and eXpendable Current Profilers (XCPs) are used to measure the current velocity. Measurements are taken from just below the ice and down to 500 m depth. The currents are only measured between the 25th (day 115) and the 29th of April.

The observations are made 10 days after a storm, and therefore only affected by the aftershock of the storm. In this case, the storm generates near-inertial waves which can still be seen propagating at the time of the measurements. The water column consists of a mixed layer (0-38 m) and an upper cold halocline (38-70 m). The entire CHL is located between 38-125 m. The temperature gradient between 70 and 125 m is very weak. The warm Atlantic water lies beneath 180 m. Between 125 and 250 m, the density structure is determined by both the temperature and the salinity, as opposed to only the salinity in the upper 125 m.

The results from Fer (2014) is seen in figure 6.1. Fer (2009) shows that the temperature and salinity do not change significantly during the observational period, there is no mixing across the CHL and only weak mixing in the upper CHL. Mixing only occurs down to ∼80 m, including the upper CHL. This is established further in Fer (2014) which supports that mixing caused by near-inertial waves is present down to 190 m, but only in the mixed layer and upper CHL is it vigorous enough to overcome the stratification. Below 80 m is the stratification too strong for mixing to occur.

Fer (2014) therefore concludes that although the storm generates near-inertial waves, they only causes mixing down to 80 m and thus do not penetrate the halocline.

6.1.1 Wind and current velocity

Figure 6.2 shows the modelled wind, figure 6.3 the zonal (a) and meridional (b) currents with depth, and figure 6.4 the zonal (a) and meridional (b) currents at specific depths for both R26 and V42. Comparing these to the observations from April 2007 shown in figure 6.1, reveals some major differences regarding the currents, temperature and salinity.

The wind speed used in the model (figure 6.2) is close to the observed wind speed (figure 6.1(a)). In the model and observations, the wind speed decreases from 10 m s^{-1} and 7 m s^{-1}, respectively, at day 114 to ∼2 m s^{-1} just before day 117. Afterwards they increase to ∼6 m s^{-1} and decrease to 2 m s^{-1} at the end of the period. The modelled wind is slightly higher in the beginning, but grows increasingly similar to the observations during the period.

The modelled currents do not compare as well with the observations. The observed currents (figure 6.1(e) to (f)) range between -0.20 and 0.20 m s^{-1}, and is strongest in the upper 100 m, with values typically around 0.10-0.20 m s^{-1}. The current in the upper 100 m is primarily southern, changing between an eastern and a western direction. The modelled R26 currents are seen in figure 6.3. The speed typically ranges between 0.02-0.03 m s^{-1}, reaching a maximum of 0.12 m s^{-1} in the western direction and 0.05 m s^{-1} in the southern direction. The flow after day 115 is primarily to the south-southwest. The current strength decrease with time. As the days go by, the current weakens at the surface. This is seen more clearly in figure 6.4, which compares the modelled currents from R26 to the currents from V42. The currents in V42 are generally slightly stronger than in R26. The modelled zonal currents (figure 6.4(a)) reaches a maximum of 0.12 m s^{-1} for R26 and 0.13 m s^{-1} for V42, both in the western direction. The maximum modelled meridional currents for R26 and V42 are both 0.05 m s^{-1} in the southern direction, figure 6.4(b). The currents for both R26 and V42 are almost entirely southwestern all through the water column, compared to the mainly southern flow observed by Fer (2014).

Thus, the modelled current is weaker than the observed currents; up to 0.13 m s^{-1} in the model and up to 0.20 m s^{-1} in the observations. The direction of the modelled current is south-southwest, like the observed current direction. However, the eastern flows are not captured by the model, especially from day 116.5 and on. V42 captures the strongest western currents better than R26, while R26 estimates the strongest southern currents better than V42. Fer (2014) concludes that mixing occurred from the surface down to the upper cold halocline, at a depth of 80 m. Below this, there is an enhanced dissipation, but the turbulence is too small to overcome the stratification. Fer (2014) suggests that this mixing is caused by near-inertial waves generated by a previous storm. Hence, the near-inertial waves penetrate down to, but not through, the cold halocline layer at 80 m.

6.1.2 Near-inertial kinetic energy

The HKE is used to determine the penetration depth of the near-inertial waves generated in the model. The results are shown in figures 6.5(a) and (b) for R26 and V42, respectively. Previously in this study, energy higher than 0.15 J m^{-3} is said to be enhanced. In figure 6.5, does the energy not exceed 0.07 J m^{-3} in R26 or 0.06 J m^{-3} in V42. Therefore, using this criterion reveals that there are no near-inertial waves generated by the wind. However, there are some disturbance at the surface, propagating downwards to around 100 m. As the modelled velocity is approximately 2/3 of the observed velocity, the modelled energy will only be 4/9 of the observed energy. This explains the low energy level. The kinetic energy is shown in Fer (2014) as HKE/ρ_0 with depth (figure not shown here). This energy ranges between $\sim 10^{-4}$ at 200 m depth to $\sim 9 \cdot 10^{-2}$ J kg^{-1} at the surface. By setting $\rho_0 = 1027$ kg m^{-3} this range becomes 0.10 to 90.00 J m^{-3}. The large difference between the surface and 200 m depth is due to near-inertial waves decreasing rapidly with depth, below the mixed layer. The observed energy is much higher than the maximum energy of 0.07 J m^{-3} found in the model.

6.1.3 Temperature and salinity

The observed thermo- and halocline are compared to R26 and V42 in figure 6.6. The observed halocline is similar to the modelled halocline in R26, except that the observed halocline starts at 38 m, whereas the modelled one starts at 80 m. The observed mixed layer salinity is 33 psu and reaches down to 38 m. It consists of three distinct areas: the upper halocline from 38-80 m, the middle halocline from 80-100 m and the lower halocline from 100-230 m. The upper and

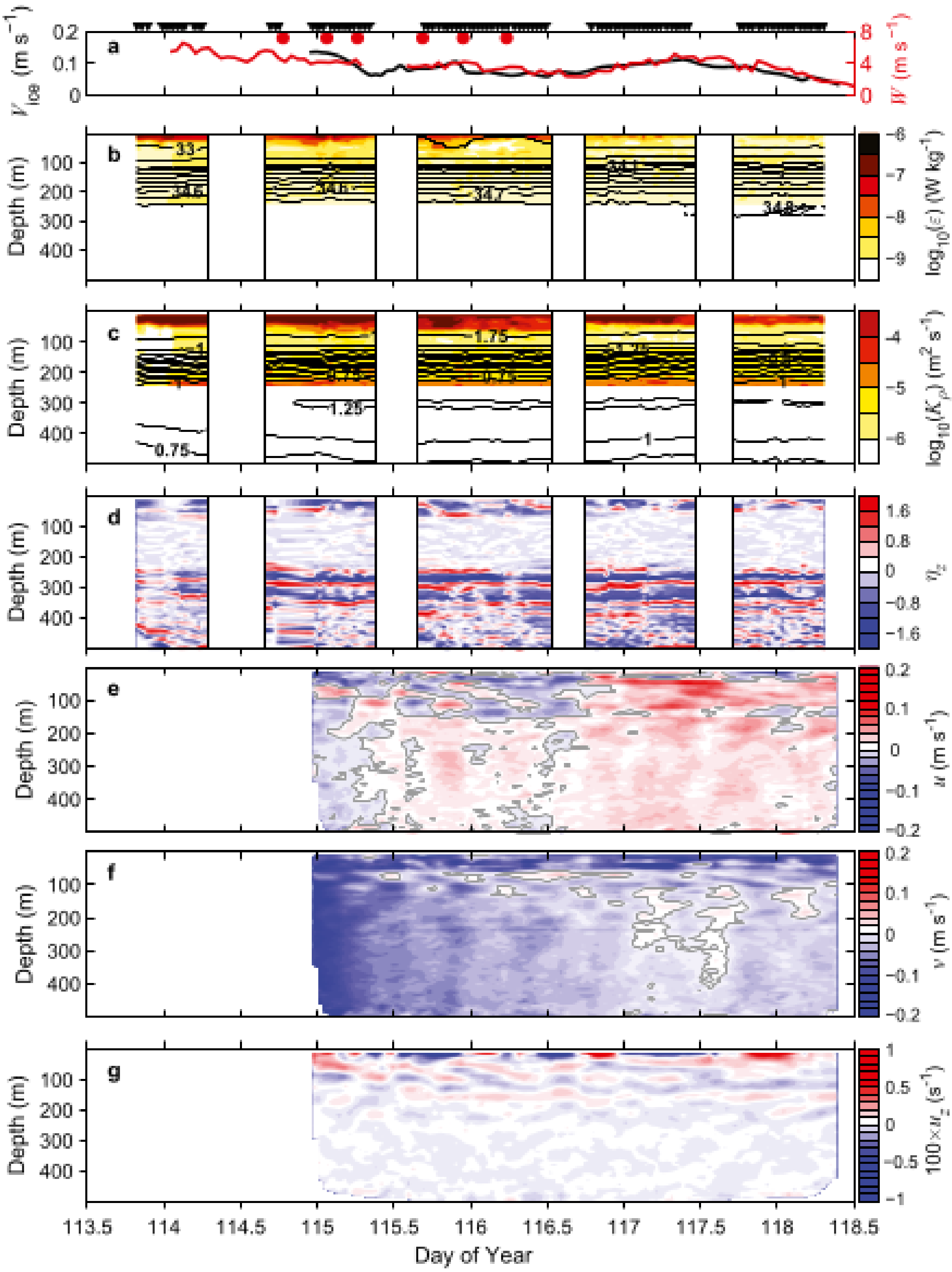

Figure 6.1: Figure from Fer (2014). Only subfigures a), e) and f) are used. a) show the time series of ice speed V_{ice} (black) and wind speed W (red). Triangles (microstructure profiles) and red circles (XCP) indicate which type of measurement was used. e) east and f) north component of the horizontal velocity.

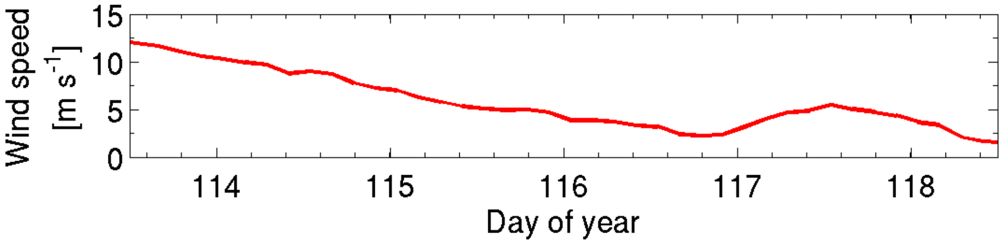

Figure 6.2: Time series of the ERA-Interim modelled wind used in HYCOM.

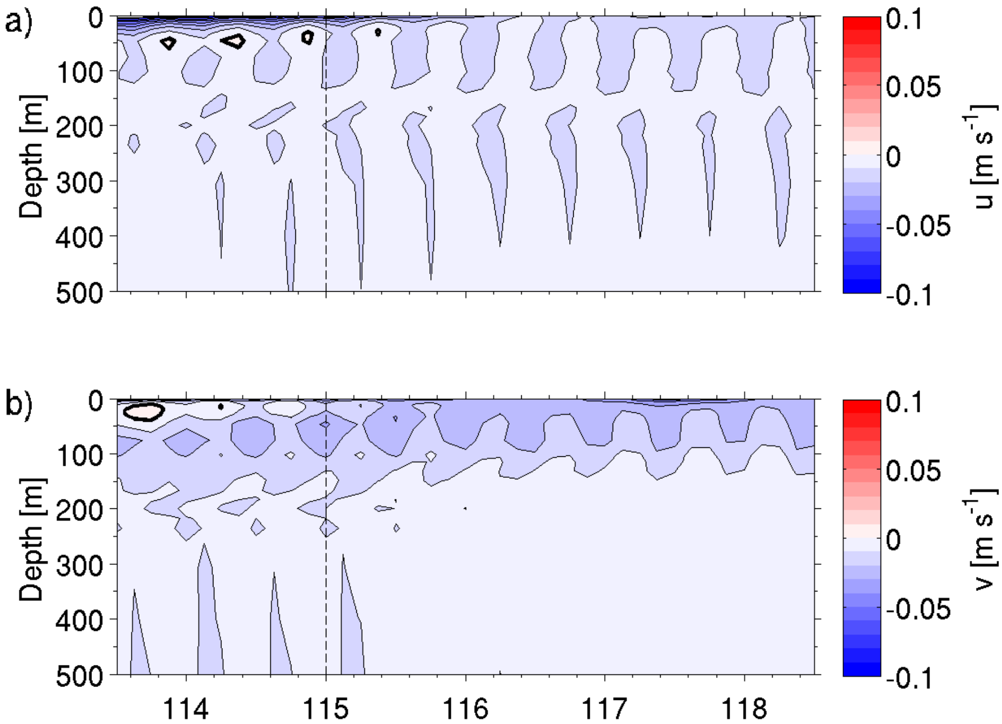

Figure 6.3: Time series of the modelled R26 a) zonal and b) meridional current. The thick contour line indicates $(u, v) = 0$ and the dashed line indicates the time from which there are current observations in figure 6.1.

lower halocline are not as steep as the middle halocline.

These three regions are not seen in the modelled halocline in R26. The upper halocline is not even present in R26, resulting in the cold halocline layer not being present in the model. The modelled mixed layer salinity is 33.30 psu, the same value as the observed salinity at the bottom of the upper halocline. The bend seen in the observations caused by the steeper halocline between 80 and 100 m is not seen in R26 either. Both the observed and the R26 salinity are ∼34.80 psu from 230 m and down.

For V42, the mixed layer salinity is higher than the observed, but below 250 m is the modelled salinity similar to the observed salinity. This means that the halocline in V42 is weaker than both the observed and the R26 modelled halocline. The halocline is too steep just below

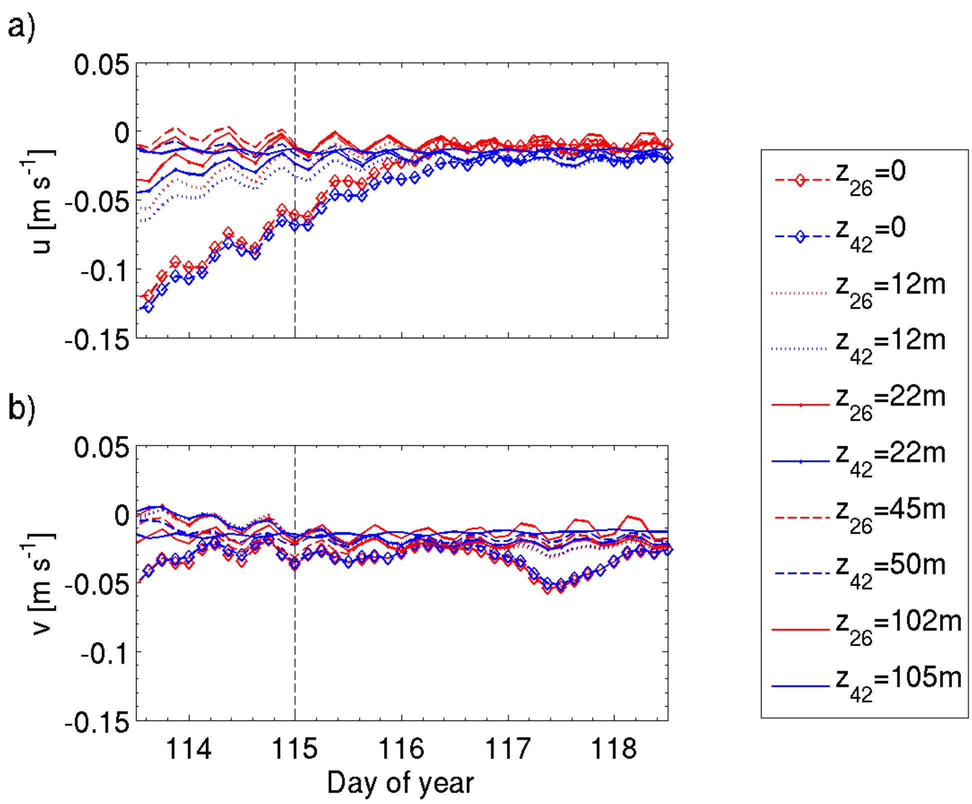

Figure 6.4: Time series of the a) zonal and (b) meridional currents at specific depth (see legend), for both R26 (red) and V42 (blue). The dashed vertical lines indicate day 115, the time from which there are current observations in figure 6.1.

the mixed layer compared to the observations, and it rapidly becomes too weak. Just below 75 m is the halocline stronger in V42 than in R26, but below ~100 m is the halocline stronger in R26.

The observed thermocline begins at 80 m and becomes stronger at 125 m depth. The thermocline continues with this gradient until 230 m, where it weakens again. The observed mixed layer temperature is -1.7°C and the maximum temperature is around 1.0°C at a depth of 250 and 300 m. The modelled mixed layer temperature is -1.80°C and the maximum temperature is 0.02 °C at 400 m in R26. In V42, the maximum temperature are 0.46 °C at 500 m depth. Due to this are the modelled thermoclines much weaker than the observed one. Just below the mixed layer and down to 125 m and 100 m (R26 and V42, respectively), are the thermoclines stronger in the model, but below is the observed thermocline strongest.

This suggests that the observed stratification is stronger than the modelled stratification and that the stratification between 75 and 100 m is stronger in V42 than in R26. Below 100 m is the halocline weaker but the thermocline stronger in R26 than in V42. The modelled thermo- and halocline both begin at 75 m indicating that the cold halocline layer is not present in the model. Further, the warm Atlantic Water below 180 m is too cold or there is not enough of it, compared to the observations. Since the wind used in the model is very close to the observed wind in Fer (2014), the reason for the difference between the modelled and the observed velocity might be in the ocean mixed layer model.

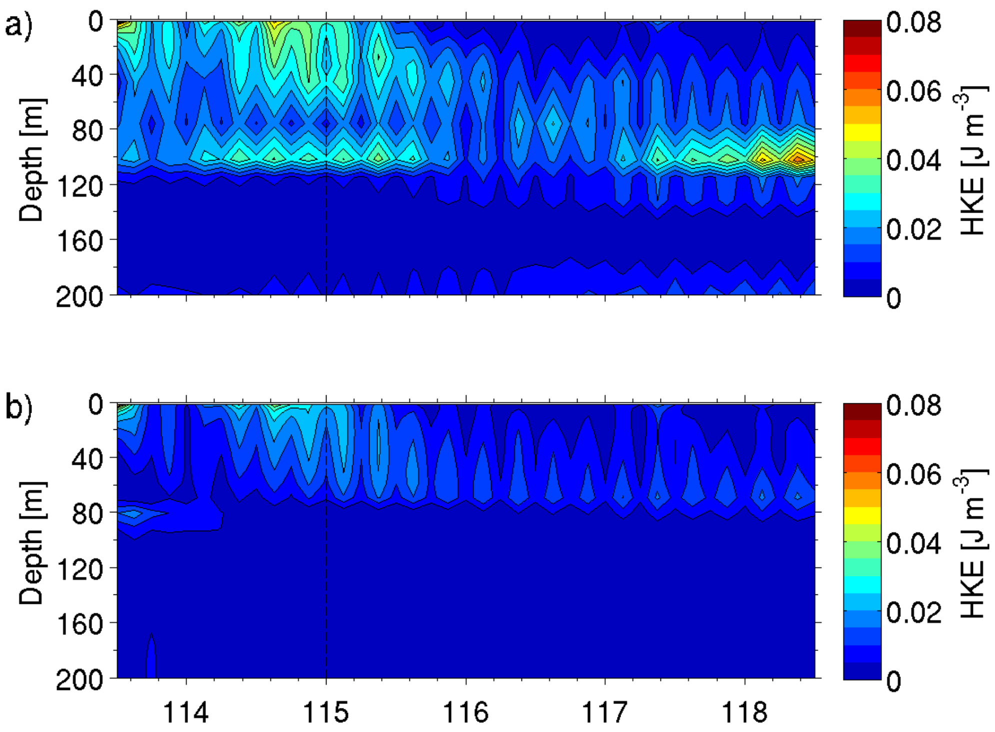

Figure 6.5: Time series of the a) R26 and b) V42 near-inertial kinetic energy. The dashed line indicates the time from which there are current observations in figure 6.1.

6.2 Observations from August 2008 to August 2009

The other set of observations were made in 2008 and 2009 by 6 moorings on the Beaufort continental slope. They are described in detail in Martini et al. (2014). Here, only measurements from one of the moorings are shown: I3 located at 71.37°N 152.05°W on the Beaufort continental slope at the 1886-m isobath, see figure 6.7. At I3 both an upward-looking ADCP and a McLane Mooring Profiler (MMP) were deployed. The ADCP measured horizontal velocities every 8 minutes in 4 m bins, from 7 to 58 m depth. The MMP measured horizontal velocity, pressure, conductivity and temperature from 90 to 580 m in 2 m bins every 3 hours. The potential temperature θ, salinity and ocean current velocities at I3 from August 1st to December 3rd 2008 are shown in figure 6.8.

The potential temperature θ generally increases with depth (figure 6.8(c)). In the upper 200 m θ is approximately -1.50°C and between 200 and 300 there is a sharp thermocline. Below this the water is ~0.50°C. The depth of the thermocline changes slightly from August to December, being deepest in August and end-October and shallowest in September, and most of November. Below approximately 500 m, the water starts to cool again.

The salinity also increases with depth, see figure 6.8(b). The upper 100 m are not recorded, but between 100 m and 300 m there is a sharp salinity gradient, the halocline. The salinity continues to increase with depth, reaching ~34.50 psu at 500-600 m. During the measured period the halocline strengthens (it becomes thinner, but with the same salinity jump across it). In November, the salinity at 600 m reaches approximately 35 psu.

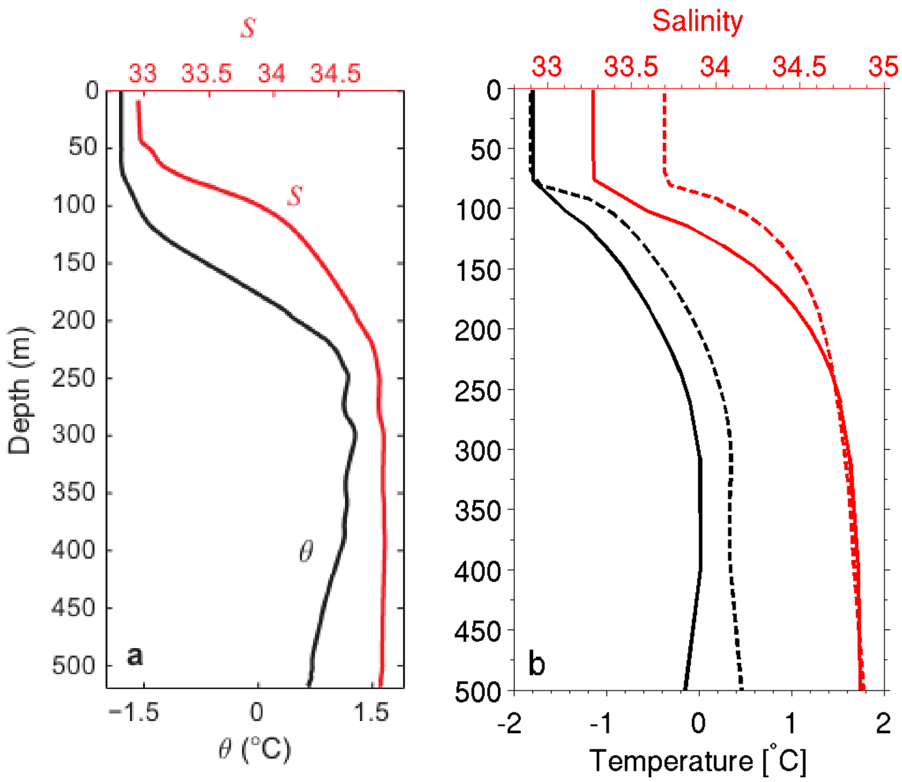

Figure 6.6: Temperature (black) and salinity (red) averaged over the six observational days for a) observations (figure from Fer (2014)), and b) for the model experiments: R26 (solid) and V42 (dashed).

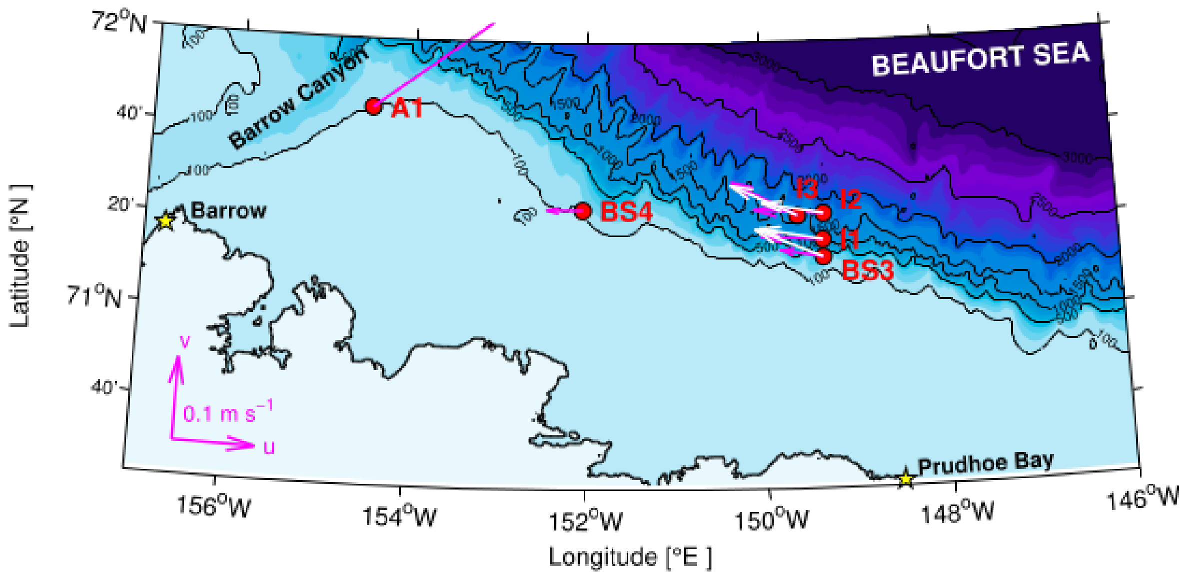

Figure 6.7: Location of moorings in Martini et al. (2014). Figure from Martini et al. (2014).

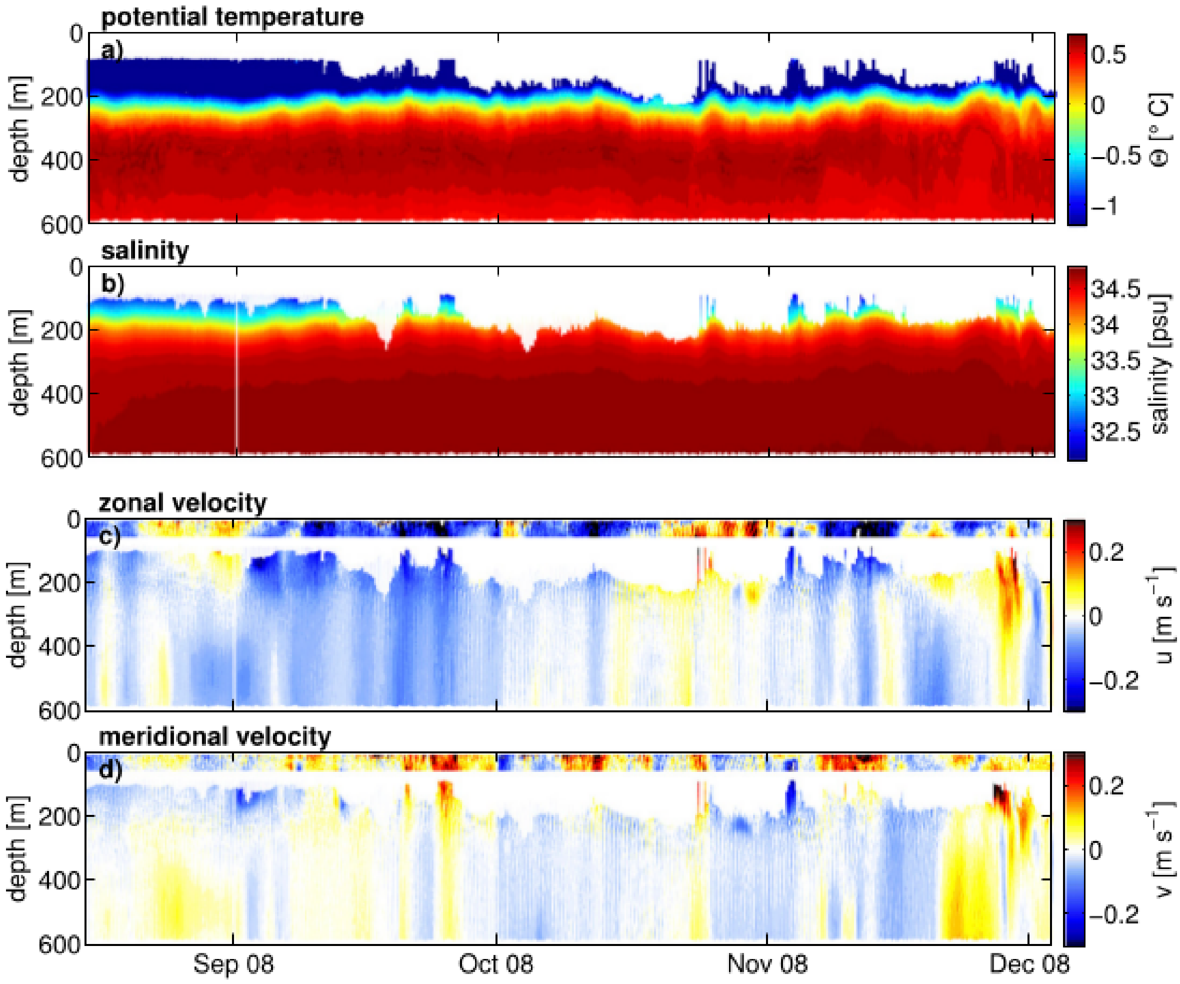

Figure 6.8: Observations from I3 of a) potential temperature, b) salinity, c) zonal velocity and d) meridional velocity. Figure from Martini et al. (2014).

The zonal velocity (figure 6.8(c)) is strongest (the speed generally ranges between 0.20-0.50 m s^{-1}) and nearly uniform in the upper 200 m. An exception to this is in end-November/start-December. Here there are strongly enhanced current velocities from the surface down to almost 400 m. Down to 600 m depth is the zonal velocity still $\sim$0.10 m s^{-1}.

The same is seen for the meridional velocity, shown in figure 6.8(d). In addition to this, there are enhanced meridional velocities in the end of November between 400 and 600 m. The flow is primarily northwestern with periods of strong, north- and southeastern flows.

To compare the observations from Martini et al. (2014) to the model used in this study, a grid point is chosen 45.3 km northeast of I3. The reason for this is that the water depth at this point is 1829 m, whereas at the grid point closest to I3 (only 8 km away) the water depth is only 168 m. The observed water depth at I3 is 1886 m. A possible cause for the water depth close to the location of I3 not being close to the observed water depth, is that the observations are measured on the Beaufort continental slope, i.e. on a steep gradient. The model output at this location for R26 and V42 is seen in figures 6.9 and 6.10, respectively.

6.2.1 Temperature, salinity and velocity for R26

The R26 temperature in figure 6.9(a) shows a very stratified region in the upper 25-30 m, below which a cold layer lies from 30-300 m. The stratification in the surface layer strengthens from August to September, after which it starts to weaken, causing the thermocline to be shallow and strong, and the mixed layer to be very shallow ($\sim$10 m). In October the stratification weakens so much that the cold water from beneath 30 m can mix into the surface layer. The observed strong thermocline between 200 m and 300 m depth, going from $\sim$-1.0 to 0.5° is not as strong in the model. Here the temperature changes from around -1.0° at 180 m to 0.0° at 320 m. Below 350-400 m the temperature is $\sim$0.2°C, close to the observed temperature. Overall, the temperature in the upper 200 m, neglecting the mixed layer, is $\sim$0.5 °C warmer than the observations.

The modelled salinity is almost constant with time, as shown in figure 6.9(b). The halocline lies from 50 to 300 m, a little broader than in the observations, but the salinity jump is about the same from around 32.50 psu at 50 m to 34.50 psu at 300 m. Thus, the salinity changes the same over a broader region, making the halocline slightly weaker in the model. From this it is seen that the observed stratification is stronger than the stratification modelled by R26.

The zonal and meridional current velocities are shown in figures 6.9(c) and (d), respectively. The modelled zonal current velocity has a maximum of 0.31 m s^{-1} and the meridional a maximum of 0.27 m s^{-1}. This is in the low end of the observed velocity range of 0.20-0.50 m s^{-1}. The modelled zonal velocity is primarily northwestern, the same as in the observations. In the observations of the zonal current, there are three distinct strong eastward flows: mid-August to start-September, mid-October to start-November and end-November to start-December. In R26, all of these events have western flows, although the one in mid-October to start-November has a very weak western flow. The observed event around the beginning of December has strong velocities down to 400 m. In R26, the zonal velocity below 200-250 m is only around 0.05 m s^{-1}, and does not reach 0.20 m s^{-1}, as in the observations.

The observed meridional current direction changes between north and south, which is not captured well in the model. The modelled meridional velocity is weakly northward throughout the whole period, except around mid- to end-October.

The ocean surface velocities in the observations are most of the time to the northwest, which is also the case in the models, but during the periods where the observed currents change to a more southeastern direction, the modelled currents only very weakly predicts this. The magnitudes of the modelled currents are smaller compared to the observed currents.

6.2.2 Temperature, salinity and velocity for V42

Similar figures for V42 are shown in figure 6.10. The main temperature structure is the same as for R26, but the strong thermocline at the surface stretches down to 50 m, compared to 30 m in R26, and is present from August to start November. The observed strong thermocline from 200 to 300 m depth is weaker in V42. The temperature changes from around -0.5°C at 200m to 0.0°C at 300 m. In most of September-December, the temperature changes with depth are even smaller, due to the mixed layer being warmer than -0.50°C. Hence, the thermocline is weaker in V42 than in both R26 and the observations.

The surface salinity in V42 is about 0.50 psu saltier than in R26, figure 6.10(b). The halocline is between 110 and 300 m, but since the difference between the mixed layer salinity and the salinity at depth is smaller in V42 than in R26, the halocline stronger is in R26 than in V42.

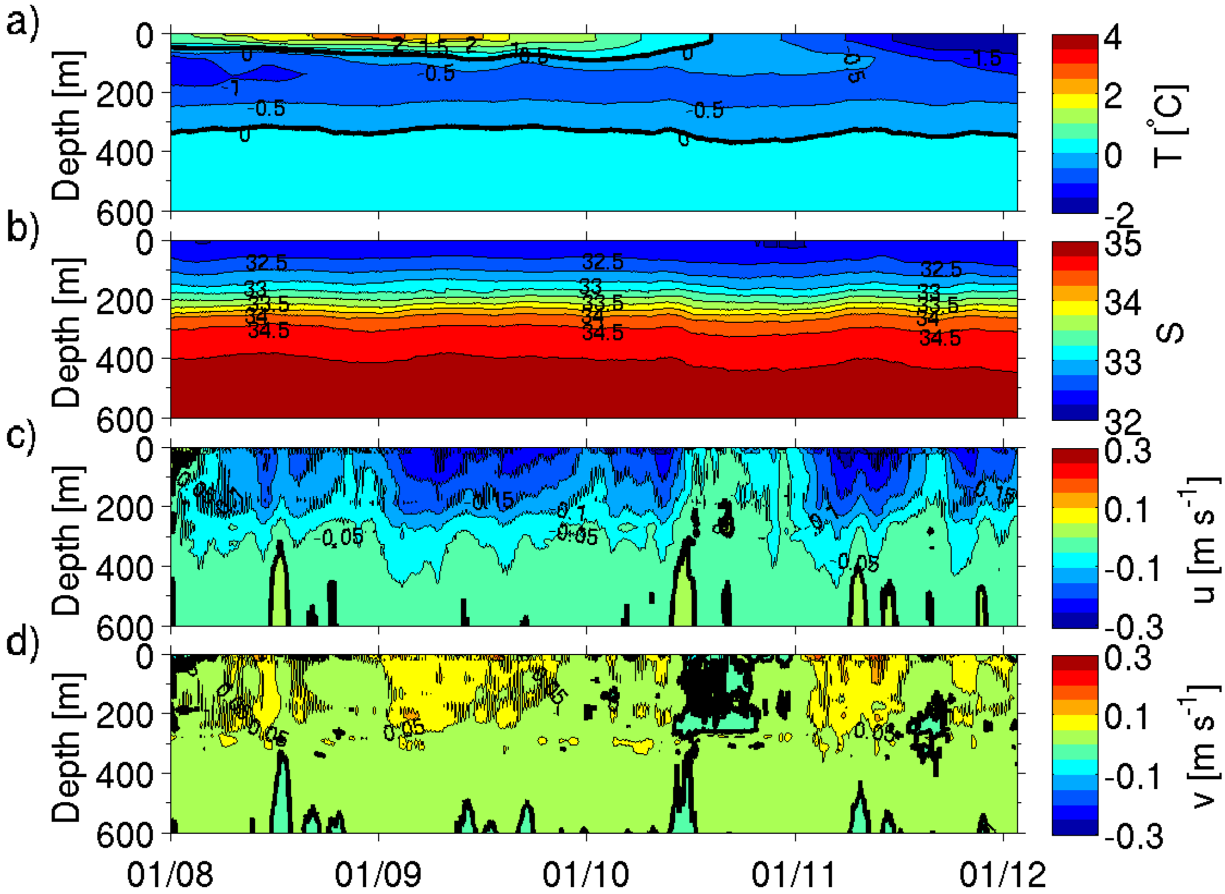

Figure 6.9: Time series from August 1st 2008 to December 3rd 2008 of (a) temperature (colours and contours in 0.50°C intervals, $T = 0$°C indicated by thick contour), (b) salinity (colours and contours in 0.25 psu intervals, $S = 0$ indicated by thick contour) and (c) zonal and (d) meridional current velocity (colours and contours in 0.10 m s^{-1} intervals, $(u, v) = 0$ indicated by thick contour), as estimated by R26.

This results in the salinity in R26 being closest to the observations, compared to V42. From this it can be concluded that the stratification is stronger in the observations in both R26 and V42. R26 comes closest to the observations.

The zonal current velocity (figure 6.10(c)), is still primarily westward (maximum zonal velocity of -0.22 m s^{-1}), but overall it is weaker than in R26. The observed strong eastward events are better captured in V42 than in R26, especially the events in mid-October and November/December. The meridional velocity (figure 6.10(d)) is still primarily northward, but the flow is more often southward than in R26. Especially around mid-to-end November there is a southeastern flow that is a weak northwestern flow in R26. This flow is very clearly seen in the observations. The maximum meridional velocity in V42 is 0.22 m s^{-1}.

To sum up, the temperature in R26 increases with time. Above 300-350 m, the water temperature is not positive, compared to 250 m in the observations. The simulated halocline lies a bit deeper than the observed halocline, but otherwise it is much like the observed. The direction of the currents in R26 is mostly northwestern, like the observations, but the periods with southeastern flows are not captured. Only one event in October with southeastern flow is caught and

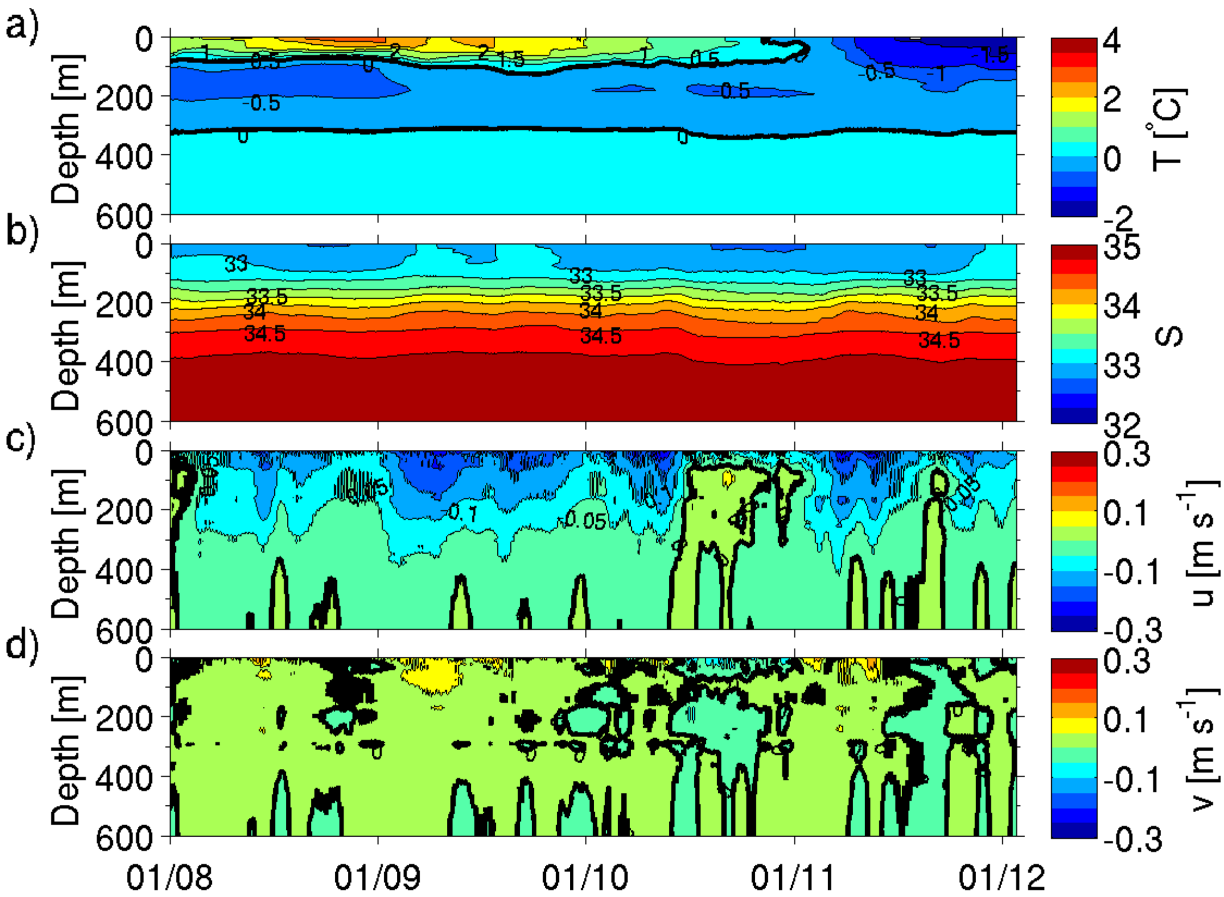

Figure 6.10: Time series from August 1st 2008 to December 3rd 2008 of (a) temperature (colours and contours in 0.50°C intervals, $T = 0°C$ indicated by thick contour), (b) salinity (colours and contours in 0.25 psu intervals, $S = 0$ indicated by thick contour) and (c) zonal and (d) meridional current velocity (colours and contours in 0.10 m s^{-1} intervals, $(u, v) = 0$ indicated by thick contour), as estimated by V42.

this has weak currents. Overall, the modelled currents are weak compared to the observations. The temperature in V42 is slightly higher than in R26. Below 200 m the temperature is close to being the same as in the observations (∼0.5°C in both observations and model). The salinity in both R26 and V42 are very close to the observations. The current is strongest in R26, but the direction of the current is better in V42.

6.2.3 Near-inertial velocity and energy

The observed near-inertial zonal velocity at I3 at 10 m depth for an event on the 16th of December 2008 ranged between ±0.10 m s^{-1}, see figure 6.11(a). For the entire observational period, the near-inertial velocity at I3 ranged between 0.05-0.20 m s^{-1}. The modelled zonal near-inertial velocity over the same period is shown in figure 6.12 for both R26 and V42 (note the different scale, compared to figure 6.11(a)). Here it is seen that the near-inertial velocities range between 0.01-0.02 m s^{-1} before the 14th and reaches ± 0.06 m s^{-1} on the 16th, after which they oscillate between ± 0.03 m s^{-1}. The near-inertial waves decrease faster in R26 than in V42. The modelled zonal near-inertial velocities are slightly weaker than the observed zonal near-inertial velocities.

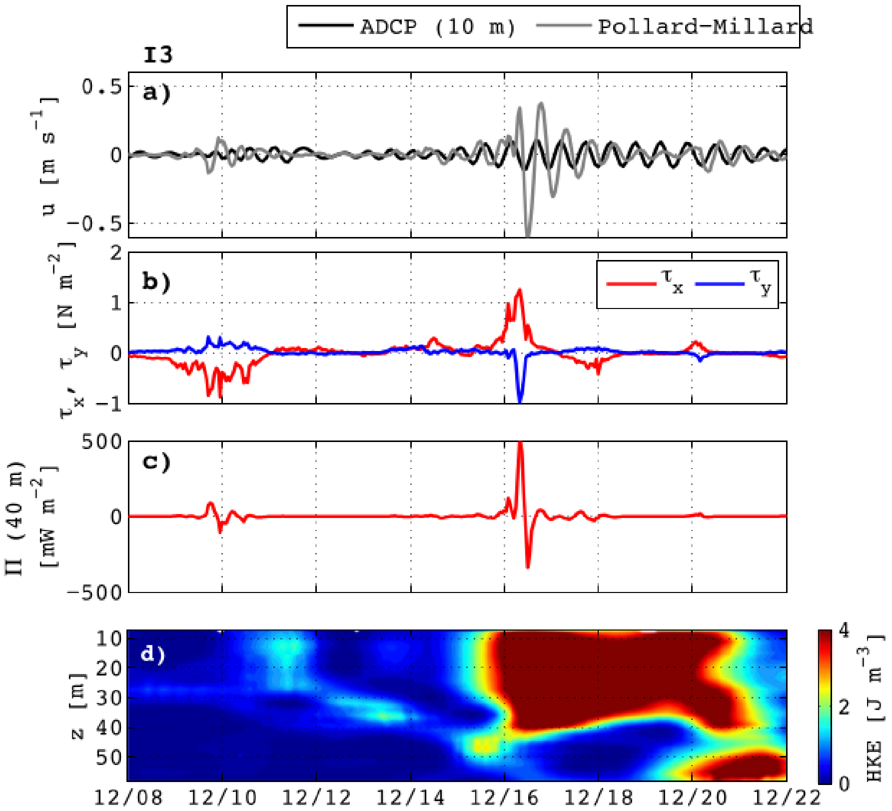

Figure 6.11: a) Observed and modelled near-inertial zonal velocity at I3, b) wind stress used to force model in Martini et al. (2014), c) predicted ML energy flux from wind to near-inertial motion (not used in this study) and d) near-inertial kinetic energy. Figure from Martini et al. (2014).

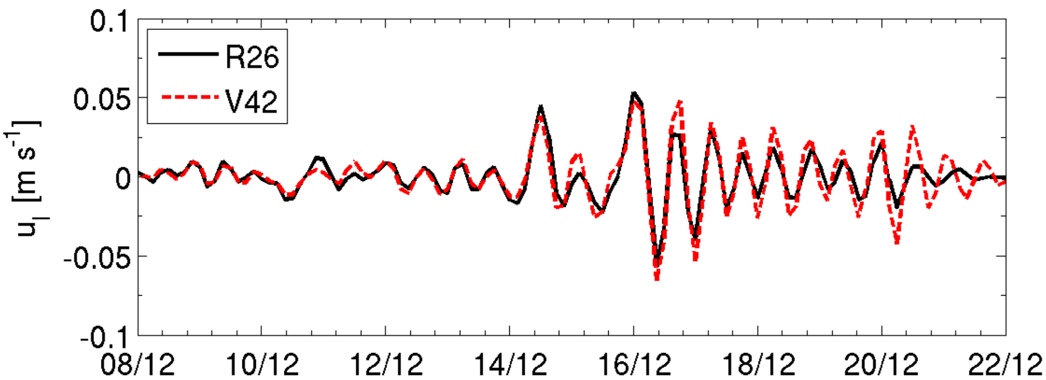

Figure 6.12: Near-inertial velocity for R26 (black) and V42 (red).

The near-inertial kinetic energy is shown in figure 6.11(d) indicating the observed near-inertial horizontal kinetic energy in the upper 60 m from the 8th to the 22nd of December 2008. There is enhanced near-inertial energy from the 16th to the 21th in the upper 40-50 m and from the 20th to the 22nd below 50 m. Martini et al. (2014) has connected this to a storm event occurring on the 16th of December. Figure 6.13(a) shows the zonal and meridional wind speed during the same period and figure 6.13(b) shows the near-inertial horizontal kinetic energy as estimated in R26. Results for V42 are shown in figure 6.13(c). The simulated wind shows a

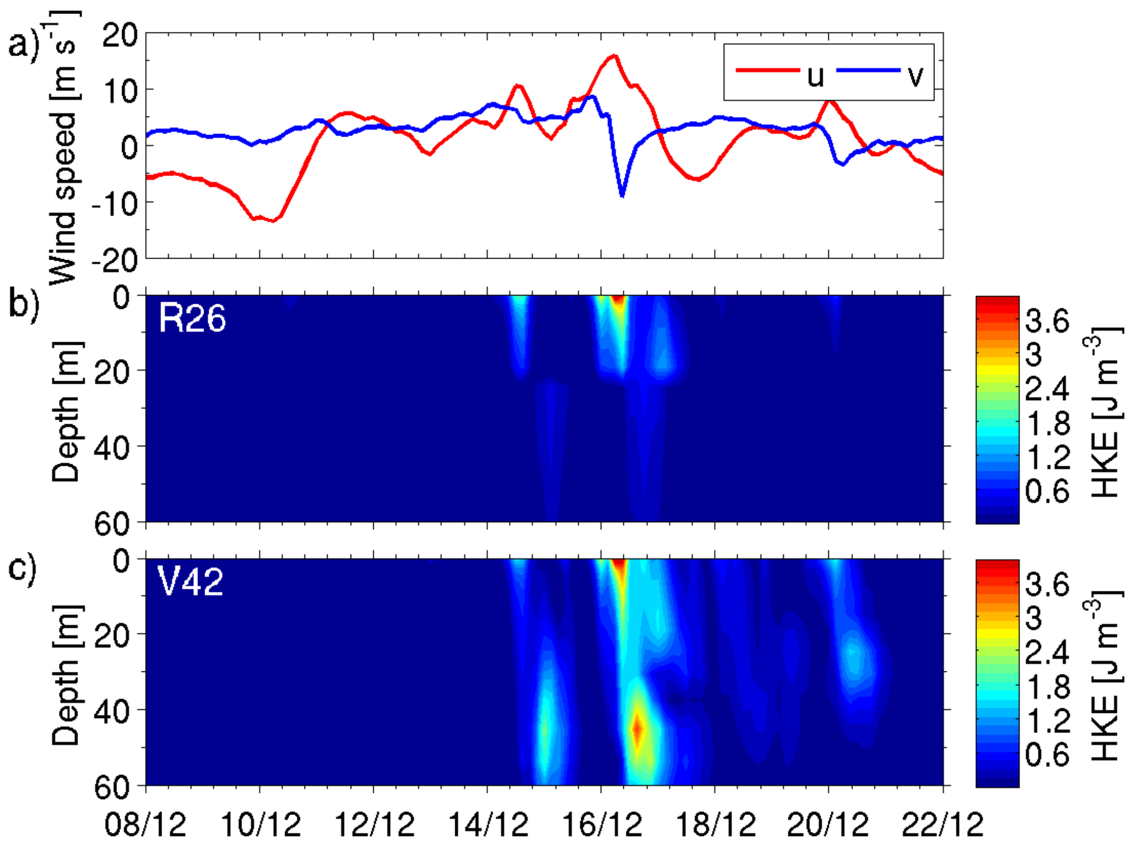

Figure 6.13: a) The wind speed in the east-west (red) and in the north-south (blue) direction. Near-inertial horizontal kinetic energy shown for b) R26 and c) V42.

strong western wind around the 10th of December and a southeastern wind around the 16th. This compares well with the observed wind stress shown in figure 6.11(b).

As the wind increases on the 16th there are regions of energy above 1.00 J m^{-3} down to 20-25 m in R26. Below 25 m, the near-inertial energy is still enhanced, but less than in the upper 25 m. In V42, HKE is enhanced on the 16th down to and below 60 m, with two areas of HKE above 3.50 J m^{-3}, one at the surface and one at 45 m. Further, in the following days there is still a near-inertial signal, down to 40-50 m. Before the strong winds, on the 15th at a depth of 30 to 60 m, there are enhanced levels of HKE as well. In the observations on the 15th, enhanced HKE is seen as well around 50 m depth.

Both of the two model experiments have too weak near-inertial energy signals, but they both capture an event simultaneously with an observed event. For this event, V42 reproduces the near-inertial energy signal down to and below 60 m. The event in V42 is generally closer to the observations than the event in R26. Martini et al. (2014) also investigates the distribution of HKE with depth. They find that elevated levels of HKE are traced down to 600 m in ice-free and ice-forming periods (figure not shown). A difference of $\sim$40% is observed between ice-free and ice covered conditions, for average depth-integrated HKE below 300 m. In the two model experiments, the kinetic energy is above 0.15 J m^{-3} down to 220 m in R26 and to 150 m in V42. In the three months shown here, R26 allows for the most energy to propagate out of the mixed layer and down. This is the opposite of what was found by examining a single event in December.

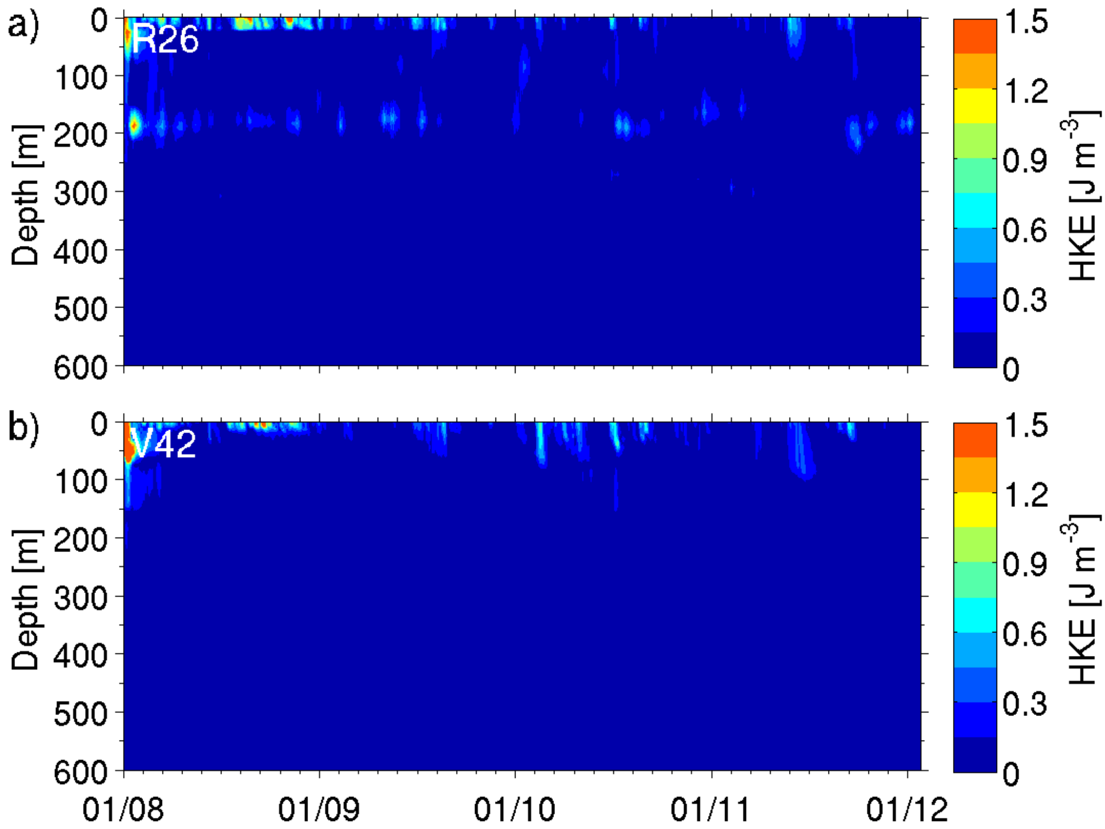

Figure 6.14: Near-inertial horizontal kinetic energy in 2008 shown for a) R26 and b) V42.

6.2.4 Wind

In Martini et al. (2014) the atmospheric forcing used is the Navy Operational Global Atmospheric Prediction System (NOGAPS) which is reanalysis data. However, Martini et al. (2014) argues that this reanalysis of the wind is too weak compared to observations. As a result of this, the observations are compared to wind-observations made at the Prudhoe Bay ~100 km away from the observation site. Figure 6.15 show the zonal and meridional components of the observed high-resolution 30-min winds, the 3-hour averaged of the observed wind and the 3-hour NOGAPS reanalysis winds. The winds are from November.

The zonal component (figure 6.15(a)) shows a strong western wind around the 3rd of November and around the 12th. These two winds reach velocities of 20 m s^{-1} in the observations and around 13 m s^{-1} in the reanalysis. In between these two strong western flows, the wind blows toward the east with velocities around 2-5 m s^{-1} for the reanalysis and 8 m s^{-1} for the observations. The modelled zonal wind, figure 6.16(a), shows the same temporal evolution as the observations, but the strength of the wind is closer to the reanalysis with maximum western flows on the 3rd and the 11th-12th of Noevmber reaching 12 m s^{-1}. The weak eastern flow between the 5th and the 9th is about 3 m s^{-1}.

The observed meridional wind is weaker than the zonal wind and changes direction more frequently. Generally, there is a northern flow around the 3rd-4th of November of 5 m s^{-1} and a southern flow on the 7th oscillating around 5-6 m s^{-1}. After the 9th, the meridional wind

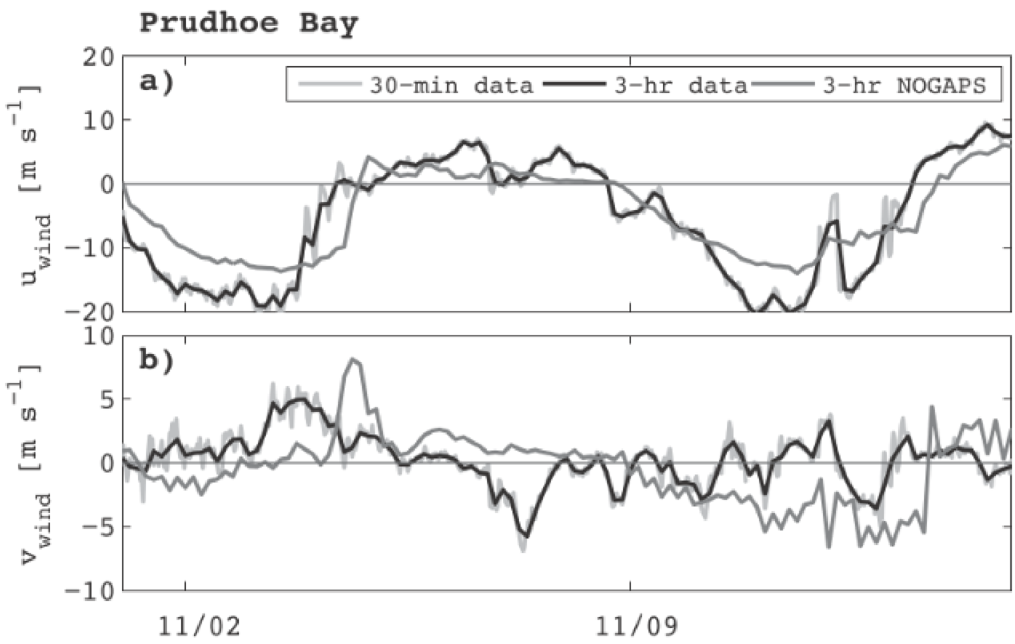

Figure 6.15: a) Observed 30-min wind at Prudhoe Bay, b) 3-hour average of 30-min observations and c) reanalysis 3-hour wind at site moorings. Figure modified from Martini et al. (2014).

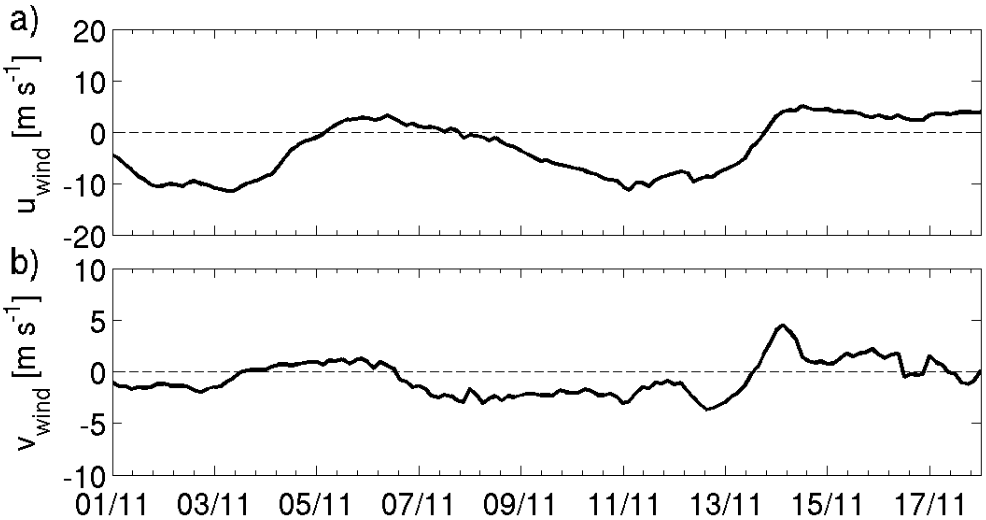

Figure 6.16: Reanalysis wind speed used in R26 and V42 from the grid point closest to Prudhoe Bay. a) show the zonal and b) the meridional wind speed.

oscillates between north and south. The reanalysed wind shows a northern peak about a day later than the observed wind, but it is stronger. It is not southern again until the 9th, after which it remains southern almost until the end of the measurements. The modelled meridional wind is weaker than the zonal component and the relatively strong northern wind on the 3rd is not seen. It follows approximately the same evolution as the observed wind, changing between northern and southern directions at the same time as the observations, but it is weaker than the observations. Hence, the modelled zonal wind component is similar to the reanalysis wind and the meridional wind component to the observations at Prudhoe Bay.

7 Discussion

The quality of the results from chapters 5 and 6 are discussed through comparison with observations and previous studies. Based on this, the impact of near-inertial waves on the Arctic Ocean is discussed.

7.1 Ice cover

The ice cover works as a lid on the ocean, damping the energy from the wind as well as the motions in the ocean. It is therefore important to model a realistic ice concentration. Comparing the sea ice concentration, as observed from satellite [UIUC, Web 4], to the modelled sea ice concentration reveals large differences, the greatest of which is seen in 2005. Figure 7.1 shows the daily averaged ice cover for September 15th 2005 (figure 7.1(a)) and as modelled in R26 and V42 (figure 7.1(b)). It is seen that the ice concentration in R26 is significantly smaller than the observed ice concentration. The North Pole is not covered by ice in R26, and it appears that only small patches are compact ice (ice concentration of 100%). A large fraction of the eastern Arctic Ocean is also not covered by sea ice in the model, but it is in reality. V42 captures the ice cover somewhat better, however the North Pole is ice-free.

This makes a great difference on locations for near-inertial events. According to the observations, the four locations investigated for near-inertial activity in this study, are all covered by ice. However, these events are selected using three criteria, one being that the ice cover should be less than 20% (section 4). For a modelled sea ice concentration closer to the observed sea ice concentration, fewer near-inertial events will occur, hence the number of near-inertial events found in this study is probably exaggerated.

The ice concentration for April 24th 2007 is shown in figure 7.2. The model captures the ice cover better than in 2005 and the difference between R26 and V42 is small.

The ice concentration for September 15th 2008 is shown in figure 7.3. This ice cover is closer to the observed ice cover, than on the same day in 2005, but there is still not enough compact ice. Again, the ice concentration at the North Pole is not 100%, as is observed. The location of I3 on the Beaufort continental slope is ice-free on September 15th in both the observations and on the two model experiments.

Finally, the ice concentration for November 11th 2013 is shown in figure 7.4. Here it is seen that H10 is closest to the observed ice cover. R26 has two distinct differences: first of all, the sea ice is too far north along the eastern coast of Greenland. Secondly, the southern part of the Canada Basin is ice-free in R26 but not in the observations or in H10. As this is the location of case 5, the difference in ice cover can partly explain the difference between R26 and H10. As discussed earlier (section 5.2.5), there are differences between the wind fields in the two experiments, but since the wind field is used to force the model, and not the other way around, the difference in wind speed cannot be explained by the difference in ice cover.

These results show that the sea ice concentration is at times much lower in the model than observed. Especially in September 2005 and 2008 is the sea ice concentration very different from the observations and the North Pole is not covered by ice. This suggests that the sea ice is not modelled well enough. The sea ice concentration in 2005 is observed to be too small in the

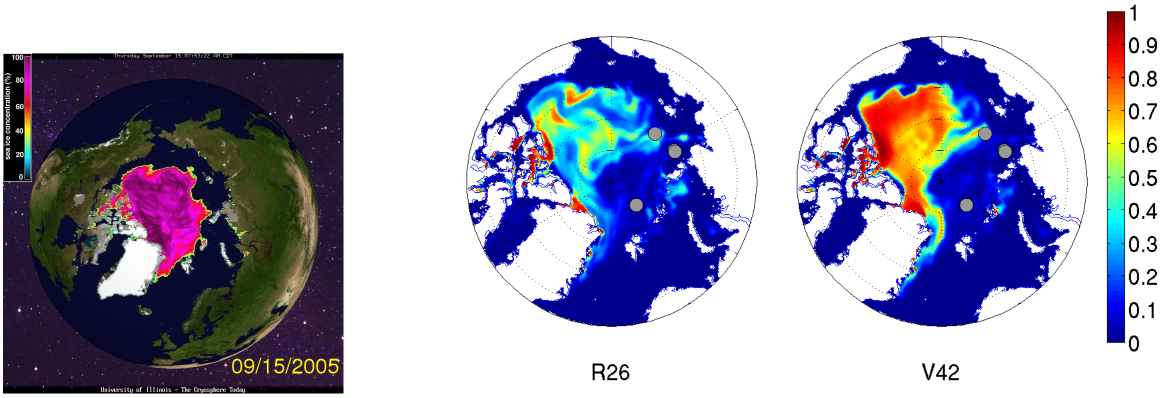

(a) (b)

Figure 7.1: Observed a) and modelled b) sea ice concentration on the 15th of September 2005. In b) is shown the concentration for R26 (left) and V42 (right). Observations from UIUC, Web 4. Grey dots represent the near-inertial events investigated in this study.

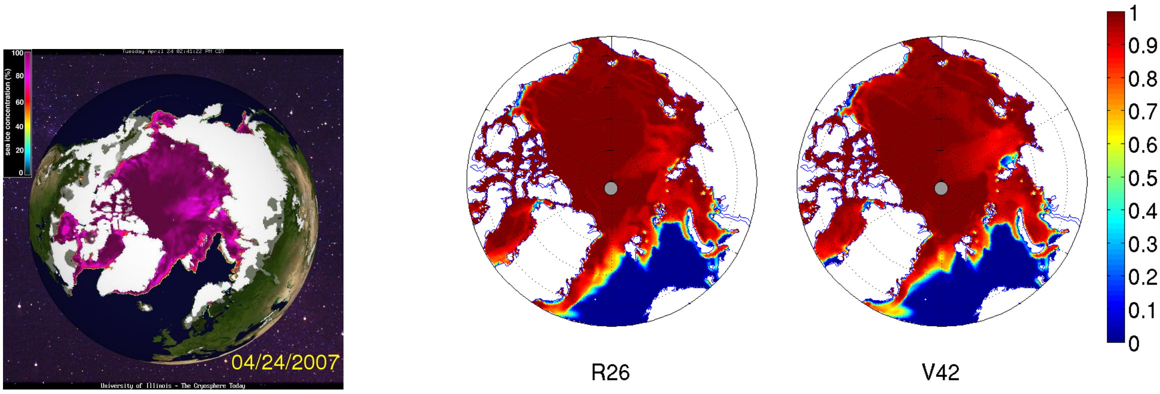

(a) (b)

Figure 7.2: Observed a) and modelled b) sea ice concentration on the 24th of April 2007. In b) is shown the concentration for R26 (left) and V42 (right). Observations from UIUC, Web 4.

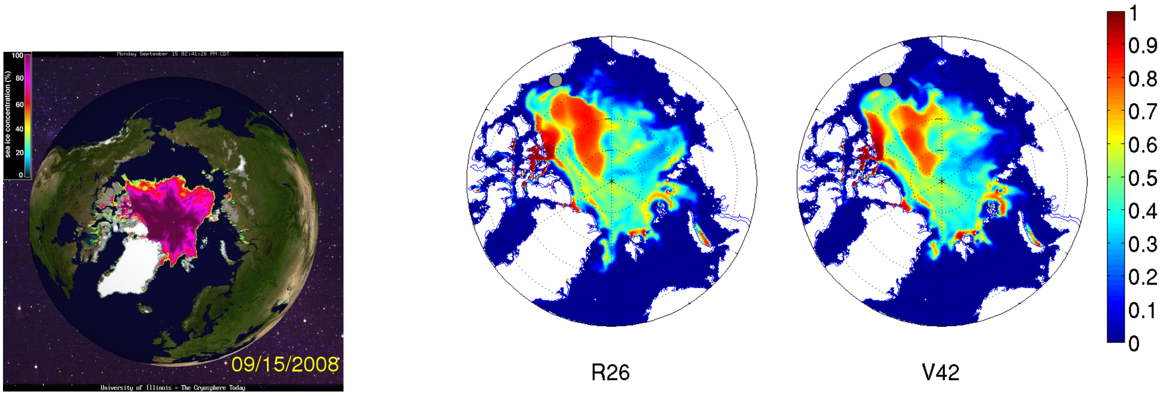

(a) (b)

Figure 7.3: Observed a) and modelled b) sea ice concentration on the 15th of September 2008. In b) is shown the concentration for R26 (left) and V42 (right). Observations from UIUC, Web 4. Grey dots represent the near-inertial events investigated in this study.

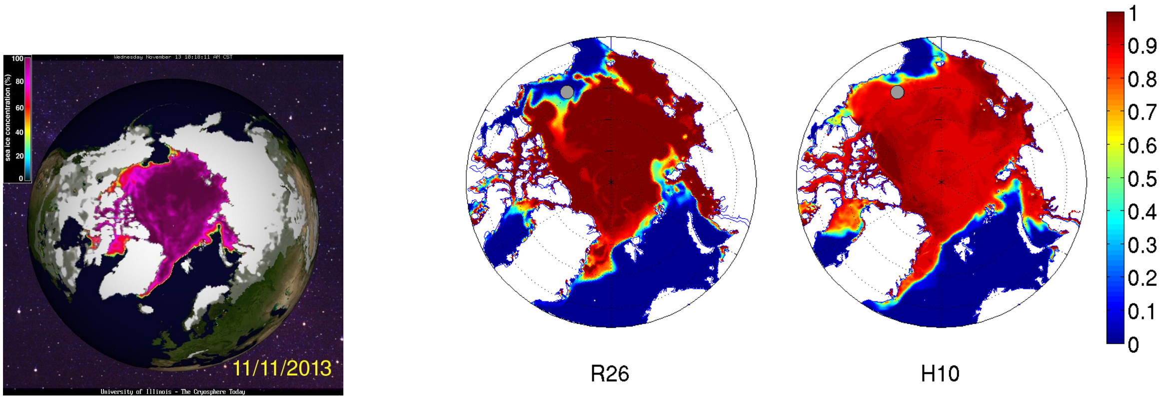

(a) (b)

Figure 7.4: Observed a) and modelled b) sea ice concentration on the 11th of November 2013. In b) is shown the concentration for R26 (left) and V42 (right). Observations from UIUC, Web 4. Grey dots represent the near-inertial events investigated in this study.

Arctic Ocean in other HYCOM experiments as well.

As a result of the smaller ice cover in the model, the number of potential near-inertial events found in this study, is probably overestimated. However, as the focus on near-inertial events in the Arctic is a result of the decrease in sea ice concentration, the Arctic sea ice cover could potentially evolve to a new state, more similar to the ice cover seen in figures 7.1(b) and 7.3(b). The results found here can perhaps give an idea of how near-inertial waves will behave in the future, but there are many unknown factors not taken into account in this. The melting of sea ice will potentially alter the temperature and salinity of the water and the dynamics of the water mass transport will probably be affected as well.

7.2 Current velocity

The observed velocities in Fer (2014) and in Martini et al. (2014) are compared to the modelled velocity over the same periods and locations. The modelled velocities found in sections 5.1 and 5.2, typically ranged between 0.02-0.03 m s^{-1}, reaching maxima of 0.12 m s^{-1} for R26 and 0.13 m s^{-1} in V42 in the zonal (westward) direction. The meridional velocities are smaller with a maximum of 0.05 m s^{-1} in the southern direction, for both R26 and V42.

The observed currents in April 2007 were typically 0.1-0.2 m s^{-1} (section 6.1.1). The modelled maximum velocities are therefore in the low end of the observed, and generally the modelled velocity is lower.

The velocities measured by Martini et al. (2014) ranges between 0.20-0.50 m s^{-1} (see section 6.2). The maximum modelled current velocities for the same time and place are 0.31 and 0.22 m s^{-1} for the zonal component and 0.27 and 0.22 m s^{-1} for the meridional component, for R26 and V42, respectively (sections 6.2.1 and 6.2.2). Hence, the maximum modelled velocities in the upper ocean are in the observed range, but in the low end. Overall, the modelled velocity is weaker compared to the observations. Below 200 m, the velocity in the models are lower than 0.10 m s^{-1}. The observed velocity typically ranges between ± 0.10 m s^{-1} as well, but occasionally becomes higher. The direction of the modelled current is mostly northwestern, as is the case in the observations. The sporadic southern and southeastern events in the 2008 observations are not captured well in neither R26 nor V42.

Comparing R26 to H10 in section 5.2.5 shows that the current velocity is similar in the two cases. The only exception is the event from the 13th to the 17th which is not reproduced in

H10. The modelled velocity in both R26 and H10 ranges between 0.10-0.20 m s^{-1} and in R26 they reach as high as 0.35 m s^{-1}. This is similar to the current velocities found in the four cases in 2005 and the modelled events in 2007 and 2008.

Hence, the modelled velocity is weaker than the observations, both in the event occurring under ice in April 2007, and in the measurements from August to December 2008, occurring both in ice-free and ice-covered conditions. V42 generally captures the direction of the current better than R26, but it is not the case every time. The velocity is generally higher in V42 compared to R26 in the four cases in 2005 and the event in April 2007. It is the opposite for the measurements in 2008; here R26 has the highest velocities.

7.3 Near-inertial waves

The maximum near-inertial speed for the four events ranges between 0.20 m s^{-1} and 0.32 m s^{-1}, occurring in July and in September, respectively (see section 5.1). In V42, the maximum near-inertial speed ranges between 0.15 and 0.34 m s^{-1} (section 5.2). This spans over a wider range, reaching a maximum near-inertial velocity slightly higher than in R26.

The near-inertial waves in 2013 modelled by R26 and H10 are compared in section 5.2.5. The near-inertial velocity ranges around 0.03-0.05 m s^{-1} and 0.02-0.03 m s^{-1}, respectively. However, the near-inertial velocity in R26 becomes as high as 0.18 m s^{-1} during the near-inertial event. Since this event is not seen in H10, the maximum near-inertial velocity in H10 is around 0.08-0.09 m s^{-1}.

In Martini et al. (2014) the near-inertial velocities typically ranged from 0.05 to 0.20 m s^{-1}, but the event on December 16th ranged between $\pm$ 0.10 m s^{-1}, whereas the modelled velocity for this event was $\pm$ 0.06 m s^{-1} (see section 6.2.3). The near-inertial waves decrease faster in R26 than in V42.

Outside the Arctic, Park and Kim (2005) uses Argo profiling floats to show that the monthly averaged near-inertial amplitude peaks in September in the North Atlantic (30-60°N) and in October for the North Pacific (30-60°N). The seasonal variability between the monthly averages is 0.11-0.17 m s^{-1} and 0.13-0.23 m s^{-1}, respectively. Jochum et al. (2013) uses a numerical study to estimate average near-inertial velocities over 40 years to be around 0.02-0.03 m s^{-1} in the Arctic Ocean. The near-inertial velocities increase with decreasing latitude, reaching velocities up to 0.20 m s^{-1} at the Equator.

The near-inertial velocities found in this study were slightly weaker for a specific event in December 2008 than the observations. The near-inertial velocities found in Park and Kim (2005) and Jochum et al. (2013) are monthly and 40-year means, respectively. This cannot be compared to the maximum near-inertial velocities found in this study, or be used to say if the near-inertial velocities are higher than the observations or not. They can, however, be used to say if the modelled near-inertial velocities are of the same order of magnitude and relatively close to what is observed before. Doing this comparison between the values from Park and Kim (2005) and Jochum et al. (2013), and the modelled near-inertial velocities found in this study, shows that they are comparable and relatively close to each other.

The total current velocities are found to be weaker in the model compared to the observations, and the modelled near-inertial velocity for the specific event in 2008 is weaker than the observations for the same event. From this, the modelled near-inertial velocities should be weaker than the observations. In addition to this, they are comparable to what is observed, both in and outside of the Arctic.

Increasing the number of vertical layers increases the near-inertial velocities slightly, and for the event in December 2008 the near-inertial waves persists longer. For this specific event V42 is closer to the observations than R26.

7.4 Kinetic energy

The near-inertial velocity is used to calculate the near-inertial horizontal kinetic energy (HKE). For the event in December 2008 observed by Martini et al. (2014) the energy in the model was too weak, but V42 reproduced it better than R26, as is seen in section 6.2.3. The kinetic energy found in R26 and V42 when comparing to the observations from April 2007 from Fer (2014) is very weak (section 6.1.2). There is a near-inertial signal propagating down from the surface, but it is below the critical value for enhanced energy set to 0.15 J m^{-3}. The energy found in Fer (2014) is much higher at the surface, up to 90 J m^{-3}.

For the four events in 2005 described in section 5, the depth-integrated energy in the mixed layer, E_{ML}, ranges between 264 and 1081 J m^{-2}. Below the mixed layer, $E_{Below\ ML}$, it ranges between 103 and 305 J m^{-2}, see section 5.1. Increasing the number of vertical layers (V42) changes this to be 169-1095 J m^{-2} and 59-488 J m^{-2}, respectively (section 5.2).

Park and Kim (2005) calculated the mixed layer inertial energy (comparable to E_{ML}) averaged over 1998-2003 and averaged over the area in each of the three basins: the North Atlantic (30-60°N), the North Pacific (30-60°N) and the Southern Ocean (30-60°S). From this they estimated that the seasonal variability in energy is largest for the North Atlantic (difference between highest and lowest energy is 870 J m^{-2}, with a maximum inertial energy ∼3000-3200 J m^{-2}). In the North Pacific the seasonal variability is 772 J m^{-2} and in the Southern Ocean it is 311 J m^{-2}. The average energy taken over the North Atlantic and the North Pacific from 1997-2003 is approximately 1165 J m^{-2}.

This is higher than the energies found in this study. The near-inertial speed is of similar magnitude in this study and in Park and Kim (2005), but the velocities found in Park and Kim (2005) are monthly averages, so they are bound to be lower than the instantaneous velocities found here. However, in Park and Kim (2005) it is assumed that the inertial amplitude is uniform in the mixed layer and the mixed layer inertial energy is then calculated as the product between the inertial amplitude and the mixed layer depth. The inertial waves decrease with depth, even in the mixed layer, which could be a possible cause for the kinetic energy to be higher in Park and Kim (2005) than the HKE found in this study, even though the near-inertial velocities are of comparable magnitude.

7.5 Temperature and salinity

Mixing in the ocean is greatly influenced by the distribution of temperature and salinity. In the Arctic Ocean a cold halocline layer isolates the cold mixed layer from the warm water below. It is therefore essential to model this properly.

In general, the Atlantic Water and the Pacific Summer Water are not reproduced in any of the three model experiments. The Atlantic Water is seen as a tongue of warm water in figure 5.24 in section 6.1.3, but the water is too cold in the simulation.

For the four events in 2005 it is shown that the halocline is stronger in V42 than in R26 and that in three of the four cases, the mixed layer salinity is lower in V42 than in R26 (see sections 5.1 and 5.2). The thermocline varies from case to case, with R26 having the stronger thermocline in case 1 and 4, and V42 having the strongest thermocline in cases 2 and 3. This results in a stronger stratification in V42 than in R26.

An important difference is that the water beneath the mixed layer becomes so warm in V42, that it is warmer than the surface mixed layer (figure 5.24 in section 5.2). This occurs for cases 2 and 3 in V42, but only case 3 in R26. Further, the cold halocline layer is not seen in these four events, since the upper limit of both the thermocline and the halocline is located at the same depth.

The monthly averaged temperature and salinity changes greatly from R26 to H10 (section 5.2.5). The mixed layer temperature increases by 1.37°C and the salinity decreases by 1.35 psu. In addition to this, the mixed layer shoals by 17 m. The cold halocline layer is not seen in neither R26 or H10.

By comparing the two model experiments, R26 and V42, with observations from 2007 and 2008 it is shown that the observed stratification is stronger than in the model.

The surface mixed layer is slightly colder and more saline in R26 and V42 for 2007, compared to the observations (section 6.1.3). The halocline in R26 is closer to the observed halocline than the halocline in V42, but the model does not capture the shape of the halocline. The model does not capture the shape of the thermocline either. In the observations, the temperature changes first slowly with depth, then more rapidly. In R26, the temperature gradient is more or less linear with depth and the gradient is strong just below the mixed layer in V42, but becomes weaker with depth. The result of this is that the stratification is stronger in the observations than in the model and stronger in R26 than in V42. Just below the mixed layer, the stratification in V42 is stronger than in R26. However, the water is too cold with depth in R26, reaching a temperature maximum of 0.02°C, compared to around 1.00°C in the observations. The temperature maximum is slightly higher, 0.46°C, in V42, but still too cold.

For the observations in 2008 the surface mixed layer was not measured, see sections 6.2.1 and 6.2.2. However, it can still be estimated that R26 is about 0.5° warmer at 100-200 m depth and that the thermocline is weaker than the observed thermocline. The temperature in V42 is even warmer and hence the thermocline even weaker than in R26. The salinity is closer to the observations in R26 than in V42, but the halocline is still weaker. This indicates that the stratification is stronger in the observations than in both R26 and V42.

Overall, the stratification becomes stronger in the four events in 2005 from R26 to V42, but it is the opposite when comparing to observations in 2007 and 2008.

7.6 Wind

Since the currents are driven by the wind, the performance of the wind in the model is of great importance. Rimac et al. (2013) show that the spatial and temporal resolution of the atmospheric fields affect the wind power input to near-inertial motion. By changing from a low-resolution (6-hourly and 1.88°) to a high-resolution (1-hourly and 0.35°) atmospheric field, the kinetic near-inertial energy increases by a factor three. The wind power input to near-inertial motion increases from 0.3 TW to 1.1 TW.

In this study, the ERA-Interim reanalysis winds are used. Lindsay et al. (2014) tests seven different reanalysis products in the Arctic and find that out of the seven products, ERA-Interim correlates best with observations. Therefore, the atmospheric field used in this study should be close to the observations. However, the ERA-Interim reanalysis winds are weaker than the winds observed at Prudhoe Bay in Martini et al. (2014), section 6.2.4. The modelled winds are closer to the reanalysis winds which Martini et al. (2014) argues are too weak.

The observed winds in Fer (2014) are similar to the winds from ERA-Interim, see section 6.1.1. The magnitude and time evolution are close to being the same. Due to this consistency, the difference between the model and the observations is potentially caused by the ocean mixed layer model.

The winds from ERA-Interim are compared to the ECMWF operational forecast in November 2013 in section 5.2.5. In the event investigated using both R26 and H10, the wind speed in the two atmospheric systems compare well, most of the time. However, ERA-Interim captures a strong event on the 13th to the 17th of November. This is not present in the ECWMF operational forecast. Since it is this event that generates the near-inertial event that should have been investigated, the near-inertial event is not present in H10. The cause for this missing event in H10 is not clear, since both the temporal and the spatial resolution is higher in H10, which should improve it. However, atmospheric fields are sensitive to small changes.

7.7 The impact from near-inertial waves on the Arctic mixed layer and stratification

The results found in this study suggests that the model underestimates the current velocity and hence the near-inertial current velocity. The stratification is too weak in the model compared to the observations as well. The combination of the weaker near-inertial currents and stratification results in a situation similar to what is observed: the wind-generated near-inertial waves penetrate down into the pycnocline, but not through it. The mixed layer does not warm up, it cools in three of the four cases. The only time it warms up is in July, but this is more likely due to solar heating, as the water below is colder than at the surface.

The hypothesis that the mixed layer warms up due to increased mixing caused by near-inertial waves in the Arctic Ocean, is investigated in many studies.

Rainville and Woodgate (2009) find that in ice-free regions in summer the wind is able to generate strong near-inertial waves (<0.05 m s^{-1} in ice-covered regions, as high as 0.30 m s^{-1} in ice-free regions). These deepen the mixed layer and erode into the pycnocline.

Yang et al. (2004) find, from buoy measurements in the Beaufort Sea, that several events with enhanced mixing occurred but they only reached the halocline or the upper thermocline and that mixing only occurred when the stratification was weak (spring and winter). Mixing events were observed where warm thermocline water was drawn up into the mixed layer. The measured events were not in the centre of the storm systems, so Yang et al. (2004) suggests that it is possible for near-inertial waves generated in the center of a storm system to penetrate further down.

Neither Toole et al. (2010) nor Shaw et al. (2009) observe near-inertial waves penetrating down into warmer waters. Toole et al. (2010) observes a freshening and warming of the mixed layer and hence an increased stratification, isolating the near-inertial waves from the warm Pacific Summer Water underneath. Shaw et al. (2009) suggests that the heat flux at the base of the mixed layer is too small to contribute to melting of the sea ice. The decrease in sea ice allows for more solar insolation to penetrate into the ocean, and thus heating up the mixed layer. This will, as Toole et al. (2010) also suggests, freshen and warm the mixed layer and strengthen the stratification. However, the decrease in sea ice cover exposes more ocean surface to the wind, enhancing the effect from wind-driven events and thereby generate stronger near-inertial events. The amount of warm thermocline water that can interact with the mixed layer depends on this balance between the potential enhanced stratification and stronger mixing caused by near-inertial waves.

8 Conclusion

The impact of near-inertial waves on the stratification in the Arctic Ocean was investigated in this thesis through the use of the coupled ice-ocean model HYCOM. To investigate this, four events in 2005 were selected and investigated in detail. Enhanced near-inertial energy were found in all four events and near-inertial waves were observed penetrating through the base of the mixed layer, down into the upper pycnocline. The upper limit of the thermo- and halocline were located at the same depth, i.e. the characteristic cold halocline layer was not present in the model. As the cold halocline layer is thought to be the strong barrier between the cold, fresh mixed layer and the warmer waters underneath, the absence of it should allow for more warm water to be drawn up to the surface. This was not observed in the four cases investigated in this study, but it has been observed in other studies [Yang et al. (2004)].

Increasing the number of vertical layers in the model, V42, resulted in a stronger stratification and generally warmer water, compared to the reference experiment R26. This also caused the water beneath the mixed layer to be warmer than the mixed layer in cases 2 and 3, as opposed to only in case 3 in R26.

Comparing this to the observations in 2007 and 2008 and previous studies showed that the observed stratification was stronger than in R26. The stratification in V42 was weaker compared to R26, the opposite of what was seen from the four cases in 2005. Generally, R26 agreed better with the observations than V42.

The observed currents, and hence near-inertial currents, were stronger than the modelled currents. The combination of the weaker modelled currents and the weaker stratification, resulted in wind-induced near-inertial waves. These eroded into the halocline, but not through it, similar to what has been observed. As the model did not predict the cold halocline layer, the near-inertial waves eroded into the thermocline and the halocline at the same time. However, this did not result in a warming of the mixed layer. In three out of the four cases investigated in 2005, the mixed layer cooled during and after a storm. Only in July was the mixed layer warming up, but this was probably a result of solar radiation and a thinning mixed layer.

The cooling of the mixed layer was most likely due to the temperature decreasing with depth in most of the cases, since the mixing drew up water from beneath. Only in R26 in case 3 and in V42 in cases 2 and 3 was the temperature higher at depth than in the mixed layer, allowing for warm water to be mixed into the surface mixed layer. However, the stratification was too strong for mixing to occur.

The model have some shortcomings. First of all, the ice cover in September 2005 and 2008 were much too small compared to observations. Most noteworthy was the lack of sea ice on the North Pole. Secondly, the warm Atlantic Water at around 300 m depth was too cold or there was not enough of it. The warm Pacific Summer Water located around 50 m in the western Arctic Ocean was not seen at all. And finally, as mentioned above, the missing cold halocline layer was not present either.

Near-inertial waves are likely to become stronger in the Arctic Ocean as the sea ice cover decreases and the ocean surface is more exposed to the wind. As observed by Toole et al. (2010) and Shaw et al. (2009) the stratification enhances as well, so even though the near-inertial waves might become stronger, they may not be strong enough to cause mixing into the warmer water below the halocline and thus change the sea-surface temperature. The increased turbulent mixing on the mixed layer can potentially change the water mass formation and water transport in the Arctic as well. Further observations and model simulations are needed to estimate how large an impact the decreasing ice cover has on the Arctic Ocean.

Bibliography

Aagaard, K.; Coachman, L. K., and Carmack, E., 1981: "On the halocline of the Arctic Ocean". *Deep-Sea Research Part A: Oceanographic Research Papers*, **28**(6), pp. 529–545.

Alford, M. H; Cronin, M. F., and Klymak, J. M., 2012: "Annual cycle and depth penetration of wind-generated near-inertial internal waves at Ocean Station Papa in the Northeast Pacific". *Journal of Physical Oceanography*, **42**, pp. 889–909.

Bleck, R., 2002: "An oceanic general circulation model framed in hybrid isopycnic-Cartesian coordinates". *Ocean Modelling*, **37**, p. 55.88.

Bleck, R.; Halliwell, G.; Wallcraft, A.; Carroll, S. N.; Kelly, K. A., and Rushing, K. V., 2002: *Hybrid Coordinate Ocean Model, User's Manual*.

Brydon, D.; Sun, S., and Bleck, R., 1999: "A wind-driven isopycnic coordinate model of the North and Equatorial Atlantic Ocean 1. Model development and supporting experiments". *Journal of Geophysical Research*, **104**, pp. 1537–1540.

D'Asaro, E. A., 1985: "The energy flux from the wind to near-inertial motions in the surface mixed layer". *Journal of Physical Oceanography*, **15**, pp. 1043–1059.

Dohan, K. and Davis, R. E., 2010: "Mixing in the Transition Layer During Two Storm Events". *Journal of Physical Oceanography*, **41**, pp. 42–66.

Dosser, H. V. and Rainville, L., 2014: "Near-inertial internal wave field in the Canada Basin from Ice-Tethered Profilers". *Journal of Physical Oceanography*, **44**, pp. 413–425.

ECMWF, Web 3. "ECMWF: ERA-Interim". `http://www.ecmwf.int/en/research/climate-reanalysis/era-interim`. [Online; Accessed 2014-06-05].

Emery, W. J. and Thomson, R. E., 1998: *Data analysis methods in physical oceanography*. Elsevier Science Ltd, United Kingdom, 1. edition.

Fer, I., 2009: "Weak vetical diffusion allows maintenance of cold halocline in the Central Arctic". *Atmospheric and Oceanic Science Letters*, **2**(3), pp. 148–152.

Fer, I., 2014: "Near-inertial mixing in the central Arctic Ocean". *Journal of Physical Oceanography*. doi: 10.1175/JPO-D-13-0133.1. In press.

Fer, I.; Skogseth, R., and Geyer, F., 2010: "Internal waves and mixing in the marginal ice zone near the Yermak Plateau". *Journal of Physical Oceanography*, **40**, pp. 1613–1630.

Furuichi, N.; Hibiya, T., and Niwa, Y., 2008: "Model-predicted distribution of wind-induced internal wave energy in the world's oceans". *Journal of Physical Research*, **113**, pp. 1–13.

Garrett, C., 2001: "What is the 'near-inertial' band and why is it different from the rest of the internal wave spectrum?". *Journal of Physical Oceanography*, **31**, pp. 962–971.

Holton, J. R., 2004: *An introduction to dynamic meteorology*. Elsevier Academic Press, San Diego, California, 4. edition.

Hunke, E. C.; Lipscomp, W. H.; Turner, A. K.; Jeffrey, N., and Elliott, S.: *CICE: The Los Alamos Sea Ice Model, Documentation and Software User's Manual, Version 5.0*.

IPCC, 2013: *Technical Summary. In: Climate Change 2013: The Physical Science Basis. Contribution of Working Group I to the Fifth Assessment Report of the Intergovernmental Panel on Climate Change [Stocker, T.F., D. Qin, G.-K. Plattner, M. Tignor,S.K. Allen, J. Boschung, A. Nauels, Y. Xia, V. Bex and P.M. Midgley (eds.)].* Cambridge University Press, Cambridge, United Kingdom and New York, NY, USA.

Jochum, M.; Briegleb, B. P.; Danabasoglu, G.; Large, W. G.; Norton, N. J.; Jayne, S. R.; Alford, M. H., and Bryan, F. O., 2013: "The impact of oceanic near-inertial waves on climate". *Journal of Climate*, **26**, pp. 2833–2844.

Kantha, L. H. and Clayson, C. A., 2000: *Numerical models of oceans and oceanic processes.* Academic Press, San Diego, California.

Knauss, J. A., 2005: *Introduction to physical oceanography.* Waveland Press, Inc, Long Grove, Illinois, 2. edition.

Large, W. G., 1994: "Oceanic vertical mixing: A review and a model with a nonlocal boundary layer parameterization". *Reviews of Geophysics*, **32**, pp. 363–403.

Large, W. G. and Crawford, G. B., 1995: "Observations and simulations of upper-ocean response to wind events during the Ocean Storms Experiment". *Journal of Physical Oceanography*, **25**, pp. 2831–2852.

Lindsay, R.; Wensnahan, M.; Schweiger, A., and Zhang, J., 2014: "Evaluation of seven different atmospheric reanalysis products in the Arctic". *Journal of Climate*, **27**, pp. 2588–2606.

Map of the Arctic Ocean, Web 1. "Map of the Arctic Ocean". `http://geology.com/articles/arctic-ocean-features/`. [Online; Accessed 2014-10-21].

Martin, T.; Steel, M., and Zhang, J., 2014: "Seasonality and long-term trend of Arctic Ocean surface stress in a model". *Journal of Geophysical Research: Oceans*, **119**, pp. 1723–1738.

Martini, K. I.; Simmons, H. L.; Stoudt, C. A., and Hutchings, J. K., 2014: "Near-inertial internal waves and sea ice in the Beaufort Sea". *Journal of Physical Oceanography*, **44**, pp. 2012–2234.

Oceanographers.net, Web 2. "Oceanographers.net". `http://www.oceanographers.net/forums/showthread.php?429-Normal-Mode-Oscillation-in-the-Ocean`. [Online; Accessed 2014-09-16].

Park, J. J. and Kim, K., 2005: "Global statistics of inertial motions". *Geophysical Researh Letters*, **32**, pp. 1–5.

Pedlosky, J., 1996: *Ocean circulation theory.* Springer, Germany, 1. edition.

Pinkel, R., 2005: "Near-inerital wave propagation in the Western Arctic". *Journal of Physical Oceanography*, **35**, pp. 645–665.

Pollard, R. T. and Millard Jr., R. C., 1970: "Comparison between observed and simulated wind-generated inertial oscillations". *Deep-sea researh*, **17**, pp. 813–821.

Pollard, T. R., 1970: "On the generation by winds of inertial waves in the ocean". *Deep-sea researh*, **17**, pp. 795–812.

Polyakov, I. V., 1997: "Maintenance of the Arctic Ocean large-scale baroclinic structure by the M2 tide". *Polar Research*, **13**, pp. 219–232.

Rainville, L. and Woodgate, R. A., 2009: "Observations of internal wave generation in the seasonally ice-free Arctic". *Geophysical Research Letters*, **36**, pp. 1–5.

Rainville, L.; Lee, C. M., and Woodgate, R. A., 2011: "Impact of wind-driven mixing in the Arctic Ocean". *Oceanography*, **24**(3), pp. 136–145.

Rimac, A.; von Storch, J.; Eden, C., and Haak, H., 2013: "The influence of high-resolution wind stress field on the power input to near-inertial motions in the ocean". *Geophysical Researh Letters*, **40**, pp. 1–5.

Shaw, W. J.; Stanton, T. P.; McPhee, M. G.; Morison, J. H., and Martinson, D. G., 2009: "Role of the upper ocean in the energy budget of Arctic sea ice during SHEBA". *Journal of Geophysical Research*, **114**, pp. 1–21.

Simmons, H. L. and Alford, M. H, 2012: "Simulating the long-range swell of internal waves generated by ocean storms". *Oceanography*, **25**(2), pp. 30–41.

Sirevaag, A.; de la Rosa, S.; Fer, I.; Nicolaus, M.; Tjernström, M., and McPhee, M. G., 2011: "Mixing, heat fluxes and heat content evolution of the Arctic Ocean mixed layer". *Ocean Science Discussions*, **8**(1), pp. 247–289. doi: 10.5194/osd-8-247-2011.

Suh, G. Y., 2011: "Shear and stability at the base of the mixed layer in the arctic ocean: The role of inertial motions". Master's thesis, Naval Postgraduate School.

Toole, J. M.; Timmermans, M. L.; Perovich, D. K.; Krishfield, R. A., and Proshutinsky, A., 2010: "Influences of the ocean surface mixed layer and thermohaline stratification on Arctic sea ice in the Central Canada Basin". *Journal of Geophysical Researh*, **115**, pp. 1–14.

UIUC, Web 4. "UIUC: Archive of ice concentration". `http://arctic.atmos.uiuc.edu`. [Online; Accessed 2014-09-19].

Wallcraft, A.; Carroll, S. N.; Kelly, K. A., and Rushing, K. V., 2003: *Hybrid Coordinate Ocean Model, User's Guide.*

Wallcraft, A.; Metzger, E. J., and Carroll, S. N., 2009: *Software design description for the HYbrid Coordinate Ocean Model (HYCOM) version 2.2.*

Yang, J.; Comiso, J.; Walsh, D.; Krishfield, R., and Honjo, S., 2004: "Storm-driven mixing and potentiel impact on the Arctic Ocean". *Journal of Geophysical Research*, **109**, pp. 1–18.